UNIVERSITY OF CALIFORNIA
RIVERSIDE

Development of 3D Printing Enabled Methodologies for Microfluidic Cell Analysis and Surface Plasmon Resonance Sensing Enhanced by Nanoconjugates

A Dissertation submitted in partial satisfaction
of the requirements for the degree of

Doctor of Philosophy

in

Chemistry

by

Zhengdong Yang

December 2021

Dissertation Committee:

Dr. Quan Cheng, Chairperson
Dr. Yinsheng Wang
Dr. James F. Davies

The Dissertation of Zhengdong Yang is approved:

Committee Chairperson

University of California, Riverside

Acknowledgments

Five years ago, before I left home for the US, everyone in my family hugged me. I received lots of encouragement and wishes from my family. Today, I am still carrying these gestures of love and warmth, which have given me strength and hope along the way, even at the toughest times.

I still remember how I felt when I first arrived at Riverside. I was amazed by the open, friendly environment and culture in UCR, which I have always appreciated during the time I have studied here. Everyone, including professors, students, and colleagues, has been so helpful and enthusiastic. I have also appreciated that there are many places for relaxation and there were lots of resources available when I needed help. There is also a nice gym, and I have spent quite a lot of time there.

More importantly, I have had an awesome supervisor, Professor Quan Cheng. He has all the characteristics that one can hope for in a good mentor; he is patient, kind, generous, and rigorous in academic research. I know I have room to improve in many aspects. Therefore, I have been grateful that every time Professor Cheng pointed out any problems, he was always patient and tried not to embarrass me. Instead, he helped me realize what I needed to improve. Because of this, I was able to make unceasing progress during my graduate studies. Moreover, he continued to develop my confidence throughout my graduate career, which I have always appreciated.

I want to thank the amazing research group I am a part of. When I first joined the group, Dr. Sam Hinman, Dr. Pete Shanta, and Dr. Kelvin Tran generously provided guidance on both research and life in general. They were quite patient with me despite our

language barrier during my first few months at Riverside. I want to thank the previous visiting scholar, Professor Zhanjun Yang, for helping me to practice driving and for helping me with the nanoparticles projects, which is not covered in this thesis. I want to express my heartfelt gratitude to Professor Wei Cheng for helping me with the nanoclusters project and for being concerned for my life. I want to thank Daniel, Alex, and Malinick for helping me revise the manuscripts and for kindly offering their support during my graduate career. I want to thank Dr. Brent Adkins for training me on NTA for the liposome project, Dr. Zhili Guo for helping me with the TLC assays, and Dr. Dong Yan for helping me with the cleanroom experiments. I want to thank Santino, Kristy, Fatimah, and Liza for being great lab mates. I really learned a great deal from everyone in the lab! Specifically, I want to express my deep gratitude for Bochao Li not only for her awesome help and work with the MALDI project but also for being a great friend to share my annoyance and joy with.

I want to thank my homies: Baoning Wu, Boxiao Wang, and Ying Xiong. They are always there when I have cool ideas to share and am looking for suggestions. I want to thank my friends, Kingsley Wu and Yanwei He; they bring me joy and help me with my problems. I want to thank Yanxiang Wang and Kaizhu Guo for being great housemates and for their inclusiveness and help. I want to thank all my mates for playing basketball with me and passing me the ball. I want to greatly thank my mentor and manager, Dr. Deqing Xiao, for mentoring me during my internship at Gilead Science and for providing career advice.

I am thankful for my mother, Min Lu, and my father, Junhui Yang. I could not express how grateful I am for them even if I wrote tens of thousands of words of appreciation.

They are my heroes, my idols, and also my friends. Whatever I decide to do, they will always support me and have always been proud of me.

I want to express my heartful appreciation for my grandparents, Shuzhi Wu, Qingcun Yang, Shufen Jiang, and Jiuzeng Lu, and my aunt, Li Yang, who took care of me when I was a child and have loved me so much. Although my grandparents barely went to school, they loved me so much, made sure I ate my fill and had warm clothes to wear, and taught me to respect knowledge and to study diligently. My grandfather passed away last year, but I will always remember what he taught me: be a hardworking, thrifty, and steadfast person, and be kind to others. We all miss you so much.

Lastly, I want to thank everyone who helped me during my graduate career and all the researchers who maintain their enthusiasm to contribute to science and technology.

Copyright Acknowledgements

The text and figures in Chapter 2 of this dissertation, in full, are a reprint of the material as it appears in Yang, Z.; Malinick, A. S.; Yang, T.; Cheng, W.; Cheng, Q., Gold nanoparticle-coupled liposomes for enhanced plasmonic biosensing. *Sensors and Actuators Reports* **2020**, 2 (1), 100023. Two of the coauthors listed in that publication, Alexander Malinick and Tiantian Yang, helped to organize the work; Professor Wei Cheng and Professor Quan Cheng supervised the research.

This dissertation is dedicated to my parents, Junhui Yang and Min Lu, for their constant love, support and encouragement

ABSTRACT OF THE DISSERTATION

Development of 3D Printing Enabled Methodologies for Microfluidic Cell Analysis and Surface Plasmon Resonance Sensing Enhanced by Nanoconjugates

by

Zhengdong Yang

Doctor of Philosophy, Graduate Program in Chemistry
University of California, Riverside, December 2021
Dr. Quan Cheng, Chairperson

Understanding biomolecular interactions and cellular activities based on these interactions are important research topics in bioanalytical chemistry that can have a large impact on key fields such as drug discovery, biomedical sciences, and environmental monitoring. High performing biosensors are an essential part for this task. Effective sensing platforms with improved analytical performance and reduced cost are actively sought after and remain a major area of intense research endeavors. The goal of this thesis is to develop novel biosensing systems enabled by 3D printing technology and nanoscience for probing biochemical interactions and achieving cell lipidomic analysis.

Surface plasmon resonance (SPR) biosensors have been wildly applied for biomolecular assays in a label-free fashion. The sensitivity of SPR sensors, however, still needs signal enhancement when dealing with trace amounts of analytes. Chapter 2 describes the fabrication and application of gold nanoparticles-coupled POPC liposomes nanoclusters for signal amplification for SPR sensors and the study of protein-membrane recognition on a biomimetic interface. By combining the large mass of liposomes and plasmonic coupling of

the noble metal nanoparticles, the highly stable POPC-gold nanoparticles showed a large amplification effect and a 0.1 ng/mL LOD was achieved for cholera toxin detection.

3D printing technology has greatly impacted the bioanalytical fields by providing the fabrication capability with almost no geometric restriction, rapid prototyping, and low cost. Chapter 3 describes the design and fabrication of a Dove prism by 3D printing with transverse micropatterns for multiplexed sensing with SPR imaging. The sensitivity of the system was evaluated by bulk refractive index change and protein binding assays; both showed similar performance as compared to the SPR configuration using high end glass optics.

3D printing technology has been further applied to fabricating microfluidic chips for cell analysis. Chapter 4 demonstrates the design and fabrication of a 3D printed microfluidic device for on-chip cell lysis, lipid extraction and phase separation for lipidomic study of algae C. *reinhardtii* cells by the microchip enhanced MALDI-MS. Compared with conventional bulk methods, extraction by the microfluidic device showed higher efficiency and cell lysis capability.

Contents

List of Figures

List of Tables

Chapter 1

Introduction

Biochemical interactions, such as small molecule-biomacromolecule interactions and protein-ligand interactions, are critical for intracellular processes and key factors in our understanding of diverse biological systems. The use of biosensors to assist in the investigation of biomimetic systems has become increasingly important for the study of biochemical interactions. Surface plasmon resonance (SPR) biosensors, which are capable of monitoring changes in surface mass density of the sensor chip [1], have been widely utilized in the study of biomolecule interactions in various biomimetic systems [2]. SPR sensors have attracted considerable attention in bioanalysis through advantages such as label-free detection and simple instrumental format [3]. Thus far, a variety of approaches to development of sensing performance and instrumental setup of SPR sensors have been reported [4].

Cell omics study is another important discipline for investigations of biological systems. Unlike biochemical interactions, which focus on a specific type of interactive

process, omics is a comprehensive and statistically rigorous assessment of a various types of molecules [5]. Lipidomics is a subdiscipline of omics that is focused on cellular lipids on a large scale and plays a crucial role in biological, biomedical, and environmental research [6]. Matrix-assisted laser desorption/ionization mass spectrometry (MALDI-MS) is a sensitive and reliable tool for lipidomics research, and the analysis method is simple and convenient. In prior studies, our group developed a gold microwell chip for MALDI-MS with improved sensing performance, and the gold microwell chips are also used in the work of this thesis [7].

The research goal in this dissertation is to develop chip-based biosensing systems, including SPR sensors and microfluidic chip-based MALDI-MS, by integration of 3D printing and novel nanoparticle preparation, that demonstrate better sensing performance with lower cost than existing tools for lipidomics and biochemical interaction studies.

1.1 Surface Plasmon Resonance (SPR) and Surface Plasmon Resonance Imaging (SPRi) Biosensors

1.1.1 Theory of Surface Plasmon Resonance Biosensors

Since the first SPR sensor for gas detection and biosensing was developed in 1982 [8], sensing platforms based on SPR have been widely applied in bioanalytical chemistry, drug screening, and environmental monitoring [9]. SPR is known as a quantum electromagnetic phenomenon at the metal-dielectric interface where incident light interacts with free electrons on the surface, generating electron density waves (surface plasmons) that propagate along the metal-dielectric interface [10]. This electromagnetic field reaches its

maximum at the interface and decays exponentially on both sides as the distance from the interface increases. Thus, if there are molecular interactions at the interface or a change of refractive index for the dielectric media, SPR is capable of monitoring these slight changes [11] [12]. As a transverse magnetic (TM)-polarized wave, in which the magnetic vector is perpendicular to the surface plasmon propagation direction and parallel to the interface plane, the surface plasmon has a propagation constant which can be described by the following equation [13]:

$$\beta = k\sqrt{\frac{\varepsilon_m {n_s}^2}{\varepsilon_m + {n_s}^2}} \tag{1.1}$$

where k is the wave number in the free space, ε_m denotes the dielectric constant of the metal (including real and imaginary parts), and n_s is the refractive index of the dielectric. Gold and silver were selected to be the two most widely used metals for SPR sensors [14] [15]. Based on Equation 1.1, to match the optical wave vector of the incident light to the wave vector of the surface plasmon wave and meet the condition of surface plasmon resonance, a coupler with a higher refractive index or with diffraction effects is needed [10].

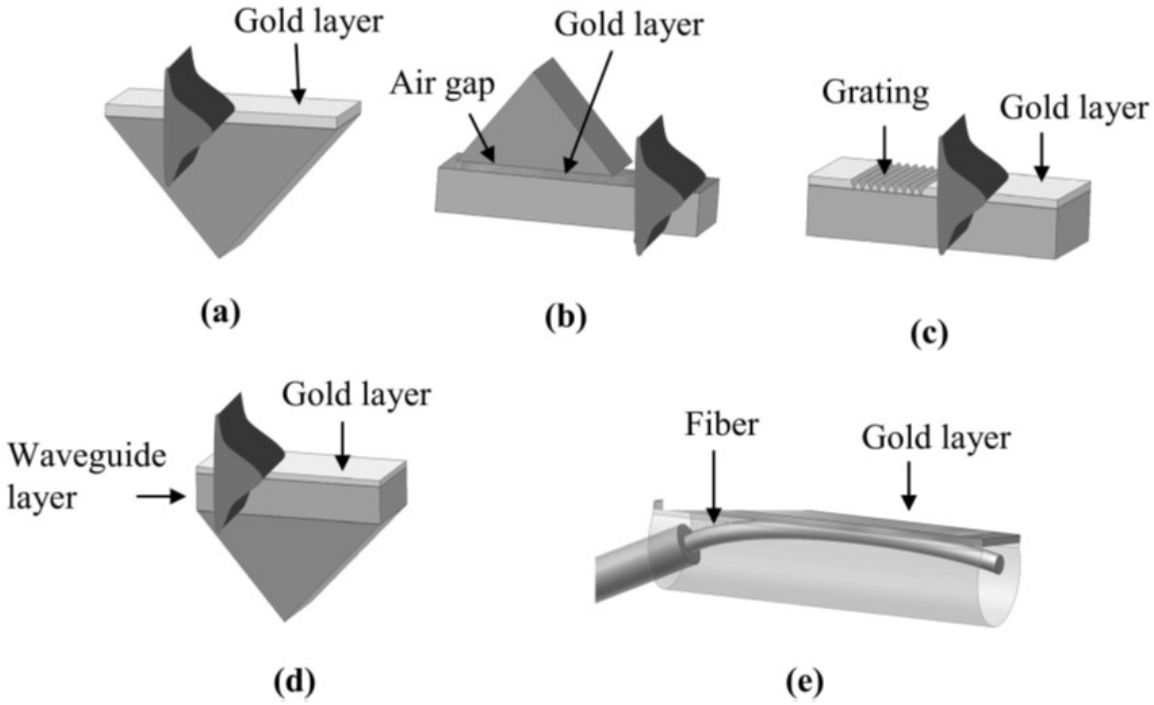

Figure 1.1: Various types of couplers for SPR, including prism couplers under (a) Kretschmann configuration and (b) Otto configuration, (c) grating couplers, (d) waveguide couplers, and (e) optical fibre couplers. Reprinted from Ref. [10], Copyright 2008, with permission from Taylor & Francis

There are several ways to excite SPR with the assistance of different couplers [10] [16] (Figure 1.1): (1) prism couplers in Otto configuration have a prism placed at the top of the metal film and a gap filled with sample liquid in between [17]; (2) prism couplers in Kretschmann configuration have a coated metal film above the prism surface and the sam-

ple medium in contact with the other side of the metal layer [18]; (3) grating couplers have metal diffraction grating; (4) waveguide couplers have a setup similar to the Kretschmann configuration; and (5) optical fibre couplers allow miniaturization of SPR sensors. Among the described configurations, the Kretschmann configuration in attenuated total reflection (ATR) mode is the most commonly used geometry due to its compact features and portability [13]. Multiple modes are applied for SPR sensing over time using this configuration, including reflected light wave intensity monitoring [19], resonant angle measurement [20], and resonant wavelength measurement [21].

The SPR sensor is currently used as a powerful tool to monitor cellular receptors and ligand binding. The association and dissociation rates obtained from SPR are important information for the evaluation of binding kinetics of molecules [22]. Normally, for a reversible reaction:

$$\mathrm{A} + \mathrm{B} \underset{\mathrm{k}_d}{\overset{\mathrm{k}_a}{\rightleftharpoons}} \mathrm{AB}$$

where k_a denotes the association rate constant and k_d denotes the dissociation rate constant. The conventional method for calculation of the key binding kinetic parameters is described as follows, with BIAcore, one of the most commonly used commercial SPR instruments, as an example. The signal R is assumed to be proportional to the formation of AB, and R_{max} is proportional to the concentration of active ligands for the targets on the interface. In this case, $(R_{max} - R)$ represents the unbonded sites on the surface at a specific time, t. Based on the assumptions above, an equation is obtained as follows [23]:

$$\frac{dR}{dt} = k_a C R_{max} - (\, k_a C + k_d)\, R \tag{1.2}$$

By plotting dR/dt versus R, the slope of k_s is obtained and is defined by the following equation [23]:

$$k_s = k_a C + k_d \tag{1.3}$$

If the k_s values are determined under different ligand concentrations (C), k_a and k_d can be calculated, based on equation 1.3, as the slope and the intercept on the y axis while plotting k_s versus C.

1.1.2 Surface Plasmon Resonance Imaging (SPRi)

The development of the surface plasmon resonance imaging (SPRi) technique has greatly improved the throughput of conventional SPR sensors [24], which is achieved by monitoring the reflectance image of the chip with a plasmonic microarray under a CCD camera [3]. Compared with traditional SPR biosensors, which rely on scanning resonance angle change or resonance wavelength change, SPRi sensors generally measure the intensity

of reflected p-polarised light at a fixed angle [25] (Figure 1.2). S-polarised light is used as a reference signal to reduce effects of visual artefacts [25]. For quantitative SPRi assays, the incident light angle should be located in the linear response region of the reflectivity curve, where the light intensity change is proportional to the effective refractive index [26]. Due to the application of SPRi with multiple microarrays on a single chip, SPRi sensors are able to collect data on various analytes/samples at one time.

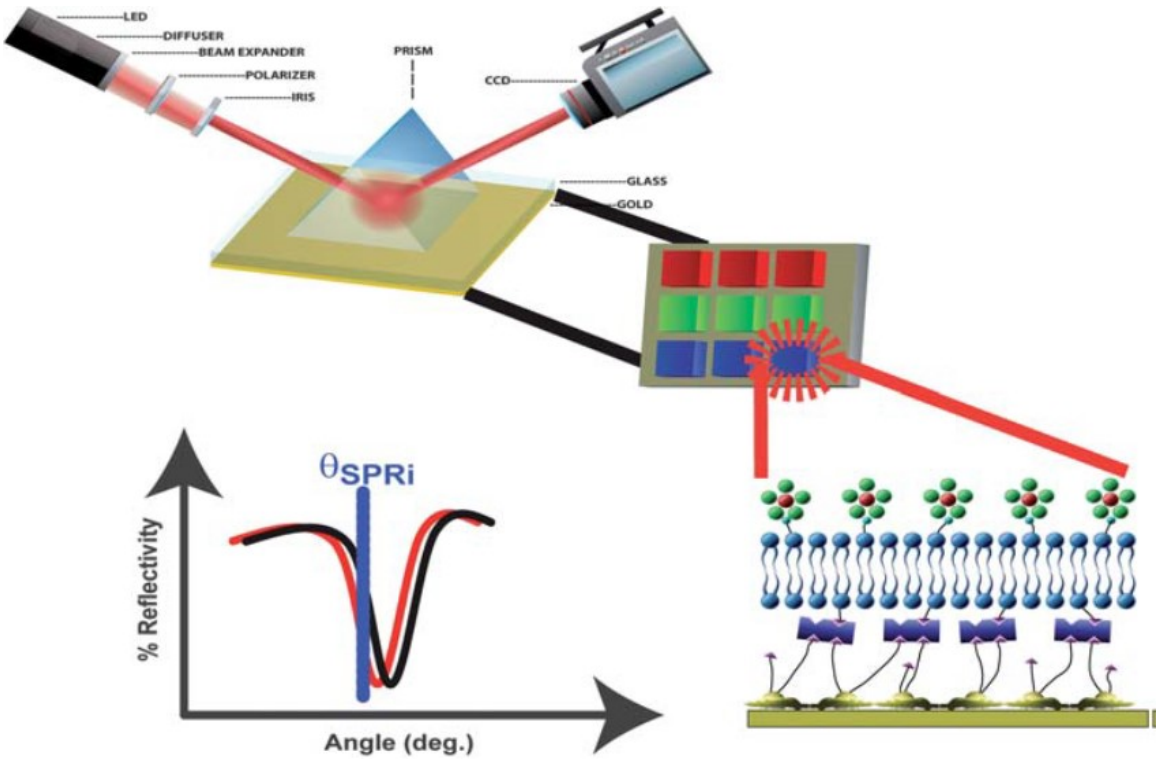

Figure 1.2: Scheme of the working principle of SPR imaging biosensors. Reprinted from Ref. [27], Copyright 2010, with permission from Royal Society of Chemistry

Arrays design plays an important role in sensing performance and the capacity for multiplexed analysis using SPRi. Krishnamoorthy and coworkers presented an electrokinetic biomolecular screening chip combining microfluidic technology with SPRi and were able to screen up to 10 samples simultaneously [28]. Additionally, our group has developed a sialoside-based carbohydrate microarray with 400 spots on a single chip by contact printing for SPRi [29]. New developments in interface design will continue improvement of SPRi sensing platforms, resulting in higher sensing efficiency and lower non-specific background signal [27].

1.1.3 Applications of Noble Metal Nanoparticles for Signal Amplification of SPR Biosensing

For traditional SPR biosensors, the limit of detection is often in the nanomolar range, restricting its application for high-sensitivity biosensing [30]. A number of approaches to signal amplification of SPR biosensors have been reported. Noble metal (e.g., gold and silver) nanoparticles, as typical metallic plasmonic nanostructures, are widely applied for signal enhancement in SPR due to their unique properties [24]. At nanometer sizes, noble metal nanoparticles hold free electrons on their surface, which oscillate under the excitation of proper incident light. This phenomenon is called localized surface plasmon resonance (LSPR). Specifically, when being used as a signal enhancer tag in SPR sensing platforms, the surface plasmon polaritons of the metal film can couple with the localized surface plasmon of the metal nanoparticles, causing significant signal enhancement [31]. The configuration, size, and shape of the metal nanoparticles were reported to be key factors

in signal amplification performance in SPR according to both theoretical and experimental studies [32] [33].

Gold nanoparticles (AuNPs) are the most commonly used noble metal nanoparticles for signal enhancement in SPR because of the high stability and ease of preparation. Labeled gold nanoparticles can be applied as signal enhancement tags for sandwich immunoassays in SPR by taking advantage of the plasmon coupling effect of AuNPs [34] [35]. Moreover, AuNPs can also combine with other nanoparticles and act as magneto-plasmonic probes for signal amplification [36]. In addition to use as signal amplification tags, AuNPs have also been used via direct immobilization on the metal layer, which improves sensitivity by forming a self-assembled monolayer (SAM) or through being entrapped on the surface [37] [38], resulting in increased surface area compared to the original planar surface.

1.2 3D Printing for Optical Biosensors

1.2.1 Principles and Fabrication Methods for 3D Printing

Three-dimensional (3D) printing, also known as additive manufacturing, provides a fast and robust way to fabricate highly complex objects quickly and at low cost and has revolutionized many aspects of the manufacturing industry [39]. To date, multiple printing techniques with various materials delivery and solidification methods have been applied in 3D printing fabrication (Figure 1.3) [40] [41]. Among these fabrication methods, fused deposition modeling (FDM) and stereolithography (SLA) are the two major technologies with commercial application.

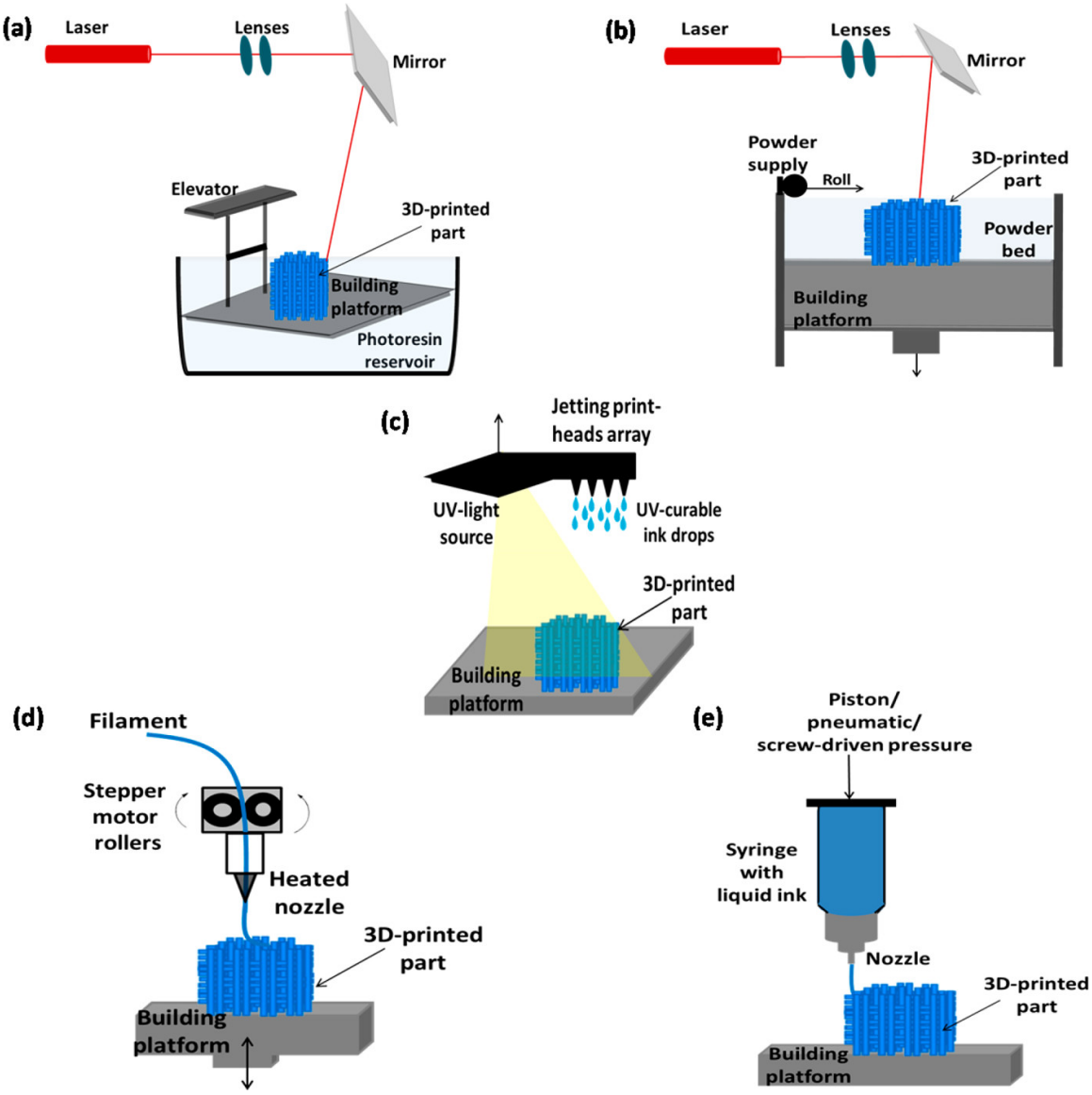

Figure 1.3: Major fabrication techniques for 3D printing. (a) Laser assisted stereolithography (SLA), (b) Laser assisted selective laser sintering (SLS), (c) Inkjet printing, (d) Fused deposition modeling (FDM), and (e) Liquid deposition modeling (LDM). Reprinted from Ref. [41], Copyright 2018, with permission from ACS Publications.

The FDM method relies on thermoplastic polymeric materials that are extruded to print the objects in a layer-by-layer workflow [42]. This technique is capable of printing out multiple materials, including acrylonitrile butadiene styrene (ABS), polylactic acid (PLA), polycarbonate (PC), and a PC-ABS blend [43]. Generally, FDM involves low-cost materials and open source nature, yet also has drawbacks, such as low resolution output and a time consuming process [44].

Stereolithography (SLA) utilizes liquid photocurable polymeric resin that polymerizes into solid form when triggered by ultraviolet (UV) light; like FDM, the deposition of material in SLA occurs layer-by-layer [42]. Various types of resin can be used to meet the requirements of the printed products. Objects printed by SLA have well-controlled layer-thickness and relatively smooth surfaces [45]. Use of SLA has advantages in the fabrication of accurate and complex internal structures, but has limited capability in handling multiple materials for a single object [44].

1.2.2 3D Printing Techniques for Optical Biosensing

To date, 3D printing has been used in a variety of disciplines and products, such as robotics, medical devices, actuators, switches, and sensors [46] [47]. Specifically, 3D printing has had remarkable impact on the advancement of analytical chemistry through its wide application in design and production of new analytical equipment and manufacturing parts [40].

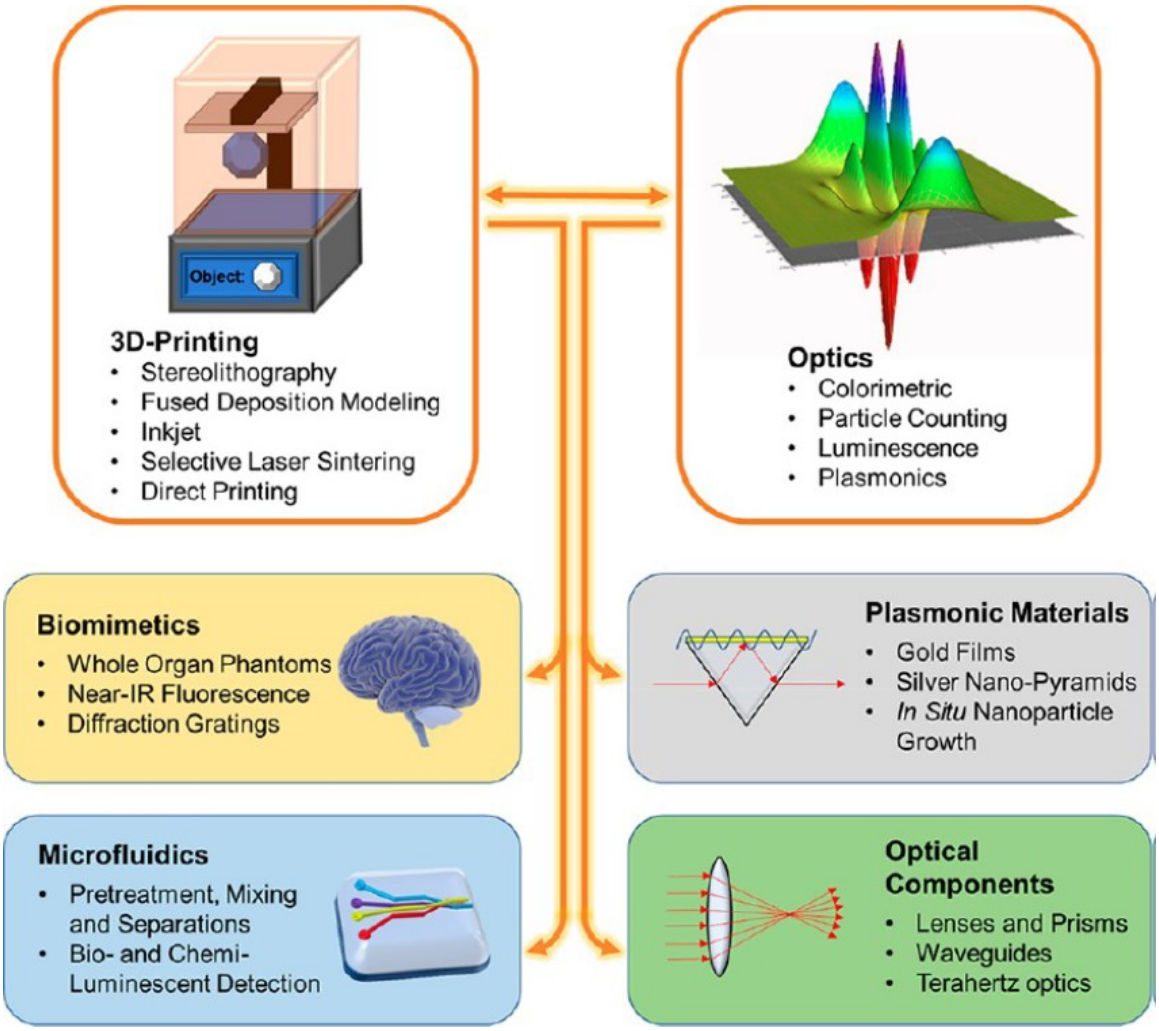

Figure 1.4: 3D printing applications for optical biosensing. Reprinted from Ref. [48], Copyright 2018, with permission from ACS Publications.

Additionally, 3D printing of optical equipment for biosensing has generated considerable attention based on its low cost and production of parts with high quality optical properties, thereby promoting use of 3D printing in biomimetics, production of plasmonic materials, microfluidics, and for fabrication of other optical components (Figure 1.4) [48]. As a promising point-of-care and lab-on-a-chip system, microfluidics has been coupled with 3D printing technologies for optical detection [49] [50]. In the meantime, 3D printed objects can also be used for mechanical integration of biosensors. An example of this is the fabrication of a 3D printed fluidic cartridge for fully automated colorimetric enzyme-linked immunosorbent assay (ELISA) for malaria detection [51]. Moreover, another important use for 3D printing is to fabricate plasmonic surfaces. Zhang and coworkers reported 3D printing of entire structural components of an angle-scanning SPR sensor [52]; likewise, our group demonstrated the 3D printing of equilateral prisms by SLA for SPRi sensing [53]. Overall, there is a great potential for continuing beneficial impact of 3D printing on analytical chemistry, particularly in the development of advanced biosensing platforms.

1.3 Microfluidic Devices and Their Applications in Analytical Chemistry

1.3.1 Microfluidics: Concept and Theory

Since the early research on gas chromatography at Stanford University and the development of ink jet printers by IBM in the 1960s, microfluidic devices have been flourishing as efficient tools that are deployed widely throughout industry [54]. A microfluidics platform is a system involving microscale channels, with dimensions that are usually tens

to hundreds of micrometers, that manipulate fluids at relatively small volume (1 nL to 10^{-9}nL) [55]. Microfluidic devices are commonly used for reactions, mixing, sample treatment, and detection through microfluidic networks with goal-specific designs. Specifically, in the field of bioanalysis, microfluidics shows advantages in its capacity to deal with samples at extremely low volume. Using microfluidics, sample separation and detections can be achieved with brilliant sensitivity in high-throughput processes, thereby decreasing both the cost and time needed for analysis [55]. Microfluidics theory is a mixture of many subdisciplines, including fluid mechanics, electrostatics, statistical mechanics, thermodynamics, and materials science.

If the continuous fluid in the microchannel is a Newtonian fluid, it will follow the Navier-Stokes equations, which describe the continuum version of F=ma for a unit volume [56] [57]:

$$\rho\frac{\partial u}{\partial t} + \rho(\, u.\nabla)\, u = \nabla \cdot \sigma + f = -\nabla p + \eta\nabla^2 u + f \tag{1.4}$$

where f stands for the body force densities, and ρ, p and ∇ denote the density, pressure and dynamic viscosity of the fluid, respectively. u represents the linear velocity, and σ is the fluid stress (force per unit area). However, for most cases in the microfluidic model, when inertial forces are negligible compared with the viscous force, the nonlinear term is omissible, and equation 1.4 becomes:

$$\rho\frac{\partial u}{\partial t} = \nabla \cdot \sigma + f = -\nabla p + \eta\nabla^2 u + f \tag{1.5}$$

In both circumstances, mass conservation meets the condition that:

$$\frac{\partial p}{\partial t} + \nabla \cdot (\, pu) \, = 0 \tag{1.6}$$

giving the incompressibility condition ($\nabla \cdot u = 0$) for fluids at a low flow rate and with nearly constant density.

Reynolds number (Re) is a common parameter for prediction of fluid flow situations, and can be expressed as:

$$Re = \frac{uL}{\nu} \tag{1.7}$$

where L is the linear dimension, and ν denotes the kinematic viscosity of the fluid. Considering that the spatial length scale L and the fluid velocity u are both relatively small,

which results in a small value for Re, the fluid in the microchannel is laminar in most cases [58].

1.3.2 Materials and Fabrication Methods of Microfluidic Devices

Fabrication method is a pivotal factor in the development of a microfluidic platform and a primary consideration when designing microchannel networks. Figure 1.5 presents the benchmarks in microfluidic device fabrication history. Fabrication method varies based on the materials used for the microfluidic devices. Diverse substrate materials, including silicon, metals, ceramics, glass, and polymers have been used for microfluidic platform fabrication for different applications [59].

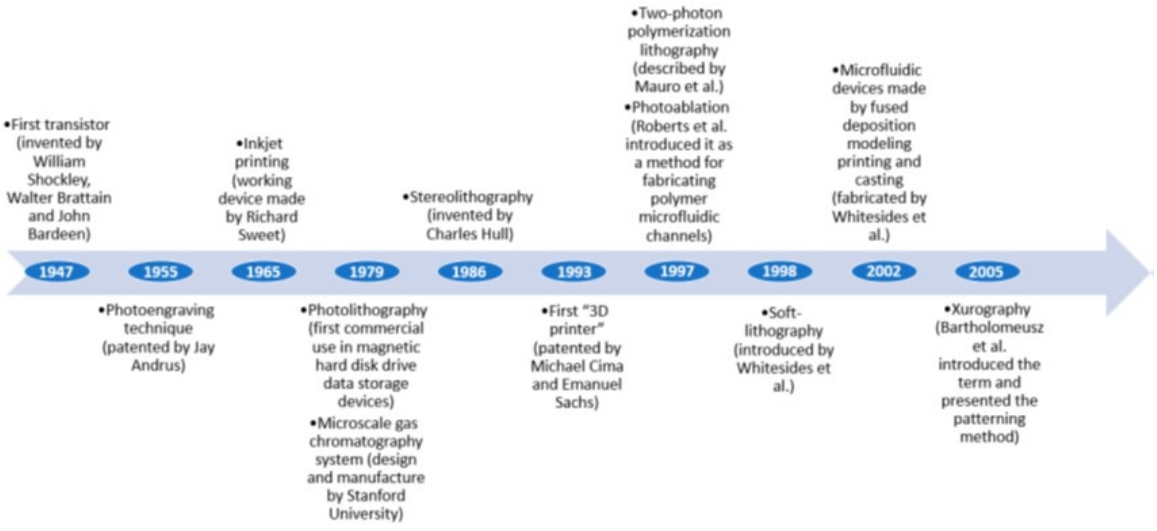

Figure 1.5: Benchmarks in the microfluidic devices fabrication history. Reprinted from Ref. [59], Copyright 2021, with permission from Multidisciplinary Digital Publishing Institute.

Silicon-based microfluidic devices show excellent chemical compatibility and thermal stability, but suffer from the disadvantages of high price, fragility, and opacification, making them unsuitable for optical uses [60]. In comparison, metal-based microfluidic devices offer high thermal stability, low cost, and ease of use during fabrication [61]. Metal-made microfluidics systems have been successfully applied in nanoparticle synthesis [62]. In recent years, paper microfluidic devices have shown unique benefits in microfluidic manufacture, including simplicity of use, low cost, and disposability [63]. One of the most impressive aspects of paper microfluidics is that, relying on the hydrophilic paper material (e.g., cellulose fiber), fluid can be conveyed along the paper surface via capillary force without the assistance of a pump [64]. This advantage has resulted in wide use of paper microfluidics in fast point-of-care biosensors for target analytes [65]. However, a major weakness of paper-based microfluidics is the lack of mechanical strength, therefore it can be easily broken when handled improperly [66]. Other than the materials described above, glass and polymers are the most commonly used microfluidics materials, which show great potential in many aspects of microfluidics applications.

Glass Materials for Microfluidic Devices and Fabrication

Glass, primarily SiO_2 but also containing other oxides, such as CaO, Na_2O, K_2O, Al_2O_3 and B_2O_3, was first chosen as a substitute material for silicon substrate during early use of microfluidic devices to reduce cost and increase transparency [67]. Even though polymers like polydimethylsiloxane (PDMS) and poly (methyl methacrylate) (PMMA) gradually become increasingly popular for microfluidics devices fabrication due to simplicity of manufacturing and cost-efficient features, glass-made microfluidic devices still have the ad-

vantages of high chemical and thermal resistance and low non-specific adsorption when dealing with biological samples [68] [69] [70].

Most of the manufacturing methods for microchannels on glass substrate can be summarized as chemical, mechanical, and laser-based processes [67]. Normally, wet etching by hydrofluoric acid (HF) with high etching efficiency, dry etching by deep reactive ion etching, and electrochemical discharge machining are the three major chemical processes for glass microfluidics channel fabrication [71] [72] [73]. Abrasive jet machining, ultrasonic machining and cutting approaches by materials removal, micro milling or micro grinding are commonly used cutting processes for microfluidics fabrication [74] [75] [76]. For laser based processes, photothermal, ultra-short pulse, and absorbent material approaches are the conventional fabrication methods [77] [78] [79].

Polymer Materials for Microfluidic Devices and Fabrication

The emergence of polymer microfluidic devices overcame the limitations of traditional micro-electromechanical systems (MEMS) materials, which suffer from high cost and time-consuming fabrication processes [80]. Polymer materials used for microfluidic devices are PMMA, fluoropolymers, PDMS, cyclo-olefin polymers and copolymers (COPs/COCs), and thiol-ene polymers (TEs) [59]. Fabrication methods for polymer based microfluidic devices can be flexible according to needs and accessibility, including mould or master manufacturing processes (such as micro-cutting, ultrasonic machining, electrodischarge machining, micro-electrochemical machining, laser ablation, electron beam machining, focused ion beam machining, and mould fabrication on curved surfaces), low-volume production (such as casting, laminate manufacturing, laser fabrication, and 3D printing), and high volume

production (such as hot embossing, injection moulding, film or sheet operations, roller embossing, and microthermoforming) [80].

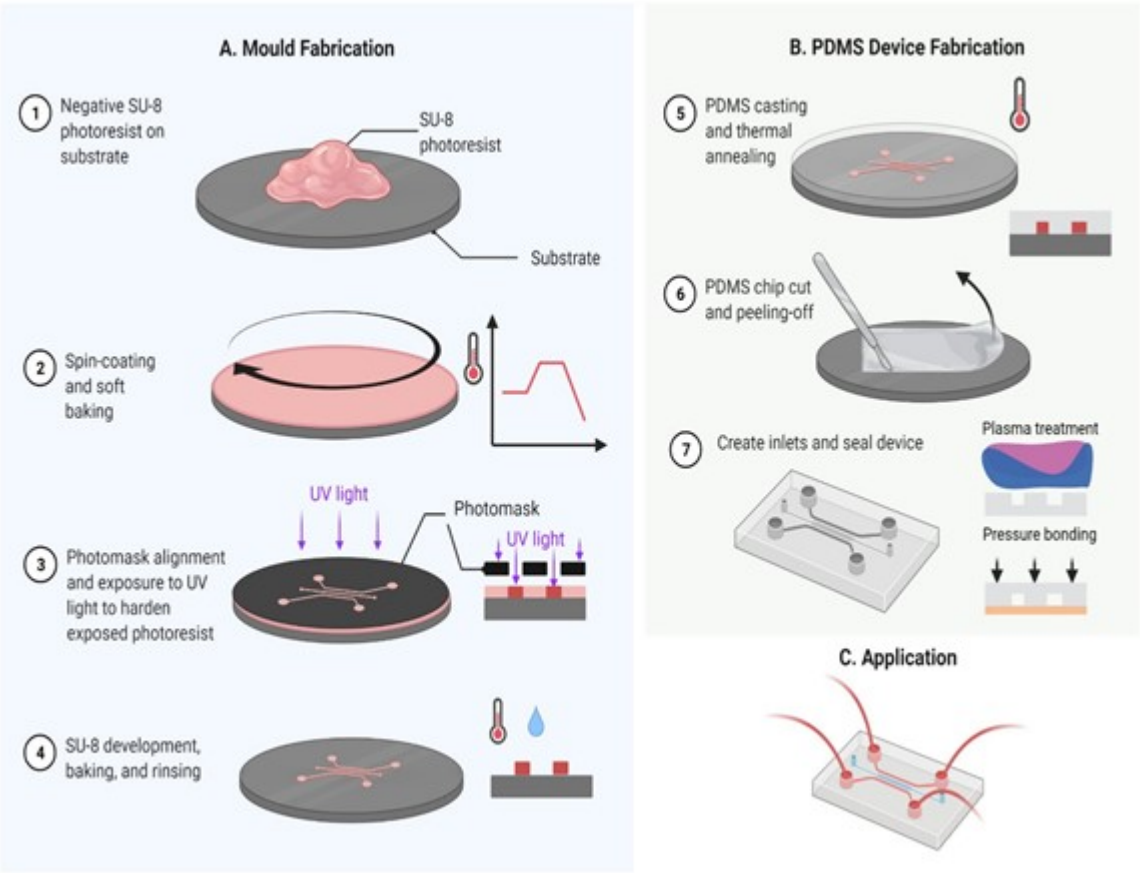

Figure 1.6: Scheme of conventional PDMS microfluidic devices fabrication. (A) Mould fabrication process. (B) PDMS casting and bonding. (C) Application of PDMS microfluidic devices. Reprinted from Ref. [80], Copyright 2021, with permission from Multidisciplinary Digital Publishing Institute.

PDMS, one of the most widely used microfluidics polymer materials, is a typical elastomer that is capable of changing shape under force and return to its original shape after the removal of the force. Besides this feature, PDMS is also inexpensive, easy to fabricate, transparent, and biocompatible, which makes it an excellent materials candidate for use in microfluidic devices [81]. Casting (or soft lithography) is one of the most commonly applied fabrication approaches in PDMS microfluidics, in which moulding is used to generate micro-sized or even nano-sized channels. Figure 1.6 illustrates a common fabrication procedure used in production of PDMS-based microfluidic devices using an SU-8 master mould [80]. Briefly, the negative SU-8 resist is first spin coated onto the substrate. A soft bake procedure is then carried out by adjusting to proper temperature. A photomask with the designed pattern is applied; SU-8 polymerization then occurs in the area exposed to UV light and is accelerated by a second bake process. After rinsing the unpolymerized area, the pattern mould on the substrate for microfluidic channels appears. A well-blended mixture of PDMS silicone elastomer base and catalyst is then transferred to the mould with the designed patterns and cured at a specific temperature. The polymerized PDMS elastomer is then removed and sticked with a cleaned substrate via plasma treatment [82]. PDMS casting has also been used for fabrications of multi-layer PDMS microfluidic devices [69].

3D Printing Techniques for Microfluidics Fabrication

Currently, due to the rapid expansion of applications for 3D printing, it has become one of the most important and promising alternative approaches to the traditional SU-8 moulding method for fabrication of microfluidic devices [83]. Processes that employ 3D printing allow rapid, inexpensive, and user-friendly manufacturing and prototyping for

geometrically complicated structures [84]. Thus far, 3D printing techniques have been applied in many aspects of microfluidic fabrication using various types of resins. Techniques involving 3D printing can be used to create multiple functional elements for the microfluidics setup, such as actuators (valves, pumps, and multiplexers) [83], as well as complete microfluidic devices [85]. Moreover, printing moulds for PDMS microfluidics is another important application of 3D printing in microfluidics fabrication. Use of 3D printing not only maintains the advantages of PDMS materials, such as biocompatibility and elasticity, but also simplifies fabrication of moulds for duplication of PDMS microfluidics platforms, resulting in dramatic reduction of fabrication cost.

1.3.3 Microfluidic Device Applications

Microfluidic Devices for Sample Treatment

Taking advantage of the small dimensions and ultra-high surface-to-volume ratio of microfluidic channels, microfluidic devices are capable of handling extremely small sample volumes and are highly efficient in mixing or reaction acceleration, making them excellent tools for sample treatment in a high-throughput context. One of the important uses of microfluidics for sample treatment is fluid separation and water treatment [86]. Specifically, liquid-liquid extraction is a typical method of sample purification and separation, and easily achieved using microfluidic devices. There are several benefits to performing the extraction process in micrometer-scale channels: (1) only a small amount of sample is needed, and microchannels with high surface-to-volume ratio accelerate mass transfer between phases [87]; (2) the flow remains laminar because of the low Reynolds number [88]; and (3) the high-

throughput approach requires less energy consumption [89]. In addition, microfluidic devices have been used for water purification with membrane and electrochemical technologies [90] [91].

Besides conventional sample separation and water treatment, another important use for microfluidic sample treatment is separation of biological samples [92] and preparation of samples for medical diagnostics [93]; examples include whole blood fractionation [94] and micro-solid-phase extraction from cell lysates [95]. Moreover, microfluidic devices have been used to create droplets of controlled size and shapes for applications, such as sample screening and monodispersed particles or vesicles production [96].

DNA sequencing is another field in which microfluidics can be a powerful tool. Traditionally, for processing of samples for DNA sequencing, several steps are needed to prepared a sample with enough DNA of interest; this includes cell transformation and culture, picking colonies, and DNA purification and amplification, with Sanger extension and product purification typically necessary, which is inefficient, expensive and cumbersome [97]. With the assist of (digital) microfluidic techniques, the DNA sample preparation workflow can be simplified considerably and automated [98]. The development of lab-on-a-chip microfabrication promotes high-throughput DNA sequencing with improved efficiency and substantial conservation of samples.

Microfluidic Devices for Production and Modification of Lipids

Cell culture, cell treatment, and lipid harvesting are several other important applications of sample treatment by microfluidic systems [99] (Figure 1.7).

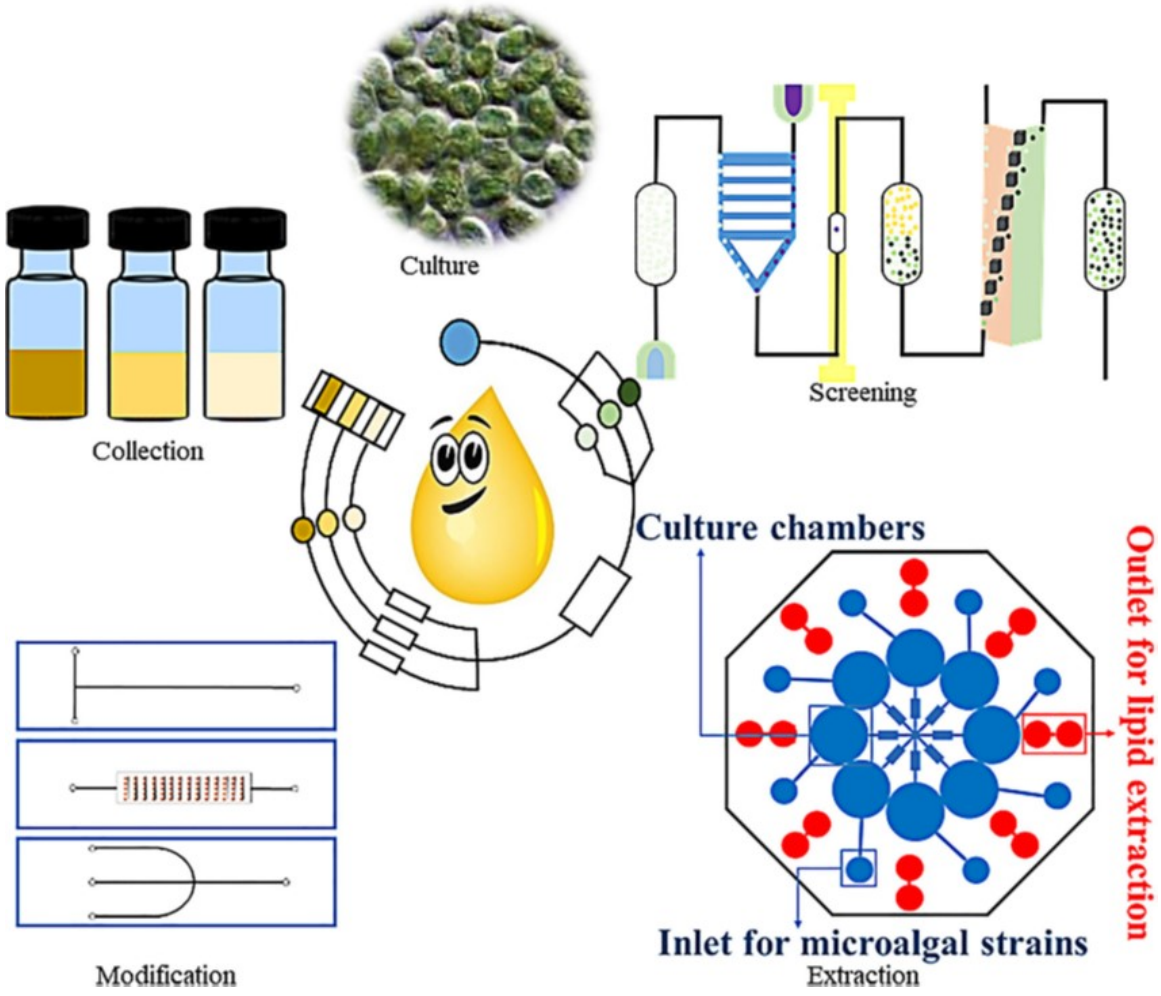

Figure 1.7: Scheme of microfluidic devices for microorganisms culturing, lipids collection and modification. Reprinted from Ref. [99], Copyright 2019, with permission from Springer.

Within an enclosed microchannel, microenvironments for cell culture and treatment are easily controlled and monitored [100]. In addition, treated cells can be transferred directly into the next microfluidic device for further treatment by connecting the outlet of the first microfluidic device to the inlet of the second microfluidic chip without additional transfer processes, which avoids contamination during sample transfer processes. In most cases, the microchannels are used as microreactors for screening and modification. The lipid components of microorganisms can be accumulated and separated within a properly designed microfluidic setup, which significantly reduces the time and cost of lipid harvesting.

Coupling of Microfluidic Devices to Mass Spectrometry (MS)

By coupling microfluidic devices to MS, sample preparation can be simplified and analytical performance can be enhanced simultaneously [101]. These microchips can be used for either sample separation followed by MS analysis or direct on-chip analysis of the unseparated sample [102]. For instance, using microchips as miniaturized emitters for electrospray ionization (ESI), sample consumption is significantly reduced and detection sensitivity is increased [103]. In addition, coupling of microfluidics to MALDI-MS via microfluidic chips has been utilized for sample dispensing and pretreatment (such as preconcentration, digestion and purification), resulting in better sensing performance [101].

To date, microfluidics techniques have been applied in sample preparation, point-of-care processes, cell analysis, nucleic acid assays, drug screening, and omics studies [104], and use continues to expand in the physical and biological sciences.

1.4 MALDI-MS and Its Use in Lipidomics

1.4.1 Basics of MALDI-TOF Mass Spectrometry

MS technology has revolutionized the identification of multiple analytes via simple, rapid, and efficient assays for analytical chemistry and the life sciences. In MS, charged gas-phase ions are isolated by electric or magnetic fields and identified by their specific mass-to-charge ratio (m/z). Based on MS data, the molecular structure and composition of an analyte can be identified. Ionization plays a crucial role in MS-based analysis. ESI and MALDI, two common ionization approaches in MS, are both soft ionization methods which transmit minimal internal energy to the analytes [105].

Matrix-assisted laser desorption/ionization time-of-flight mass spectrometry (MALDI-TOF MS) is a powerful tool for the identification and study of DNA, protein, lipids, and glycoconjugates [106] [107] [108], where ions are desorbed from a solid interface with the assistance of a matrix. The dried matrix and sample crystal is exposed to a laser beam, causing it to be ionized and converted to the gas phase (Figure 1.8). Since the absorption of laser energy is a key factor in analyte ionization, the use of a proper matrix and suitable substrate is essential [109]. A number of compounds, such as derivatives of benzoic acid, cinnamic acid, and other similar aromatic compounds, are good candidates for matrix selection, due to multiple factors, including amenability to co-crystallization and direct influence on the ionization performance of the analyte [110]. In addition, the sensing performance for MALDI-MS also varies with planar substrates with different materials [111].

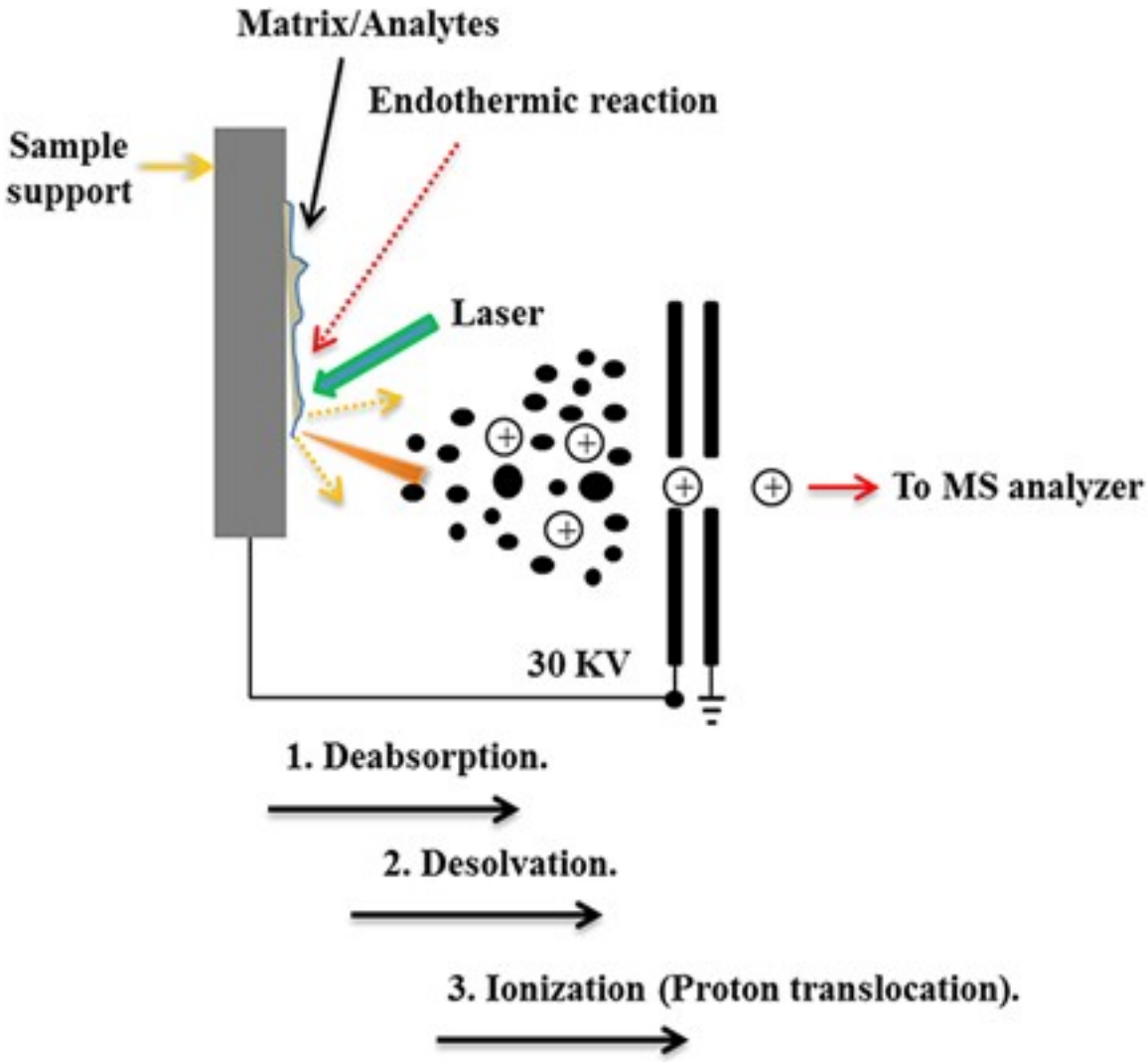

Figure 1.8: Scheme of the theory of MALDI-MS. Reprinted from Ref. [109], Copyright 2019, with permission from Frontiers.

In contrast to ESI, MALDI utilizes samples as solids rather than in the solution, making it less suitable for direct coupling with liquid chromatography for quantitative analysis. However, unlike ESI, the salt, detergents, or other impurities that exist due to sample preparation for ESI do not impact the sensing results via the ionization mechanism of MALDI, indicating the superiority of MALDI in this context [105] [112].

1.4.2 MALDI-MS Applications in Lipid Research

MALDI-TOF MS has a broad range of applications, including identification of microorganisms for medical diagnostics, environmental science, food safety, and biodefense [113]. MALDI-TOF MS has also been demonstrated as a powerful tool for lipidomic research [114].

As one of the main components of cellular membranes and lipid particles, lipids plays critical roles in cellular activities, cell signaling transduction, disease diagnostics, and environmental monitoring [6] [115]. As part of lipid analysis on a large scale, lipidomics has ongoing, significant impact on the fields of biology and analytical chemistry. Compared to conventional methods, such as high-performance liquid chromatography (HPLC), thin-layer chromatography (TLC), and ESI-MS, MALDI-TOF MS is a powerful assay used in lipid research that allows high throughput analysis with excellent sensitivity [116]. With both lipid and the matrix able to be dissolved in organic solvents, one-step and single organic phase sample preparation provides high reproducibility in formation of homogeneous crystals compared to the analysis of other polar molecules [117]. MALDI-TOF MS has been used to identify and characterize various lipid species, such as free fatty acids, cholesterol and cholesteryl esters, glycerolipids and glycerophospholipids, and acylglycerols and

phospholipids [118] from vegetable oils, cell extracts, tissues and body fluids, and oxidation samples of lipids, which provide valuable analytical information about cells and tissues [117].

1.5 Scope of Dissertation

The goals for this thesis are to improve the fabrication and sensing performance of surface plasmon resonance biosensors and microfluidic chip-based MALDI-MS, for lipidomics and biochemical interaction studies with integration of nano materials and 3D printing technology.

Lack of sufficient sensitivity could be an issue of SPR sensors while detecting trace amount of analytes. Signal amplification platform for SPR with novel materials is needed to improve the sensing performance. Chapter 2 focuses on the study of signal amplification impact of nanoclusters for plasmonic biosensors, and describes use of noble metal nanoparticles-coupled lipid vesicles as a signal amplification tool for SPR biosensing. These nanoclusters were fabricated via a straightforward salt-induced aggregation process and purified using a column-free approach. Nanocluster stability was assessed to determine material robustness. Through the large mass of the liposomes and plasmon coupling effects of the noble metal nanoparticles, the SPR signal was significantly enhanced. In addition, the sensing platform with nanoclusters provided a good reference to be used in studies of cell membranes and vesicle interaction.

3D printing technique is playing an increasing important role in the analytical field. However, there is limited work reported for 3D printing optics-based multiplex biosensing

systems. In Chapter 3, we demonstrate use of 3D printing to fabricate Dove prisms with line patterns for SPRi, which are capable of conducting multiplex assays simultaneously. Compared to the 3D printed equilateral prism for SPRi biosensing previously reported by our group, the resonance angle became 8° smaller and the sensing area increased by 21%, producing more reliable results. We also used this platform to monitor the refractive index change of the medium and protein binding on the interface. Furthermore, 3D printed E-beam evaporation masks were used to fabricate plasmonic microarrays on prisms with a larger number of sensing arrays via a photolithography-free process. Through these methods, the cost of the prisms were significantly reduced and micropattern fabrication was greatly simplified without compromising the sensitivity of the SPRi sensor.

MALDI-MS is a powerful analytical tool for lipidomics study. Cell lysis and lipid extraction are crucial sample treatment steps for conventional MALDI lipid analysis. However, traditional lipid extraction methods usually require large sample volume and are time consuming. In Chapter 4, we describe further application of 3D printing to fabricate microfluidic devices for sample treatment for mass spectrometry lipidomic analysis. A 3D printed microfluidic system was used for on-chip cell lysis, lipid extraction, and phase separation. The high mass transfer rate between the phases was demonstrated by fluid dynamic study of both velocity field simulation and droplet breakup simulation. TLC, fluorescent images, and MALDI-MS assays were used to evaluate the efficiency of the microfluidic lipid extraction process. Moreover, various organic phases were used for lipid extraction via the microfluidic system and lipid profiles with different lipid intensities were obtained. Through this work, we have developed a novel 3D printed microfluidic platform for highly efficient

lipid extraction and opened new avenues for lipidomics research. In Chapter 5, we summarize the work described in previous chapters, with additional discussion of related studies and future directions.

REFERENCES

[1] Patrik Aspermair, Ulrich Ramach, Ciril Reiner-Rozman, Stefan Fossati, Bernadette Lechner, Sergio E Moya, Omar Azzaroni, Jakub Dostalek, Sabine Szunerits, Wolfgang Knoll, et al. Dual monitoring of surface reactions in real time by combined surface-plasmon resonance and field-effect transistor interrogation. *Journal of the American Chemical Society*, 142(27):11709–11716, 2020.

[2] Neslihan Idil, Monireh Bakhshpour, Işık Perçin, and Bo Mattiasson. Whole cell recognition of staphylococcus aureus using biomimetic spr sensors. *Biosensors*, 11(5):140, 2021.

[3] Emily A Smith and Robert M Corn. Surface plasmon resonance imaging as a tool to monitor biomolecular interactions in an array based format. *Applied Spectroscopy*, 57(11):320A–332A, 2003.

[4] Pranveer Singh. Spr biosensors: historical perspectives and current challenges. *Sensors and actuators B: Chemical*, 229:110–130, 2016.

[5] Yehudit Hasin, Marcus Seldin, and Aldons Lusis. Multi-omics approaches to disease. *Genome biology*, 18(1):1–15, 2017.

[6] Kui Yang and Xianlin Han. Lipidomics: techniques, applications, and outcomes related to biomedical sciences. *Trends in biochemical sciences*, 41(11):954–969, 2016.

[7] Peter V Shanta, Bochao Li, Daniel D Stuart, and Quan Cheng. Plasmonic gold templates enhancing single cell lipidomic analysis of microorganisms. *Analytical chemistry*, 92(9):6213–6217, 2020.

[8] Bo Liedberg, Claes Nylander, and Ingemar Lunström. Surface plasmon resonance for gas detection and biosensing. *Sensors and actuators*, 4:299–304, 1983.

[9] Yong Chen and Hai Ming. Review of surface plasmon resonance and localized surface plasmon resonance sensor. *Photonic Sensors*, 2(1):37–49, 2012.

[10] Ibrahim Abdulhalim, Mohammad Zourob, and Akhlesh Lakhtakia. Surface plasmon resonance for biosensing: a mini-review. *Electromagnetics*, 28(3):214–242, 2008.

[11] Tzong-Hsien Lee, Daniel J Hirst, Ketav Kulkarni, Mark P Del Borgo, and Marie-Isabel Aguilar. Exploring molecular-biomembrane interactions with surface plasmon resonance and dual polarization interferometry technology: expanding the spotlight onto biomembrane structure. *Chemical reviews*, 118(11):5392–5487, 2018.

[12] JM Pitarke, VM Silkin, EV Chulkov, and PM Echenique. Theory of surface plasmons and surface-plasmon polaritons. *Reports on progress in physics*, 70(1):1, 2006.

[13] Jiřı Homola, Sinclair S Yee, and Günter Gauglitz. Surface plasmon resonance sensors. *Sensors and actuators B: Chemical*, 54(1-2):3–15, 1999.

[14] Mark A Ordal, LL Long, RJ Bell, SE Bell, RR Bell, RW Alexander, and CA Ward. Optical properties of the metals al, co, cu, au, fe, pb, ni, pd, pt, ag, ti, and w in the infrared and far infrared. *Applied optics*, 22(7):1099–1119, 1983.

[15] Jerome Hottin, Edy Wijaya, Laurent Hay, Sophie Maricot, Mohamed Bouazaoui, and Jean-Pierre Vilcot. Comparison of gold and silver/gold bimetallic surface for highly sensitive near-infrared spr sensor at 1550 nm. *Plasmonics*, 8(2):619–624, 2013.

[16] S Nivedha, P Ramesh Babu, and K Senthilnathan. Surface plasmon resonance: physics and technology. *Current Science (00113891)*, 115(1), 2018.

[17] Andreas Otto. Excitation of nonradiative surface plasma waves in silver by the method of frustrated total reflection. *Zeitschrift für Physik A Hadrons and nuclei*, 216(4):398–410, 1968.

[18] Erwin Kretschmann and Heinz Raether. Radiative decay of non radiative surface plasmons excited by light. *Zeitschrift für Naturforschung A*, 23(12):2135–2136, 1968.

[19] Claes Nylander, Bo Liedberg, and Tommy Lind. Gas detection by means of surface plasmon resonance. *Sensors and Actuators*, 3:79–88, 1982.

[20] B Liedberg, I Lundström, and E Stenberg. Principles of biosensing with an extended coupling matrix and surface plasmon resonance. *Sensors and Actuators B: Chemical*, 11(1-3):63–72, 1993.

[21] Hyeonjin Park, Tun Naw Sut, Bo Kyeong Yoon, Vladimir P Zhdanov, Nam-Joon Cho, and Joshua A Jackman. Unraveling how multivalency triggers shape deformation of sub-100 nm lipid vesicles. *The Journal of Physical Chemistry Letters*, 12(28):6722–6729, 2021.

[22] Jacob Carroll, Matthew Raum, Kimberly Forsten-Williams, and Uwe C Täuber. Ligand–receptor binding kinetics in surface plasmon resonance cells: a monte carlo analysis. *Physical biology*, 13(6):066010, 2016.

[23] Daniel J Oshannessy, Michael Brighamburke, K Karl Soneson, Preston Hensley, and Ian Brooks. Determination of rate and equilibrium binding constants for macromolecular interactions using surface plasmon resonance: use of nonlinear least squares analysis methods. *Analytical biochemistry*, 212(2):457–468, 1993.

[24] Youjun Zeng, Rui Hu, Lei Wang, Dayong Gu, Jianan He, Shu-Yuen Wu, Ho-Pui Ho, Xuejin Li, Junle Qu, Bruce Zhi Gao, et al. Recent advances in surface plasmon resonance imaging: detection speed, sensitivity, and portability. *Nanophotonics*, 6(5):1017–1030, 2017.

[25] Simona Scarano, Marco Mascini, Anthony PF Turner, and Maria Minunni. Surface plasmon resonance imaging for affinity-based biosensors. *Biosensors and bioelectronics*, 25(5):957–966, 2010.

[26] Christopher Lausted, Zhiyuan Hu, Leroy Hood, and Charles T Campbell. Spr imaging for high throughput, label-free interaction analysis. *Combinatorial chemistry & high throughput screening*, 12(8):741–751, 2009.

[27] Matthew J Linman, Abdennour Abbas, and Quan Cheng. Interface design and multiplexed analysis with surface plasmon resonance (spr) spectroscopy and spr imaging. *Analyst*, 135(11):2759–2767, 2010.

[28] Ganeshram Krishnamoorthy, Edwin T Carlen, Johan G Bomer, Daniël Wijnperlé, Hans L deBoer, Albert van den Berg, and Richard BM Schasfoort. Electrokinetic label-free screening chip: a marriage of multiplexing and high throughput analysis using surface plasmon resonance imaging. *Lab on a Chip*, 10(8):986–990, 2010.

[29] Matthew J Linman, Hai Yu, Xi Chen, and Quan Cheng. Fabrication and characterization of a sialoside-based carbohydrate microarray biointerface for protein binding analysis with surface plasmon resonance imaging. *ACS applied materials & interfaces*, 1(8):1755–1762, 2009.

[30] Chen Zhou, Haimin Zou, Chengjun Sun, Dongxia Ren, Jing Chen, and Yongxin Li. Signal amplification strategies for dna-based surface plasmon resonance biosensors. *Biosensors and Bioelectronics*, 117:678–689, 2018.

[31] Lin He, Emily A Smith, Michael J Natan, and Christine D Keating. The distance-dependence of colloidal au-amplified surface plasmon resonance. *The Journal of Physical Chemistry B*, 108(30):10973–10980, 2004.

[32] Kyeong-Seok Lee and Mostafa A El-Sayed. Gold and silver nanoparticles in sensing and imaging: sensitivity of plasmon response to size, shape, and metal composition. *The Journal of Physical Chemistry B*, 110(39):19220–19225, 2006.

[33] Prashant K Jain, Xiaohua Huang, Ivan H El-Sayed, and Mostafa A El-Sayed. Review of some interesting surface plasmon resonance-enhanced properties of noble metal nanoparticles and their applications to biosystems. *Plasmonics*, 2(3):107–118, 2007.

[34] Geert AJ Besselink, Rob PH Kooyman, Peter JHJ van Os, Gerard HM Engbers, and Richard BM Schasfoort. Signal amplification on planar and gel-type sensor surfaces in surface plasmon resonance-based detection of prostate-specific antigen. *Analytical biochemistry*, 333(1):165–173, 2004.

[35] Erin E Bedford, Jolanda Spadavecchia, Claire-Marie Pradier, and Frank X Gu. Surface plasmon resonance biosensors incorporating gold nanoparticles. *Macromolecular bioscience*, 12(6):724–739, 2012.

[36] Jin-Ha Choi, Jin-Ho Lee, Joohyung Son, and Jeong-Woo Choi. Noble metal-assisted surface plasmon resonance immunosensors. *Sensors*, 20(4):1003, 2020.

[37] EMS Azzam, A Bashir, Osama Shekhah, ARE Alawady, A Birkner, Ch Grunwald, and Ch Wöll. Fabrication of a surface plasmon resonance biosensor based on gold

nanoparticles chemisorbed onto a 1, 10-decanedithiol self-assembled monolayer. *Thin Solid Films*, 518(1):387–391, 2009.

[38] Shuyan Gao, Naoto Koshizaki, Hideo Tokuhisa, Emiko Koyama, Takeshi Sasaki, Jae-Kwan Kim, Joonghyun Ryu, Deok-Soo Kim, and Yoshiki Shimizu. Highly stable au nanoparticles with tunable spacing and their potential application in surface plasmon resonance biosensors. *Advanced Functional Materials*, 20(1):78–86, 2010.

[39] C Lorena Manzanares Palenzuela and Martin Pumera. (bio) analytical chemistry enabled by 3d printing: Sensors and biosensors. *TrAC Trends in Analytical Chemistry*, 103:110–118, 2018.

[40] Pavel N Nesterenko. 3d printing in analytical chemistry: current state and future. *Pure and Applied Chemistry*, 92(8):1341–1355, 2020.

[41] Milena Nadgorny and Amir Ameli. Functional polymers and nanocomposites for 3d printing of smart structures and devices. *ACS applied materials & interfaces*, 10(21):17489–17507, 2018.

[42] Mohamed Sharafeldin, Abby Jones, and James F Rusling. 3d-printed biosensor arrays for medical diagnostics. *Micromachines*, 9(8):394, 2018.

[43] Omar A Mohamed, Syed H Masood, and Jahar L Bhowmik. Optimization of fused deposition modeling process parameters: a review of current research and future prospects. *Advances in Manufacturing*, 3(1):42–53, 2015.

[44] Yuanyuan Xu, Xiaoyue Wu, Xiao Guo, Bin Kong, Min Zhang, Xiang Qian, Shengli Mi, and Wei Sun. The boom in 3d-printed sensor technology. *Sensors*, 17(5):1166, 2017.

[45] Jose Muñoz and Martin Pumera. 3d-printed biosensors for electrochemical and optical applications. *TrAC Trends in Analytical Chemistry*, 128:115933, 2020.

[46] Hoon Yeub Jeong, Eunsongyi Lee, Soo-Chan An, Yeonsoo Lim, and Young Chul Jun. 3d and 4d printing for optics and metaphotonics. *Nanophotonics*, 9(5):1139–1160, 2020.

[47] Miroslav Pohanka. Three-dimensional printing in analytical chemistry: principles and applications. *Analytical Letters*, 49(18):2865–2882, 2016.

[48] Alexander Lambert, Santino Valiulis, and Quan Cheng. Advances in optical sensing and bioanalysis enabled by 3d printing. *ACS sensors*, 3(12):2475–2491, 2018.

[49] MF Santangelo, S Libertino, APF Turner, Daniel Filippini, and Wing Cheung Mak. Integrating printed microfluidics with silicon photomultipliers for miniaturised and highly sensitive atp bioluminescence detection. *Biosensors and Bioelectronics*, 99:464–470, 2018.

[50] Ho Nam Chan, Yiwei Shu, Bin Xiong, Yangfan Chen, Yin Chen, Qian Tian, Sean A Michael, Bo Shen, and Hongkai Wu. Simple, cost-effective 3d printed microfluidic components for disposable, point-of-care colorimetric analysis. *Acs Sensors*, 1(3):227–234, 2016.

[51] Maria Bauer and Lawrence Kulinsky. Fabrication of a lab-on-chip device using material extrusion (3d printing) and demonstration via malaria-ab elisa. *Micromachines*, 9(1):27, 2018.

[52] ChenGuang Zhang, Chen Ching-Jung, Kalpana Settu, and Liu Jen-Tsai. Angle-scanning surface plasmon resonance system with 3d printed components for biorecognition investigation. *Advances in Condensed Matter Physics*, 2018, 2018.

[53] Samuel S Hinman, Kristy S McKeating, and Quan Cheng. Plasmonic sensing with 3d printed optics. *Analytical chemistry*, 89(23):12626–12630, 2017.

[54] Jaime Castillo-León. Microfluidics and lab-on-a-chip devices: history and challenges. In *Lab-on-a-Chip Devices and Micro-Total Analysis Systems*, pages 1–15. Springer, 2015.

[55] George M Whitesides. The origins and the future of microfluidics. *nature*, 442(7101):368–373, 2006.

[56] Todd M. Squires and Stephen R. Quake. Microfluidics: Fluid physics at the nanoliter scale. *Rev. Mod. Phys.*, 77:977–1026, Oct 2005.

[57] Shaurya Prakash, Aigars Piruska, Enid N. Gatimu, Paul W. Bohn, Jonathan V. Sweedler, and Mark A. Shannon. Nanofluidics: Systems and applications. *IEEE Sensors Journal*, 8(5):441–450, 2008.

[58] Sanjeeva Balasuriya. Dynamical systems techniques for enhancing microfluidic mixing. *Journal of Micromechanics and Microengineering*, 25(9):094005, 2015.

[59] Adelina-Gabriela Niculescu, Cristina Chircov, Alexandra Cătălina Bîrcă, and Alexandru Mihai Grumezescu. Fabrication and applications of microfluidic devices: A review. *International Journal of Molecular Sciences*, 22(4):2011, 2021.

[60] João Pedro Martins, Giulia Torrieri, and Hélder A Santos. The importance of microfluidics for the preparation of nanoparticles as advanced drug delivery systems. *Expert opinion on drug delivery*, 15(5):469–479, 2018.

[61] Matthew James, Richard A Revia, Zachary Stephen, and Miqin Zhang. Microfluidic synthesis of iron oxide nanoparticles. *Nanomaterials*, 10(11):2113, 2020.

[62] Prashant L Suryawanshi, Shirish H Sonawane, Bharat A Bhanvase, Muthupandian Ashokkumar, Makarand S Pimplapure, and Parag R Gogate. Synthesis of iron oxide nanoparticles in a continuous flow spiral microreactor and corning® advanced flow™ reactor. *Green Processing and Synthesis*, 7(1):1–11, 2018.

[63] Qinlei Liu, Yao Lin, Jing Xiong, Li Wu, Xiandeng Hou, Kailai Xu, and Chengbin Zheng. Disposable paper-based analytical device for visual speciation analysis of ag (i) and silver nanoparticles (agnps). *Analytical chemistry*, 91(5):3359–3366, 2019.

[64] Yajun Zhang, Jingji Liu, Hongliang Wang, and Yiqiang Fan. Laser-induced selective wax reflow for paper-based microfluidics. *RSC advances*, 9(20):11460–11464, 2019.

[65] Amid Shakeri, Noor Abu Jarad, Ashlyn Leung, Leyla Soleymani, and Tohid F Didar. Biofunctionalization of glass-and paper-based microfluidic devices: A review. *Advanced Materials Interfaces*, 6(19):1900940, 2019.

[66] Chang-Ming Wang, Chong-You Chen, and Wei-Ssu Liao. Enclosed paper-based analytical devices: Concept, variety, and outlook. *Analytica Chimica Acta*, 1144:158–174, 2021.

[67] Jihong Hwang, Young Hak Cho, Min Soo Park, and Bo Hyun Kim. Microchannel fabrication on glass materials for microfluidic devices. *International Journal of Precision Engineering and Manufacturing*, 20(3):479–495, 2019.

[68] Indalesio Rodriguez, Paolo Spicar-Mihalic, Christopher L Kuyper, Gina S Fiorini, and Daniel T Chiu. Rapid prototyping of glass microchannels. *Analytica Chimica Acta*, 496(1-2):205–215, 2003.

[69] Marc A Unger, Hou-Pu Chou, Todd Thorsen, Axel Scherer, and Stephen R Quake. Monolithic microfabricated valves and pumps by multilayer soft lithography. *Science*, 288(5463):113–116, 2000.

[70] Jaroslav Kotowski, Vít Navrátil, Zdeněk Slouka, and Dalimil Šnita. Fast and simple fabrication procedure of whole-glass microfluidic devices with metal electrodes. *Microelectronic engineering*, 110:441–445, 2013.

[71] Valia Fascio, Rolf Wuthrich, Didier Viquerat, and Hans Langen. 3d microstructuring of glass using electrochemical discharge machining (ecdm). In *MHS'99. Proceedings of 1999 International Symposium on Micromechatronics and Human Science (Cat. No. 99TH8478)*, pages 179–183. IEEE, 1999.

[72] Li Li, Takashi Abe, and Masayoshi Esashi. Smooth surface glass etching by deep reactive ion etching with sf 6 and xe gases. *Journal of Vacuum Science & Technology B: Microelectronics and Nanometer Structures Processing, Measurement, and Phenomena*, 21(6):2545–2549, 2003.

[73] Thierry Corman, Peter Enoksson, and Göran Stemme. Deep wet etching of borosilicate glass using an anodically bonded silicon substrate as mask. *Journal of micromechanics and microengineering*, 8(2):84, 1998.

[74] JH Giovanola and I Finnie. On the machining of glass. *Journal of Materials Science*, 15(10):2508–2514, 1980.

[75] PJ Slikkerveer, PCP Bouten, and FCM De Haas. High quality mechanical etching of brittle materials by powder blasting. *Sensors and actuators A: Physical*, 85(1-3):296–303, 2000.

[76] X-Q Sun, T Masuzawa, and M Fujino. Micro ultrasonic machining and self-aligned multilayer machining/assembly technologies for 3d micromachines. In *Proceedings of ninth international workshop on micro electromechanical systems*, pages 312–317. IEEE, 1996.

[77] G Allcock, PE Dyer, G Elliner, and HV Snelling. Experimental observations and analysis of co2 laser-induced microcracking of glass. *Journal of applied physics*, 78(12):7295–7303, 1995.

[78] Shamim Ahsan and Man Seop Lee. Femtosecond laser induced nanostructures in soda-lime glass. *Journal of Laser Micro/Nanoengineering*, 7(2), 2012.

[79] Hiroyuki Niino, Yoshimi Yasui, Ximing Ding, Aiko Narazaki, Tadatake Sato, Yoshizo Kawaguchi, and Akira Yabe. Surface micro-fabrication of silica glass by excimer laser irradiation of organic solvent. *Journal of Photochemistry and Photobiology A: Chemistry*, 158(2-3):179–182, 2003.

[80] Simon M Scott and Zulfiqur Ali. Fabrication methods for microfluidic devices: An overview. *Micromachines*, 12(3):319, 2021.

[81] Jacob B Nielsen, Robert L Hanson, Haifa M Almughamsi, Chao Pang, Taylor R Fish, and Adam T Woolley. Microfluidics: Innovations in materials and their fabrication and functionalization. *Analytical chemistry*, 92(1):150–168, 2019.

[82] Shantanu Bhattacharya, Arindom Datta, Jordan M Berg, and Shubhra Gangopadhyay. Studies on surface wettability of poly (dimethyl) siloxane (pdms) and glass under oxygen-plasma treatment and correlation with bond strength. *Journal of microelectromechanical systems*, 14(3):590–597, 2005.

[83] Gregor Weisgrab, Aleksandr Ovsianikov, and Pedro F Costa. Functional 3d printing for microfluidic chips. *Advanced Materials Technologies*, 4(10):1900275, 2019.

[84] Lujun Wang and Martin Pumera. Recent advances of 3d printing in analytical chemistry: Focus on microfluidic, separation, and extraction devices. *TrAC Trends in Analytical Chemistry*, 135:116151, 2021.

[85] Reza Amin, Stephanie Knowlton, Alexander Hart, Bekir Yenilmez, Fariba Ghaderinezhad, Sara Katebifar, Michael Messina, Ali Khademhosseini, and Savas Tasoglu. 3d-printed microfluidic devices. *Biofabrication*, 8(2):022001, 2016.

[86] HS Santana, JL Silva, B Aghel, and J Ortega-Casanova. Review on microfluidic device applications for fluids separation and water treatment processes. *SN Applied Sciences*, 2(3):1–19, 2020.

[87] Yury Voloshin, Raghunath Halder, and Adeniyi Lawal. Kinetics of hydrogen peroxide synthesis by direct combination of h2 and o2 in a microreactor. *Catalysis Today*, 125(1-2):40–47, 2007.

[88] Samuel K Sia and George M Whitesides. Microfluidic devices fabricated in poly (dimethylsiloxane) for biological studies. *Electrophoresis*, 24(21):3563–3576, 2003.

[89] Adeniyi Lawal, Woo Lee, Ron Besser, Donald Kientzler, and Luke Achenie. Microchannel reactor system for catalytic hydrogenation. Technical report, Stevens Institute of Technology, 2010.

[90] Catherine J Harrison, Yann A Le Gouellec, Robert C Cheng, and Amy E Childress. Bench-scale testing of nanofiltration for seawater desalination. *Journal of environmental engineering*, 133(11):1004–1014, 2007.

[91] Lingyong Wei, Shaohui Guo, Guangxu Yan, Chunmao Chen, and Xiaoyan Jiang. Electrochemical pretreatment of heavy oil refinery wastewater using a three-dimensional electrode reactor. *Electrochimica Acta*, 55(28):8615–8620, 2010.

[92] Burcu Gumuscu, Johan G Bomer, Hans L De Boer, Albert Van Den Berg, and Jan CT Eijkel. Exploiting biased reptation for continuous flow preparative dna fractionation in a versatile microfluidic platform. *Microsystems & nanoengineering*, 3(1):1–8, 2017.

[93] Francis Cui, Minsoung Rhee, Anup Singh, and Anubhav Tripathi. Microfluidic sample preparation for medical diagnostics. *Annual review of biomedical engineering*, 17:267–286, 2015.

[94] Beom Seok Lee, Jung-Nam Lee, Jong-Myeon Park, Jeong-Gun Lee, Suhyeon Kim, Yoon-Kyoung Cho, and Christopher Ko. A fully automated immunoassay from whole blood on a disc. *Lab on a Chip*, 9(11):1548–1555, 2009.

[95] Yatian Qu, Lewis A Marshall, and Juan G Santiago. Simultaneous purification and fractionation of nucleic acids and proteins from complex samples using bidirectional isotachophoresis. *Analytical chemistry*, 86(15):7264–7268, 2014.

[96] GT Vladisavljević, Isao Kobayashi, and Mitsutoshi Nakajima. Production of uniform droplets using membrane, microchannel and microfluidic emulsification devices. *Microfluidics and nanofluidics*, 13(1):151–178, 2012.

[97] Brian M Paegel, Robert G Blazej, and Richard A Mathies. Microfluidic devices for dna sequencing: sample preparation and electrophoretic analysis. *Current opinion in biotechnology*, 14(1):42–50, 2003.

[98] Hanyoup Kim, Michael S Bartsch, Ronald F Renzi, Jim He, James L Van de Vreugde, Mark R Claudnic, and Kamlesh D Patel. Automated digital microfluidic sample preparation for next-generation dna sequencing. *JALA: Journal of the Association for Laboratory Automation*, 16(6):405–414, 2011.

[99] Jin-Zheng Wang, Lin-Lin Zhu, Fan Zhang, Richard Ansah Herman, Wen-Jing Li, Xue-Jiao Zhou, Fu-An Wu, and Jun Wang. Microfluidic tools for lipid production and modification: a review. *Environmental Science and Pollution Research*, 26(35):35482–35496, 2019.

[100] Lindong Weng, Felix Ellett, Jon Edd, Keith HK Wong, Korkut Uygun, Daniel Irimia, Shannon L Stott, and Mehmet Toner. A highly-occupied, single-cell trapping microarray for determination of cell membrane permeability. *Lab on a Chip*, 17(23):4077–4088, 2017.

[101] Xiaojun Feng, Bi-Feng Liu, Jianjun Li, and Xin Liu. Advances in coupling microfluidic chips to mass spectrometry. *Mass spectrometry reviews*, 34(5):535–557, 2015.

[102] Wang-Chou Sung, Honest Makamba, and Shu-Hui Chen. Chip-based microfluidic devices coupled with electrospray ionization-mass spectrometry. *Electrophoresis*, 26(9):1783–1791, 2005.

[103] Gary A Schultz, Thomas N Corso, Simon J Prosser, and Sheng Zhang. A fully integrated monolithic microchip electrospray device for mass spectrometry. *Analytical Chemistry*, 72(17):4058–4063, 2000.

[104] Pamela N Nge, Chad I Rogers, and Adam T Woolley. Advances in microfluidic materials, functions, integration, and applications. *Chemical reviews*, 113(4):2550–2583, 2013.

[105] Anas El-Aneed, Aljandro Cohen, and Joseph Banoub. Mass spectrometry, review of the basics: electrospray, maldi, and commonly used mass analyzers. *Applied Spectroscopy Reviews*, 44(3):210–230, 2009.

[106] Michael Balazy. Eicosanomics: targeted lipidomics of eicosanoids in biological systems. *Prostaglandins & other lipid mediators*, 73(3-4):173–180, 2004.

[107] Ivo Glynne Gut. Dna analysis by maldi-tof mass spectrometry. *Human mutation*, 23(5):437–441, 2004.

[108] David J Harvey. Matrix-assisted laser desorption/ionization mass spectrometry of carbohydrates and glycoconjugates. *International Journal of Mass Spectrometry*, 226(1):1–35, 2003.

[109] Guilin Chen, Minxia Fan, Ye Liu, Baoqing Sun, Meixian Liu, Jianlin Wu, Na Li, and Mingquan Guo. Advances in ms based strategies for probing ligand-target interactions: Focus on soft ionization mass spectrometric techniques. *Frontiers in chemistry*, 7:703, 2019.

[110] Renato Zenobi and Richard Knochenmuss. Ion formation in maldi mass spectrometry. *Mass spectrometry reviews*, 17(5):337–366, 1998.

[111] Ivan Talian, Andrej Orinák, Jan Preisler, Andreas Heile, Lucie Onofrejová, Dušan Kaniansky, and Heinrich F Arlinghaus. Comparative tof-sims and maldi tof-ms analysis on different chromatographic planar substrates. *Journal of separation science*, 30(16):2570–2582, 2007.

[112] Gary A Breaux, Kari B Green-Church, Amy France, and Patrick A Limbach. Surfactant-aided, matrix-assisted laser desorption/ionization mass spectrometry of hydrophobic and hydrophilic peptides. *Analytical chemistry*, 72(6):1169–1174, 2000.

[113] Antony Croxatto, Guy Prod'hom, and Gilbert Greub. Applications of maldi-tof mass spectrometry in clinical diagnostic microbiology. *FEMS microbiology reviews*, 36(2):380–407, 2012.

[114] Beate Fuchs, Rosmarie Süß, and Jürgen Schiller. An update of maldi-tof mass spectrometry in lipid research. *Progress in lipid research*, 49(4):450–475, 2010.

[115] Min Li, Li Yang, Yu Bai, and Huwei Liu. Analytical methods in lipidomics and their applications. *Analytical chemistry*, 86(1):161–175, 2014.

[116] Beate Fuchs and Jürgen Schiller. Application of maldi-tof mass spectrometry in lipidomics. *European Journal of Lipid Science and Technology*, 111(1):83–98, 2009.

[117] J Schiller, R Süß, J Arnhold, B Fuchs, J Lessig, M Müller, M Petković, H Spalteholz, O Zschörnig, and K Arnold. Matrix-assisted laser desorption and ionization time-of-flight (maldi-tof) mass spectrometry in lipid and phospholipid research. *Progress in lipid research*, 43(5):449–488, 2004.

[118] Jenny Leopold, Yulia Popkova, Kathrin M Engel, and Jürgen Schiller. Recent developments of useful maldi matrices for the mass spectrometric characterization of lipids. *Biomolecules*, 8(4):173, 2018.

Chapter 2

Multifunctional Nanoclusters by Nanoparticle-Coupled Liposomes for Enhanced Plasmonic Biosensing with the Supported Lipid Membrane Interface

2.1 ABSTRACT

We report the fabrication of stable nanoclusters by salt-induced coupling of nanoparticles onto functionalized liposomes and their application in enhanced biosensing on a biomimetic surface. The coupling of nanoparticle-liposome structures and the subsequent

uncoupled large nanoparticle clusters removal were characterized by transmission electron microscopy (TEM) and absorption spectra. These nanoclusters were then tested for signal amplification with surface plasmon resonance (SPR), demonstrating advantages of an effective amplification by combining the large mass of lipid vesicles and the plasmonic properties of noble metal nanoparticles. Using 13nm AuNPs-POPC nanoclusters, bacterial toxin detection was drastically enhanced with a markedly low nonspecific background, reaching a LOD of 0.1 ng/mL on a supported membrane interface. The nanoclusters prove to be a highly robust and reproducible signal amplification tag for optical biosensing, and also demonstrated a long shelf life, remain effective for over four weeks before showing signs of deterioration. A comparison between different types and sizes of noble metal nanoparticles with POPC liposomes was conducted and their effectiveness on amplification was assessed. The simple preparation procedure of liposome-nanoparticle nanoclusters reported here offers a promising bio-nanomaterial for sensitive biosensing and studies of vesicles-cell membrane interactions.

2.2 INTRODUCTION

Cell membranes play an essential role in the segregation of cellular contents from the external environment, signal transduction, and molecular recognition [1].There is significant interest in mimicking natural cell membranes with self-assembled lipid membranes as they remain chemically and electrically insulating and offer great potentials in biology and bioanalysis [2].Typical lipid assemblies include planar lipid membranes and spherical liposomes [3], which are ideal models due to their similar physicochemical properties such

as high fluidity and mobility [4].Currently, supported lipid membranes have been broadly used to study protein-cell membrane interactions [4] [5] [6], transmembrane transport [7] [8], T cell activation [9], vesicle adsorption behaviors [10], and generation of biosensing microarrays [11] [12].By forming supported lipid bilayers on a calcinated silicate surface on gold [13], surface plasmon resonance (SPR) biosensing can be conducted, which allows for study of membrane-protein recognition [4] and polymeric coating in a label-free fashion [5]. Calcinated surface can also effectively suppress nonspecific binding in SPR sensing, which is a high advantage [14]. For some extremely demanding tasks, however, conventional detection may not have sufficient sensitivity when dealing with trace amount of analytes [15], therefore signal amplification is needed. In recent years, a number of signal amplification strategies have been reported to improve SPR sensitivity [16] [17] [18].However, the fragile nature of lipid membranes and the need for a continuous hydrated environment have made signal amplification on a lipid membrane interface very challenging, and only limited success has occurred [13].

Noble metal nanoparticles, especially gold nanoparticles (AuNPs) and silver nanoparticles (AgNPs), have garnered tremendous attention as localized surface plasmon resonance (LSPR) sensors [19] [20] [21]. LSPR of nanoparticles can also be coupled with propagating surface plasmon polaritons to generate a larger field enhancement that further improves detection sensitivity [22]. However, biofunctionalization of nanoparticles without compromising their stability and performance in sensing has been a challenge, especially for nanoparticles with poor stability [23]. A common approach to functionalizing AuNPs is modifying them with thiolated biomacromolecules and antibodies via gold-thiol bond or

direct adsorption of proteins via electrostatics interaction [24].However, the sulfhydrylation of biomacromolecules and the salt aging process is time-consuming and further complicates preparation steps. The stability of nanoparticle-antibody composites via electrostatic adsorption can be problematic due to the high possibility of the protein desorption on the surface of functionalized AuNPs [25] [26].

Liposomes have been utilized as a drug delivery vehicle and as the material for biosensing due to simple preparation, high biocompatibility and large surface area [27] [28]. The encapsulation properties and large surface area of liposomes have been utilized for signal amplification for colorimetric [29], fluorescent [30] and SPR sensing [31] [32]. Coupling liposomes with metal nanoparticles has generated interest due to the prospect of low toxicity in drug delivery [33] and stability enhancement of membranes [34]. Liposome-metal nanoparticles system have been used as an efficient tool for photothermal therapy [33] and study of interactions between halide capped nanoparticles and liposomes [35]. Normally, the preparation of liposome-nanoparticle composites requires in-situ synthesis or a separation procedure that makes the process cumbersome. Sugikawa et al. reported preparing liposome-gold nanoparticles by a simple mixing process and studied the relationship between fluidization of lipid and nanoparticles assembly onto the DPPC liposomes [36]. However, precipitates were observed in a few hours after mixing at 25℃ indicating the destabilization of the nano composites.

In this paper, we report a simple and highly reproducible approach for generating robust and stable liposome-nanoparticles for sensing enhancement. The charged groups that stabilize noble metal nanoparticles were electrostatically screened by the addition of

salt. Nanoparticles of different sizes were assembled on POPC liposomes and their stability and use as signal amplification reagents for SPR sensing were characterized. The large mass of liposome-nanoparticles nanoclusters and the LSPR coupling effect of the nanoparticles showed enhanced signal amplification as compared to DNA stabilized AuNPs and POPC liposomes. In addition to signal amplification, this hybrid bio-nanomaterial demonstrated ultra-low non-specific binding on the bilayer sensing surface, suggesting a novel sensing platform that may open new avenues for interaction study between vesicles and cell membranes in living organisms.

2.3 EXPERIMENTAL

2.3.1 Materials and Instrumentation

Gold(III) chloride trihydrate, trisodium citrate dihydrate, ethylenediaminetetraacetic acid (EDTA), sodium hydroxide, silver nitrate, cholera toxin from vibrio cholerae (CT), biotinylated anti-cholera toxin antibody from rabbit were purchased from Sigma-Aldrich (St. Louis, MO). Streptavidin was from Thermo Scientific (Rockford, IL). Monosialoganglioside receptor (GM1) was obtained from Matreya (Pleasant Gap, PA). 1-Oleoyl-2-palmitoyl-sn-glycero-3-phosphocholine (POPC) and 1,2-dipalmitoyl-sn-glycero-3-phosphoethanolamine-N-(biotinyl) sodium salt (biotin-PE) were obtained from Avanti Polar Lipids (Alabaster, AL). Biotinylated oligonucleotides T20 were obtained from Integrated DNA Technologies (Coralville, IA).

Absorbance spectra were collected with Cary 50 UV−vis spectrophotometer (Agilent Technologies, Santa Clara, CA). Nanoparticle tracking analysis (NTA) was obtained by

NanoSight NS300 (Malvern Instruments, Malvern, UK). Transmission electron microscopy (TEM) images were obtained by Phillips FEI Tecnai 12 TEM (Andover, MA) in CFAMM of UCR. Surface plasmon resonance (SPR) assays were carried out with a NanoSPR3 device with dual channel (NanoSPR, Addison, IL). The running buffer for all SPR assays was 20 mM phosphate buffered saline (PBS) (containing 150 mM NaCl, pH 7.4).

2.3.2 Nanoparticles Preparation

The citrate stabilized 13nm, 25nm gold nanoparticles and EDTA-capped silver nanoparticles (AgNPs) were prepared according to the standard procedure which has been reported in the previous literatures [37] [38] [39]. DNA functionalized 13nm citrate stabilized gold nanoparticles were prepared by using thiolated oligonucleotides, which has been demonstrated by Hinman et al [25]. and Hurst et al [40]. Briefly, 25μL of 100μM biotin functionalized, 20-nucleotide thiolated polythymine (T_{20}) was added to 1mL of 3.9nM citrate stabilized 13nm AuNPs solution. After mixing with 20μL of 500mM citrate-HCl (pH=3.0), the solution was sonicated for 25s. The solution was then mixed with 34μL and 241μL of 5M NaCl solution in sequence to increase the surface coverage of DNA. The solution was placed in the fridge (4 °C) overnight and was purified by centrifugal filtration to remove excess salt the following day. All nanoparticles solutions were stored at 4 °C before use.

2.3.3 Liposome-Nanoparticles Preparation

For the preparation of GM1-POPC-AuNPs, a mixture containing 200μL of POPC stock solution (5mg/mL in chloroform) and 21.1μL of GM1 stock solution (5mg/mL in chloroform) was transferred in a glass vial and dried under nitrogen to form a thin lipid

film (for biotin-POPC-AuNPs preparation, 200μL of POPC stock solution was mixed with 6.28μL of 10mg/mL biotin-PE stock solution). The glass vial was then placed in a vacuum desiccator overnight [13] [41]. The lipid film was rehydrated with 250μL 13nm AuNPs solution (3.9nM). For POPC-AgNPs and POPC-25nm AuNPs preparation, the lipid film was resuspended in 250μL 0.2nM EDTA-AgNPs solution and 250μL 0.6nM 25nm AuNPs solution, respectively. The solution was then treated by 5s of vortexing and 35min of bath sonication to form liposome-nanoparticles precursors. The solution was then extruded at least 11 times through a polycarbonate membrane with 100nm pores to generate unilamellar liposome-nanoparticles assemblies with consistent size. Next, 6μL of 5M NaCl solution was added to 200μL assembly solution to induce the nanoparticle/liposome coupling and aggregation of free nanoparticles in the solution. The solution was then centrifuged at 1500rpm for 2 min to remove aggregated nanoparticles. The supernatant was collected and stored at 4 ℃ before use.

2.3.4 SPR Calcinated Gold Chip Preparation

BK-7 microscope slides were cleaned with piranha solution (Caution!), rinsed with nanopure water, and dried by compressed air. A 2nm chromium film, followed by 50nm gold film, was deposited on the surface of the slides via e-beam evaporation. Finally, a 4nm SiO_2 film was deposited on top of the gold layer via plasmon enhanced chemical vapor deposition (PECVD) system [12].

2.3.5 Transmission Electron Microscopy

Formvar carbon coated copper grids were used for preparing specimen for TEM. All the samples were stained with 2% uranyl acetate for 1 min [42]. The grids were then placed on the drop of 1% methylecellulose for 1 min. After removing excess methylcellulose by filter paper, the grids were dried in the air and were ready for image on TEM.

2.3.6 CT Assay and Signal Amplification of Liposome-Nanoparticles

POPC vesicle solution containing 5% biotin-PE in PBS was firstly injected to the channel to form a lipid bilayer on the calcinated gold chip [13]. 500μg/mL streptavidin solution in PBS was then injected, which was followed by injection of 500μg/mL biotinylated anti-CT solution for capture of CT in different concentrations. After incubation for 50 min and rinse with PBS buffer, GM1-POPC-13nm AuNPs solution was injected. The excess liposome-nanoparticles were removed by rinsing with PBS buffer for 20min after incubation.

2.4 RESULTS AND DISCUSSION

2.4.1 Salt-Induced AuNP Assembly on the Liposomes

The preparation of the AuNP/liposome assembly was achieved by a salt-induced process. Figure 2.1 shows the general scheme for the preparation of Biotin-POPC-13nm AuNPs. The lipids were rehydrated in a citrate stabilized AuNPs solution for 10 minutes. Once resuspended in the AuNP solution, the mixture was treated with bath sonication. The solution was then extruded with a 100nm pore-size membrane to generate vesicles, and

then treated with salt to induce liposome-cluster formation. Large nanoparticle aggregates were removed by low-speed centrifugation.

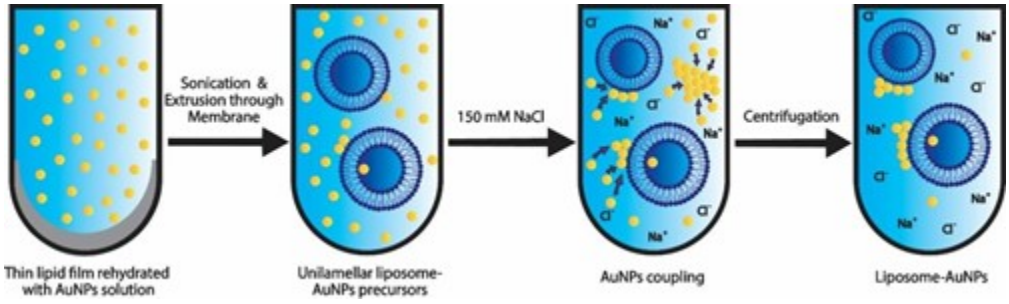

Figure 2.1: The scheme for preparation of liposome-nanoparticle clusters.

UV-vis spectroscopy was first utilized to characterize nanoparticle aggregation in different media (Figure 2.2A). We normalized the spectra by setting the peak intensity to be the same for easier comparison. The absorbance peaks showed similar shapes after sonication and extrusion, indicating limited aggregation of AuNPs before the addition of salt. After salt addition, the absorbance peak became broader, suggesting an aggregation process of AuNPs, which is consistent with literature reports [43] [44]. After centrifugation, the absorption peak became sharper than those treated with salt but broader than the original AuNPs solution, indicating that a substantial degree of AuNP clusters were removed. The assemblies were further characterized by transmission electron microscopy (TEM) (Figure 2.2C&D), which clearly indicates that NaCl promotes AuNP aggregation and AuNP coupling to the POPC liposome surface (Figure 2.2C).

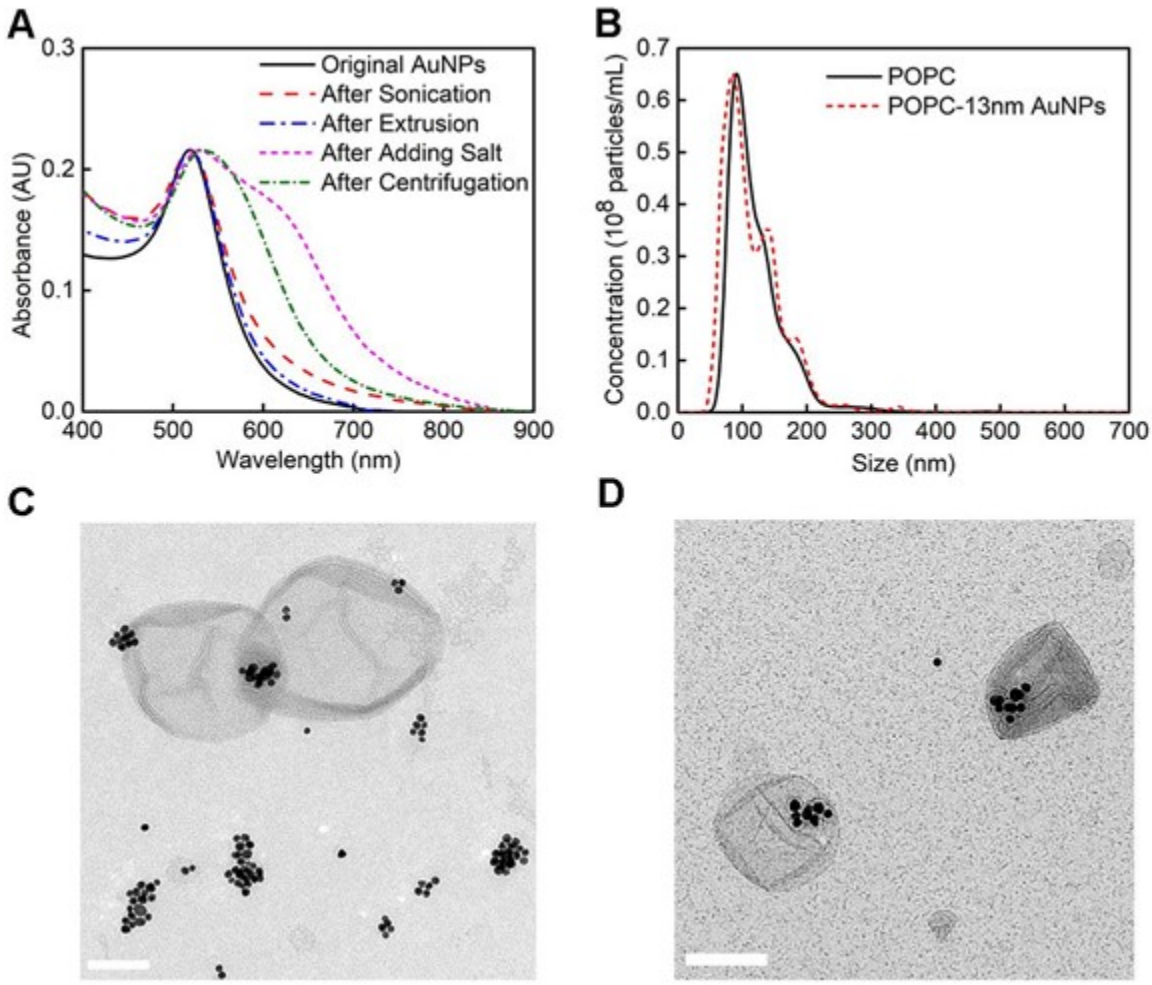

Figure 2.2: Salt-induced nanoparticles assembly on liposomes. (A) Absorbance spectra of samples after each step of preparation. (B) Size distribution of POPC liposomes and POPC-AuNPs via NTA. (C) TEM image of the sample after adding salt. Bar=100nm. (D) TEM image of the sample after centrifugation. Bar=100nm.

The removal of large clusters was also observed after centrifugation (Figure 2.2D). Further study using nanoparticle tracking analysis (NTA) showed no major difference in size between POPC−AuNPs (mean size: 116.0 ± 1.2 nm) and POPC liposomes (mean size: 120.7 ± 1.3 nm) (Figure 2.2B). The coupling of the AuNPs on to POPC liposomes was also confirmed by comparation UV−Vis spectra of POPC liposomes, AuNPs, POPC liposomes mixed with AuNPs (directly after mixing) and AuNPs-POPC composites (Figure 2.3). When liposomes were directly mixed with AuNPs, the UV-Vis curve is very closed to the original AuNPs solution, with the peak on the left of the AuNPs−coupled POPC vesicles in the spectra.

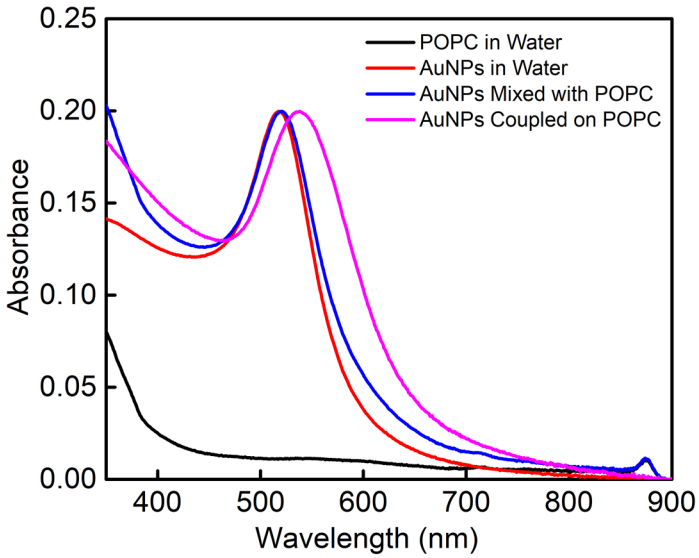

Figure 2.3: UV-Vis Spectra Comparison of POPC liposomes, AuNPs, POPC liposomes mixed with AuNPs (directly after mixing) and AuNPs-POPC composites.

The TEM and NTA data prove the formation of liposome−AuNP nanoclusters but where the AuNPs distribute can be ambiguous. After bath sonication and extrusion, a small amount of nanoparticles were likely trapped inside or absorbed onto the outer interface of liposomes during vesicle formation, due to Van der Waals force [36], electrostatic interaction [45] [46] and hydrophilic properties of citrate stabilized AuNPs [47]. After adding salt, more AuNPs started to adsorb onto the liposome surface, while the AuNPs suspended in solution began to aggregate to form large clusters [44] and get removed by low speed centrifugation. The exoneration of the clusters resulted in less absorbance of light of the solution and precipitation of nanoparticles onto the walls of the centrifuge tube (Figure 2.4).

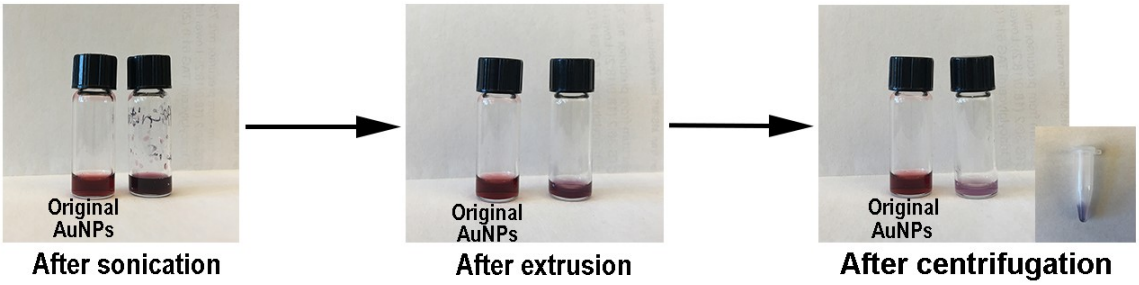

Figure 2.4: Pictures of preparation of POPC-13nm AuNPs.

2.4.2 Signal Amplification of POPC-13nm AuNPs on SPR

We then tested signal amplification of SPR biosensing by injecting biotin−POPC−AuNPs into the solution over a biotin−POPC bilayer−streptavidin interface for the detection of streptavidin (Figure 2.5A&B). The angular shift yields a large increase by more than 1.00 degrees, suggesting biotin−POPC−AuNP assembly is specific and effective. Biofunctionalized AuNPs have been commonly used and extensively studied as signal amplification tags on SPR [48]. Multiple stabilizers have been investigated to couple with AuNPs to ensure their stability in biological media [49]. Among these AuNPs functionalization methods, DNA coated AuNPs shows excellent stability and versatility and similar amplification on SPR has been conducted with functional DNA−AuNPs [25] [50] [51]. Considering this, the performance of biotin−POPC−AuNPs was compared to DNA−AuNPs as well as biotin−POPC liposomes (Figure 2.5C&D). NTA and absorption spectroscopy were utilized to determine the average concentration of POPC−AuNPs and DNA−AuNPs, which were both set at 1nM [37]. From Figure 2.5, POPC−AuNP assembly generated a signal increased by 0.788 degrees, which is 6.6 times greater than DNA−AuNPs. Between biotin−POPC−AuNP assembly and biotin−POPC liposomes, the former showed a 1.5 times signal increase on the bilayer interface and 2.5 times increase on a gold surface as compared to POPC liposomes of the same concentration (Figure 2.6).

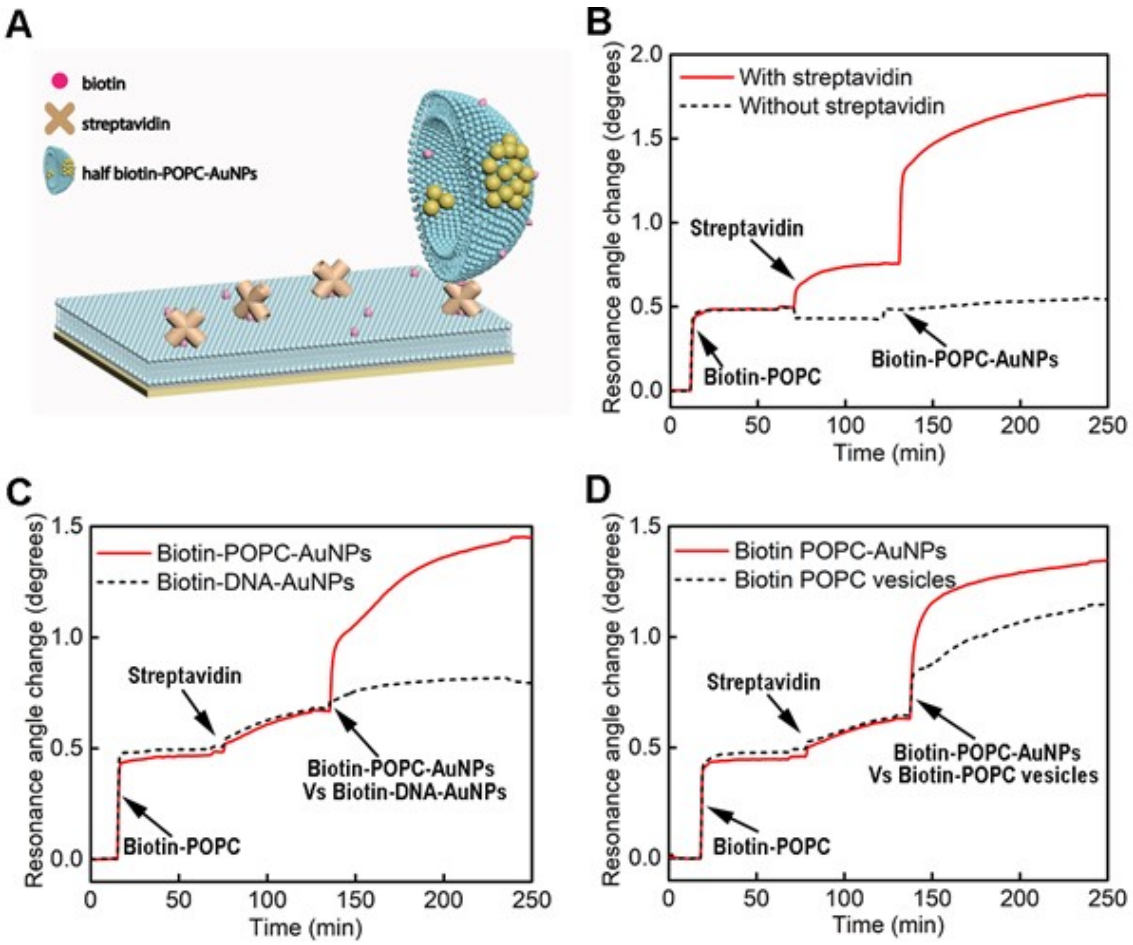

Figure 2.5: Signal amplification of liposome-nanoparticles. (A) 3D scheme of surface chemistry on SPR for signal amplification and vesicles-cell membrane interactions study. (B) SPR sensorgram for signal changes after injecting biotin-POPC-AuNPs on a bilayer interface with and without streptavidin. (C) SPR sensorgram for signal changes of the same concentrations of biotin-POPC-AuNPs (13 nm) and biotin-DNA AuNPs (13 nm) binding to streptavidin on the bilayer interface. (D) SPR sensorgram for signal changes of biotin-POPC liposomes and biotin-POPC-AuNPs (13 nm) with the same concentration binding to streptavidin on the bilayer interface.

The marked enhancement in signal amplification by POPC−AuNP assembly can be attributed to several factors. The plasmon coupling between the metal nanoparticle LSPR and the propagating surface plasmon polariton (SPP) on the gold film could be an important one [52] [53]. In addition, SPR is known to be highly sensitive to small change of refractive index caused by captured biomolecules [54], especially of those with large mass such as lipid vesicles and metal nanoparticles. The combination of the large mass of liposome−nanoparticles and the plasmon coupling effect appears to be an ideal signal enhancement strategy. Compared to a single nanoparticle or liposome, liposome−nanoparticles nanoclusters show obvious advantages in coupling multiple nanoparticles and low non−specific binding.

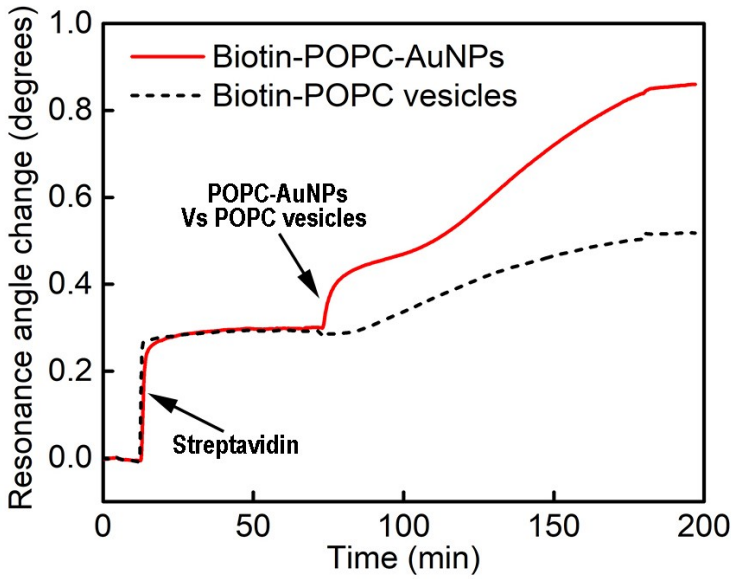

Figure 2.6: Signal comparison of Biotin-POPC-AuNPs and Biotin-POPC vesicles binding onto the streptavidin adsorbed on bare gold surface.

Further study on amplification performance of the POPC−AuNPs nanoclusters was carried out with GM1−POPC−13nm AuNPs for detection of cholera toxin, CT (Figure 2.7A&B). CT is a bacterial toxin secreted by *Vibrio cholera*, which is known to target the membrane receptor monosialoganglioside GM1. In this work, a lipid bilayer of POPC mixed with 5% of biotin−PE was first formed on the calcinated gold surface. After the injection of streptavidin solution, the biotinylated anti−CT antibody was immobilized on the bilayer interface via streptavidin−biotin interaction. The toxin was then captured by the surface−bound antibody and the capture was amplified by GM1−embedded POPC−AuNPs nanoclusters. From the sensorgrams in Figures 2.7B&C, an angular shift of 0.374 degrees was observed for 5μg/mL CT with low nonspecific background, yielding almost 40 times amplification as compared to the native protein capture. A calibration curve was generated for CT detection from 0.1ng/mL to 1μg/mL, yielding a linear fit with R^2=0.9726 (Figure 2.7D). Using the 3 S/N principle, the detection limit can go down to 0.1ng/mL. The blank value refers to the non−specific binding of POPC−AuNPs with no CT injected. The signal generated only by CT is low and show no differentiation, however with the dramatic signal amplification of the POPC−AuNPs, a clear differentiation of concentrations can be observed.

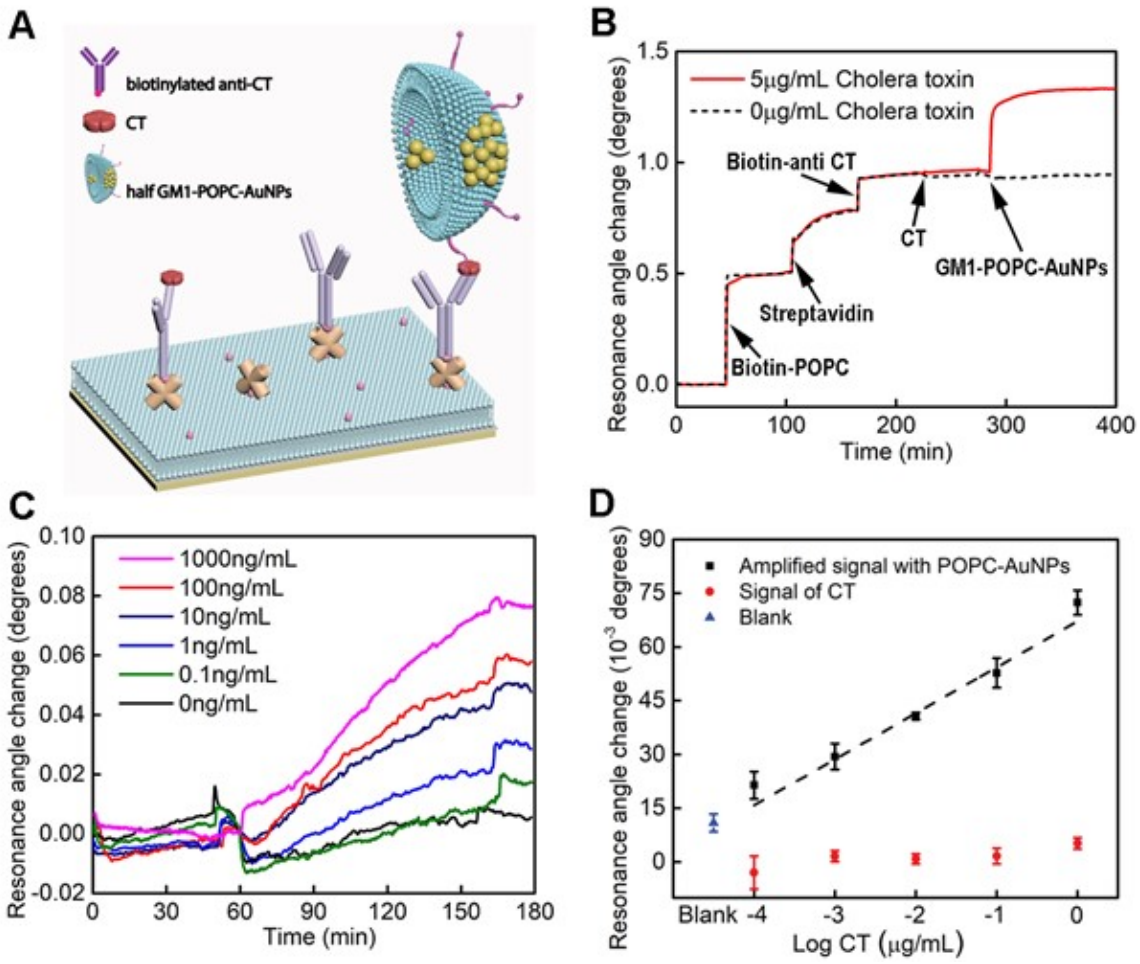

Figure 2.7: Detection of CT. (A) 3D scheme of surface chemistry on SPR for using GM1-POPC-AuNPs nanoclusters as a signal amplification tool to detect CT. (B) SPR sensorgram depicting using GM1-POPC-AuNPs for signal amplification to detect CT. (C) SPR sensorgram after injection of GM1-POPC-AuNPs to detect CT. (D) Calibration graph for detection of CT with and without amplification by GM1-POPC-AuNPs.

2.4.3 Long-term Stability of POPC-AuNPs Nanoclusters

We then tested the long−term storage stability of POPC−AuNP nanoclusters. The performance and stability of POPC−AuNPs was tracked by UV−vis, NTA and SPR biosensing over a 5−week period. There was no significant change in peak shape in UV−vis spectra after four weeks of storage, indicating little variation in the level of nanoparticle aggregation [55] (Figure 2.8A). The size distribution of POPC−AuNPs from NTA measurements remained unchanged for the first 2 weeks, but increased slightly after 4 weeks, from 124.3±1.1 nm to 128.1±3.2 nm (Figure 2.8B). The POPC−AuNPs still demonstrated consistent amplification performance, as observed from the SPR measurements over the period (Figure 2.8C). The high stability of POPC−AuNPs nanoclusters is possibly due to the large template size and high stability of the liposomes, as well as the repulsive interaction by thermal fluctuations [56] and head group electrostatic repulsion [57] between bilayers.

2.4.4 POPC-AgNPs and larger POPC-AuNPs nanoclusters for Signal Amplification on SPR

Silver nanoparticles (AgNPs) and magnetic nanoparticles have been broadly used for sensing and can generate enhancement due to stronger and sharper resonance [48] [58] [59]. In addition, there have been reports on using AuNPs with different sizes and shapes to optimize sensing performance [60] [61]. Therefore, investigation of coupling liposome with various types of nanoparticles was pursued. We synthesized larger biotin−POPC−25nm AuNPs and biotin−POPC−AgNPs nanoclusters and tested their performance in signal amplification. For POPC−AgNPs, the dried biotin−POPC lipid film was rehydrated

by EDTA−capped AgNPs solution, followed by sonication and extrusion process. Since EDTA−capped AgNPs can tolerate higher salt concentration than the citrate stabilized AuNPs, the NaCl concentration was increased to 0.6M to induce aggregation and assembly.

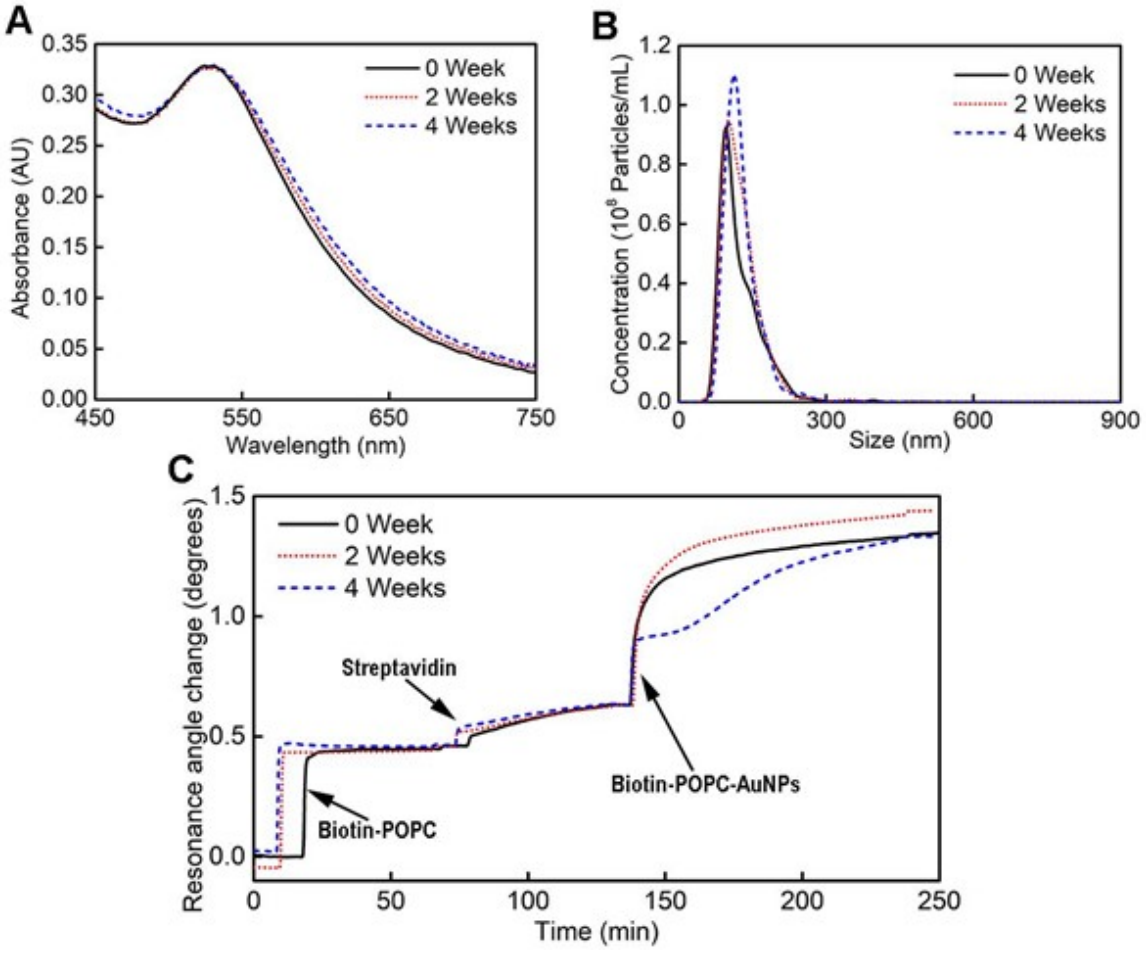

Figure 2.8: Long-term stability of POPC-13nm AuNPs. (A) Absorbance spectra of POPC-AuNPs 0 week, 2 weeks and 4 weeks after preparation. (B) Size distribution of POPC-AuNPs 0 week, 2 weeks and 4 weeks after preparation via NTA. (C) SPR sensorgram for biotinylated POPC-AuNPs binding to streptavidin on the bilayer interface 0 week, 2 weeks and 4 weeks after preparation.

From Figure 2.9, the number of AgNPs in liposome appears to be rather small, possibly due to the large size of the AgNPs ($\sim$ 30nm). NTA measurements show the average size of the POPC−AgNPs to be 130.4nm $\pm$ 39.7nm, slightly larger than the POPC−13nm AuNPs (Figure 2.9B). The somewhat broader absorbance peak than the original AgNPs, after coupling, is consistent with the formation of liposome−nanoparticles nanoclusters (Figure 2.9A). The signal amplification test by SPR with biotin−POPC−AgNPs shows an enhancement by 0.923 degrees, larger than the POPC−13nm AuNPs. Larger gold nanoparticle (25 nm) biotin−POPC−AuNPs nanoclusters were also tested for comparison, and a 0.652 degree increase in angular shift was observed (Figure 2.10), which is slightly smaller than POPC−13nm AuNPs (0.788 degrees). Overall, nanoparticle−encapsulated liposome nanoclusters provide robust signal enhancement as compared to nanoparticles or liposomes alone. They show a great potential to be a universal material to improve performance of sensing based on SPR detection scheme.

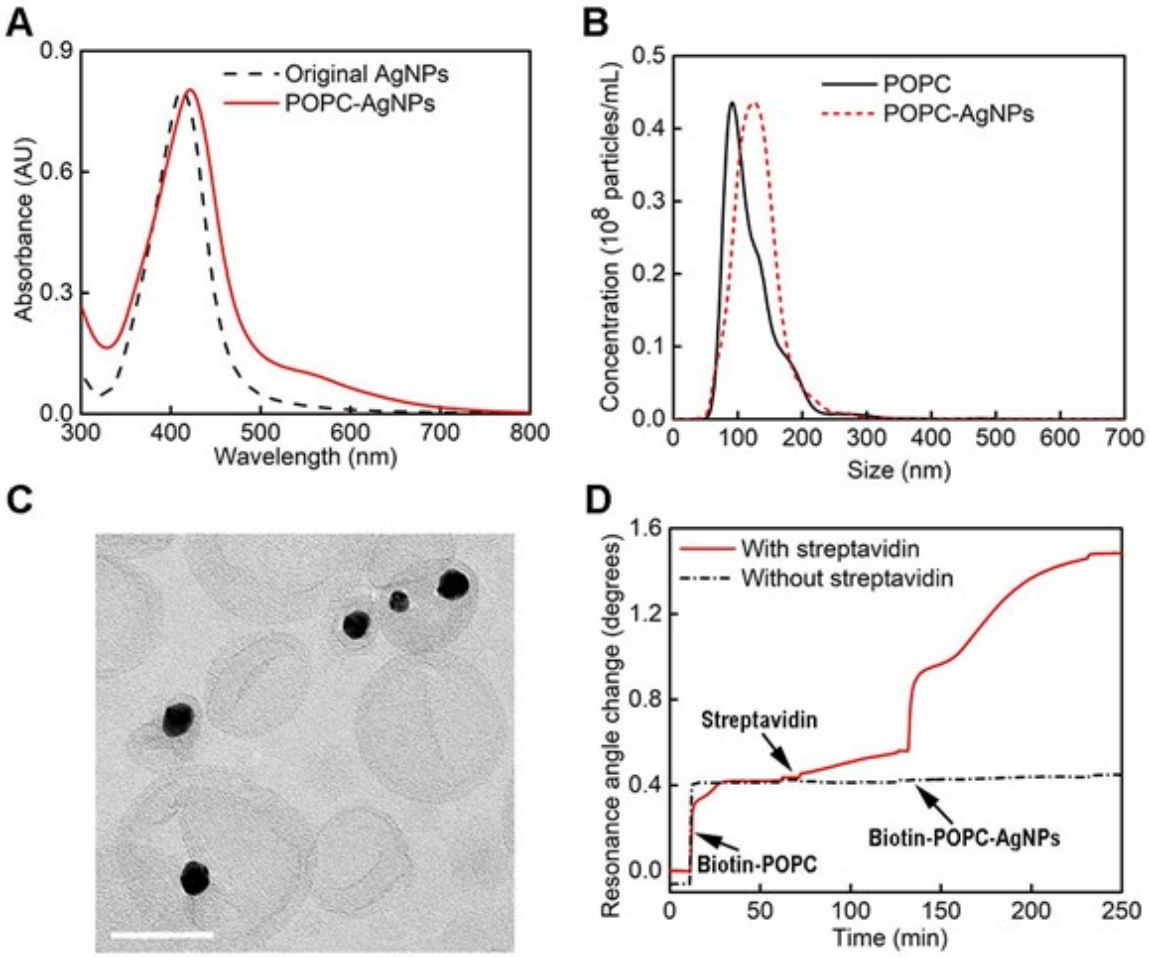

Figure 2.9: Preparation and signal amplification of POPC-AgNPs. (A) Absorbance spectra of POPC-AgNPs. (B) Size distribution of POPC-AgNPs via NTA. (C) TEM image of POPC-AgNPs. Bar=100nm. (D) SPR sensorgram for signal changes after injecting biotin-POPC-AgNPs on bilayer interface with and without streptavidin.

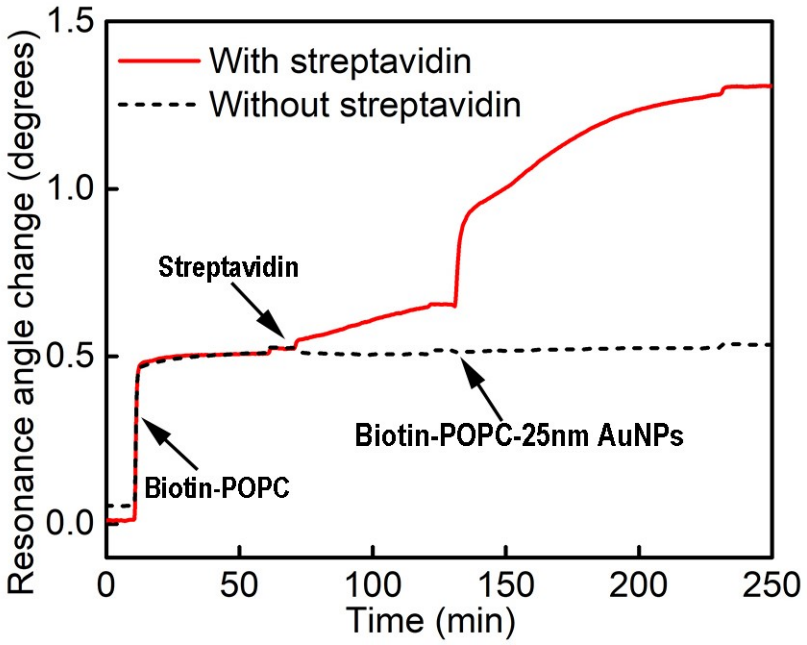

Figure 2.10: SPR sensorgram for signal changes after injecting biotin-POPC-25nm AuNPs on bilayer interface with and without streptavidin.

2.5 CONCLUSION

In this study, robust POPC−AuNPs nanoclusters were constructed by a salt−induced aggregation process. The POPC−AuNP assemblies were stable with a longer than 4 weeks shelf life, and the functional POPC−AuNPs proved to be effective as a signal amplification agent for SPR biosensing. The combination of large mass of the liposomes and the plasmonic coupling of the AuNPs yields marked signal amplification performance for SPR detection while the non−specific binding is kept low. Compared to DNA−AuNPs and POPC liposomes, POPC−AuNPs showed higher signal response, demonstrating a performance with more than 6 times greater than DNA−AuNPs and 1.5 times greater than POPC liposomes. The GM1 functionalized POPC−AuNPs were tested for detection of

cholera toxin, which resulted in almost 40 times amplification and a detection limit of 0.1ng/mL. Larger AuNPs and AgNPs were also coupled to biotin−POPC liposomes, which similarly yielded substantially amplified signals on SPR. POPC liposomes allow easy coupling of various nanoparticles, generating stable liposome−nanoparticles assemblies that act as effective signal amplification agents in biosensing. With further functionalization with specific receptors, the nanoclusters could be applied to detect a wide range of biomolecules with high detection sensitivity.

REFERENCES

[1] Gerrit Van Meer, Dennis R Voelker, and Gerald W Feigenson. Membrane lipids: where they are and how they behave. *Nature reviews Molecular cell biology*, 9(2):112–124, 2008.

[2] Anne L Plant. Supported hybrid bilayer membranes as rugged cell membrane mimics. *Langmuir*, 15(15):5128–5135, 1999.

[3] Yue-xiao Shen, Patrick O Saboe, Ian T Sines, Mustafa Erbakan, and Manish Kumar. Biomimetic membranes: A review. *Journal of Membrane Science*, 454:359–381, 2014.

[4] Ying Liu, Puhong Liao, Quan Cheng, and Richard J Hooley. Protein and small molecule recognition properties of deep cavitands in a supported lipid membrane determined by calcination-enhanced spr spectroscopy. *Journal of the American Chemical Society*, 132(30):10383–10390, 2010.

[5] Ying Liu, Michael C Young, Orly Moshe, Quan Cheng, and Richard J Hooley. A membrane-bound synthetic receptor that promotes growth of a polymeric coating at the bilayer–water interface. *Angewandte Chemie International Edition*, 51(31):7748–7751, 2012.

[6] K Scott Phillips, Thomas Wilkop, Jiing-Jong Wu, Rabih O Al-Kaysi, and Quan Cheng. Surface plasmon resonance imaging analysis of protein-receptor binding in supported membrane arrays on gold substrates with calcinated silicate films. *Journal of the American Chemical Society*, 128(30):9590–9591, 2006.

[7] Jonathan R Burns, Eugen Stulz, and Stefan Howorka. Self-assembled dna nanopores that span lipid bilayers. *Nano letters*, 13(6):2351–2356, 2013.

[8] Astrid Seifert, Kerstin Gopfrich, Jonathan R Burns, Niels Fertig, Ulrich F Keyser, and Stefan Howorka. Bilayer-spanning dna nanopores with voltage-switching between open and closed state. *ACS nano*, 9(2):1117–1126, 2015.

[9] Brynn R Olden, Caleb R Perez, Ashley L Wilson, Ian I Cardle, Yu-Shen Lin, Bryan Kaehr, Joshua A Gustafson, Michael C Jensen, and Suzie H Pun. Cell-templated silica microparticles with supported lipid bilayers as artificial antigen-presenting cells for t cell activation. *Advanced healthcare materials*, 8(2):1801188, 2019.

[10] Kabir H Biswas, Joshua A Jackman, Jae Hyeon Park, Jay T Groves, and Nam-Joon Cho. Interfacial forces dictate the pathway of phospholipid vesicle adsorption onto silicon dioxide surfaces. *Langmuir*, 34(4):1775–1782, 2018.

[11] Mathieu Jung, Nicolas Vogel, and Ingo Koper. Nanoscale patterning of solid-supported membranes by integrated diffusion barriers. *Langmuir*, 27(11):7008–7015, 2011.

[12] Samuel S Hinman, Charles J Ruiz, Georgia Drakakaki, Thomas E Wilkop, and Quan Cheng. On-demand formation of supported lipid membrane arrays by trehalose-assisted vesicle delivery for spr imaging. *ACS applied materials & interfaces*, 7(31):17122–17130, 2015.

[13] Ying Liu and Quan Cheng. Detection of membrane-binding proteins by surface plasmon resonance with an all-aqueous amplification scheme. *Analytical chemistry*, 84(7):3179–3186, 2012.

[14] K Scott Phillips and Quan Cheng. Microfluidic immunoassay for bacterial toxins with supported phospholipid bilayer membranes on poly (dimethylsiloxane). *Analytical chemistry*, 77(1):327–334, 2005.

[15] Ying Liu, Yi Dong, Jessica Jauw, Matthew J Linman, and Quan Cheng. Highly sensitive detection of protein toxins by surface plasmon resonance with biotinylation-based inline atom transfer radical polymerization amplification. *Analytical chemistry*, 82(9):3679–3685, 2010.

[16] Zhichao Lou, He Han, Ming Zhou, Jinfeng Wan, Qian Sun, Xiaoyan Zhou, and Ning Gu. Fabrication of magnetic conjugation clusters via intermolecular assembling for ultrasensitive surface plasmon resonance (spr) detection in a wide range of concentrations. *Analytical chemistry*, 89(24):13472–13479, 2017.

[17] Rongjuan Liu, Qing Wang, Qing Li, Xiaohai Yang, Kemin Wang, and Wenyan Nie. Surface plasmon resonance biosensor for sensitive detection of microrna and cancer cell using multiple signal amplification strategy. *Biosensors and Bioelectronics*, 87:433–438, 2017.

[18] Alexander Lambert, Zhanjun Yang, Wei Cheng, Zhenda Lu, Ying Liu, and Quan Cheng. Ultrasensitive detection of bacterial protein toxins on patterned microarray via surface plasmon resonance imaging with signal amplification by conjugate nanoparticle clusters. *ACS sensors*, 3(9):1639–1646, 2018.

[19] Prashant K Jain, Xiaohua Huang, Ivan H El-Sayed, and Mostafa A El-Sayed. Noble metals on the nanoscale: optical and photothermal properties and some applications in imaging, sensing, biology, and medicine. *Accounts of chemical research*, 41(12):1578–1586, 2008.

[20] Peter J Webster, Greg J Holland, Judith A Curry, and H-R Chang. Changes in tropical cyclone number, duration, and intensity in a warming environment. *Science*, 309(5742):1844–1846, 2005.

[21] Amanda J Haes and Richard P Van Duyne. A nanoscale optical biosensor: sensitivity and selectivity of an approach based on the localized surface plasmon resonance spectroscopy of triangular silver nanoparticles. *Journal of the American Chemical Society*, 124(35):10596–10604, 2002.

[22] Wing-Cheung Law, Ken-Tye Yong, Alexander Baev, and Paras N Prasad. Sensitivity improved surface plasmon resonance biosensor for cancer biomarker detection based on plasmonic enhancement. *ACS nano*, 5(6):4858–4864, 2011.

[23] Qiao Zhang, Jianping Ge, Tri Pham, James Goebl, Yongxing Hu, Zhenda Lu, and Yadong Yin. Reconstruction of silver nanoplates by uv irradiation: tailored optical properties and enhanced stability. *Angewandte Chemie*, 121(19):3568–3571, 2009.

[24] Hasan Aldewachi, Tamim Chalati, MN Woodroofe, Neil Bricklebank, B Sharrack, and Philip Gardiner. Gold nanoparticle-based colorimetric biosensors. *Nanoscale*, 10(1):18–33, 2018.

[25] Samuel S Hinman, Kristy S McKeating, and Quan Cheng. Dna linkers and diluents for ultrastable gold nanoparticle bioconjugates in multiplexed assay development. *Analytical chemistry*, 89(7):4272–4279, 2017.

[26] David A Giljohann, Dwight S Seferos, Weston L Daniel, Matthew D Massich, Pinal C Patel, and Chad A Mirkin. Gold nanoparticles for biology and medicine. *Angewandte Chemie International Edition*, 49(19):3280–3294, 2010.

[27] Vladimir P Torchilin. Recent advances with liposomes as pharmaceutical carriers. *Nature reviews Drug discovery*, 4(2):145–160, 2005.

[28] Federico Mazur, Marta Bally, Brigitte Städler, and Rona Chandrawati. Liposomes and lipid bilayers in biosensors. *Advances in colloid and interface science*, 249:88–99, 2017.

[29] Gyuho Yeom, Juyoung Kang, Hyungjun Jang, Ho Yeon Nam, Min-Gon Kim, and Chin-Ju Park. Development of dna aptamers against the nucleocapsid protein of severe fever with thrombocytopenia syndrome virus for diagnostic application: catalytic signal amplification using replication protein a-conjugated liposomes. *Analytical chemistry*, 91(21):13772–13779, 2019.

[30] Katie A Edwards and Antje J Baeumner. Enhancement of heterogeneous assays using fluorescent magnetic liposomes. *Analytical chemistry*, 86(13):6610–6616, 2014.

[31] Thijs Wink, Steven J van Zuilen, Auke Bult, and Wouter P Van Bennekom. Liposome-mediated enhancement of the sensitivity in immunoassays of proteins and peptides in surface plasmon resonance spectrometry. *Analytical Chemistry*, 70(5):827–832, 1998.

[32] Christoph Fenzl, Thomas Hirsch, and Antje J Baeumner. Liposomes with high refractive index encapsulants as tunable signal amplification tools in surface plasmon resonance spectroscopy. *Analytical chemistry*, 87(21):11157–11163, 2015.

[33] Aravind Kumar Rengan, Amirali B Bukhari, Arpan Pradhan, Renu Malhotra, Rinti Banerjee, Rohit Srivastava, and Abhijit De. In vivo analysis of biodegradable liposome gold nanoparticles as efficient agents for photothermal therapy of cancer. *Nano letters*, 15(2):842–848, 2015.

[34] Nishu Kanwa, Ananya Patnaik, Soumya Kanti De, Mirajuddin Ahamed, and Anjan Chakraborty. Effect of surface ligand and temperature on lipid vesicle–gold nanoparticle interaction: a spectroscopic investigation. *Langmuir*, 35(4):1008–1020, 2019.

[35] Xiuru Liu, Xiaoqiu Li, Wu Xu, Xiaohan Zhang, Zhicheng Huang, Feng Wang, and Juewen Liu. Sub-angstrom gold nanoparticle/liposome interfaces controlled by halides. *Langmuir*, 34(22):6628–6635, 2018.

[36] Kouta Sugikawa, Tatsuya Kadota, Kazuma Yasuhara, and Atsushi Ikeda. Anisotropic self-assembly of citrate-coated gold nanoparticles on fluidic liposomes. *Angewandte Chemie International Edition*, 55(12):4059–4063, 2016.

[37] Wolfgang Haiss, Nguyen TK Thanh, Jenny Aveyard, and David G Fernig. Determination of size and concentration of gold nanoparticles from uv- vis spectra. *Analytical chemistry*, 79(11):4215–4221, 2007.

[38] Gerrit Frens. Controlled nucleation for the regulation of the particle size in monodisperse gold suspensions. *Nature physical science*, 241(105):20–22, 1973.

[39] Jonathan Simpson, Derek Craig, Karen Faulds, and Duncan Graham. Mixed-monolayer glyconanoparticles for the detection of cholera toxin by surface enhanced raman spectroscopy. *Nanoscale horizons*, 1(1):60–63, 2016.

[40] Sarah J Hurst, Abigail KR Lytton-Jean, and Chad A Mirkin. Maximizing dna loading on a range of gold nanoparticle sizes. *Analytical chemistry*, 78(24):8313–8318, 2006.

[41] Samuel S Hinman, Charles J Ruiz, Yu Cao, Meghann C Ma, Jingjie Tang, Erik Laurini, Paola Posocco, Suzanne Giorgio, Sabrina Pricl, Ling Peng, et al. Mix and match: coassembly of amphiphilic dendrimers and phospholipids creates robust, modular, and controllable interfaces. *ACS applied materials & interfaces*, 9(1):1029–1035, 2017.

[42] Danke Xu and Quan Cheng. Surface-bound lipid vesicles encapsulating redox species for amperometric biosensing of pore-forming bacterial toxins. *Journal of the American Chemical Society*, 124(48):14314–14315, 2002.

[43] Stephanie Christau, Tim Moeller, Jan Genzer, Ralf Koehler, and Regine von Klitzing. Salt-induced aggregation of negatively charged gold nanoparticles confined in a polymer brush matrix. *Macromolecules*, 50(18):7333–7343, 2017.

[44] Alexandre Albanese and Warren CW Chan. Effect of gold nanoparticle aggregation on cell uptake and toxicity. *ACS nano*, 5(7):5478–5489, 2011.

[45] Juan C Fraire, Stephan Stremersch, Davinia Bouckaert, Tinne Monteyne, Thomas De Beer, Pieter Wuytens, Riet De Rycke, Andre G Skirtach, Koen Raemdonck, Stefaan De Smedt, et al. Improved label-free identification of individual exosome-like vesicles with au@ ag nanoparticles as sers substrate. *ACS applied materials & interfaces*, 11(43):39424–39435, 2019.

[46] Marek Sokolowski, Zehra Parlak, Christopher Bartsch, Stefan Zauscher, and Michael Gradzielski. Interaction between soft nanoparticles and phospholipid membranes: effect of the polymer-grafting density on nanoparticle adsorption. *ACS Applied Nano Materials*, 2(4):1808–1819, 2019.

[47] Nagarjun V Konduru, Flavia Damiani, Svetla Stoilova-McPhie, Jason S Tresback, Georgios Pyrgiotakis, Thomas C Donaghey, Philip Demokritou, Joseph D Brain, and Ramon M Molina. Nanoparticle wettability influences nanoparticle–phospholipid interactions. *Langmuir*, 34(22):6454–6461, 2018.

[48] Shuwen Zeng, Dominique Baillargeat, Ho-Pui Ho, and Ken-Tye Yong. Nanomaterials enhanced surface plasmon resonance for biological and chemical sensing applications. *Chemical Society Reviews*, 43(10):3426–3452, 2014.

[49] Jun Hyuk Heo, Kyung-Il Kim, Hui Hun Cho, Jin Woong Lee, Byoung Sang Lee, Seokyoung Yoon, Kyung Jin Park, Seungwoo Lee, Jaeyun Kim, Dongmok Whang, et al. Ultrastable-stealth large gold nanoparticles with dna directed biological functionality. *Langmuir*, 31(51):13773–13782, 2015.

[50] Stefano Mariani, Simona Scarano, Maria Laura Ermini, Massimo Bonini, and Maria Minunni. Investigating nanoparticle properties in plasmonic nanoarchitectures with dna by surface plasmon resonance imaging. *Chemical Communications*, 51(30):6587–6590, 2015.

[51] Xiaofeng Liu, Guofu Liao, Liyuan Zou, Yan Zheng, Xiaohai Yang, Qing Wang, Xiuhua Geng, Shaoyuan Li, Yaqin Liu, and Kemin Wang. Construction of bio/nanointerfaces: stable gold nanoparticle bioconjugates in complex systems. *ACS applied materials & interfaces*, 11(43):40817–40825, 2019.

[52] Lin He, Emily A Smith, Michael J Natan, and Christine D Keating. The distance-dependence of colloidal au-amplified surface plasmon resonance. *The Journal of Physical Chemistry B*, 108(30):10973–10980, 2004.

[53] Marco Frasconi, Cristina Tortolini, Francesco Botre, and Franco Mazzei. Multifunctional au nanoparticle dendrimer-based surface plasmon resonance biosensor and its application for improved insulin detection. *Analytical Chemistry*, 82(17):7335–7342, 2010.

[54] Jiří Homola. Surface plasmon resonance sensors for detection of chemical and biological species. *Chemical reviews*, 108(2):462–493, 2008.

[55] Vincenzo Amendola and Moreno Meneghetti. Size evaluation of gold nanoparticles by uv- vis spectroscopy. *The Journal of Physical Chemistry C*, 113(11):4277–4285, 2009.

[56] HeeTae Jung, B Coldren, JA Zasadzinski, DJ Iampietro, and EW Kaler. The origins of stability of spontaneous vesicles. *Proceedings of the national academy of sciences*, 98(4):1353–1357, 2001.

[57] AM Carmona-Ribeiro, LS Yoshida, and H Chaimovich. Salt effects on the stability of dioctadecyldimethylammonium chloride and sodium dihexadecyl phosphate vesicles. *The Journal of Physical Chemistry*, 89(13):2928–2933, 1985.

[58] Chuanbo Gao, Zhenda Lu, Ying Liu, Qiao Zhang, Miaofang Chi, Quan Cheng, and Yadong Yin. Highly stable silver nanoplates for surface plasmon resonance biosensing. *Angewandte Chemie International Edition*, 51(23):5629–5633, 2012.

[59] Jianlong Wang, Ahsan Munir, Zanzan Zhu, and H Susan Zhou. Magnetic nanoparticle enhanced surface plasmon resonance sensing and its application for the ultrasensitive

detection of magnetic nanoparticle-enriched small molecules. *Analytical chemistry*, 82(16):6782–6789, 2010.

[60] Shuwen Zeng, Xia Yu, Wing-Cheung Law, Yating Zhang, Rui Hu, Xuan-Quyen Dinh, Ho-Pui Ho, and Ken-Tye Yong. Size dependence of au np-enhanced surface plasmon resonance based on differential phase measurement. *Sensors and Actuators B: Chemical*, 176:1128–1133, 2013.

[61] Suhee Kim and Hye Jin Lee. Gold nanostar enhanced surface plasmon resonance detection of an antibiotic at attomolar concentrations via an aptamer-antibody sandwich assay. *Analytical chemistry*, 89(12):6624–6630, 2017.

Chapter 3

3D Printed Prisms with Micropatterns for Multiplex Label-Free Biosensing

3.1 ABSTRACT

3D printed optics have attracted attention due to ease of design and fabrication and low cost. Our group has previously reported the application of 3D printed equilateral prisms using a commercial clear resin for surface plasmon resonance imaging (SPRi) biosensing. However, the resonance incident angle using the prisms is relatively high, resulting in a small sensing area. Additionally, the 3D printed equilateral prisms were not applicable for multiplex biosensing. Here, we present the design and fabrication of a 3D printed Dove prism with transverse patterns and the capacity for multiplex SPRi biosensing. Following

the benchtop polishing process, the surface roughness of the sensing area was found to be as low as 10 nm, which resulted in brilliant optical performance. In reflectivity images at the sensing incident angle, the rectangular micropatterns were easily differentiated from the background, and the cross sections of the S-shaped flow channel and micropatterns were used as the sensing area for SPRi. Compared to the 3D printed equilateral prisms, the Dove prisms showed an 8-degree reduction in sensing angle and led to more reliable results. The prisms were utilized for protein recognition, including analysis of streptavidin and cholera toxin, and demonstrated comparable sensitivity to platforms using commercial glass prisms. Moreover, we demonstrated another approach to fabrication of microarrays on a prism surface using a 3D printed E-beam mask. This work opens new avenues for utilization of 3D printing in multiplex optical biosensing in a cost-efficient, photolithography-free, and convenient manner, without losing sensitivity compared to conventional the SPRi setup with a commercial glass prism.

3.2 INTRODUCTION

Additive manufacturing, known as 3D printing, is an adaptable technique for the construction of 3D architectures with complex geometric shapes from a well-designed 3D model using a fast and straightforward approach [1] [2]. This technique relies on a layer-upon-layer stacking method, which is in contrast to the traditional subtraction techniques of material-removal processes [3], and is continuously attracting public and media attention due to its unique advantages, such as user friendly, rapid prototyping and relatively low cost [4] [5]. As 3D printing techniques allow complicated fabrication without tedious and

expensive manufacturing processes, they are applied in many fields, including machinery, aerospace and aviation, biomaterials, biosensors and biomedical devices, and robotics; scientists and engineers in these fields use the optical, chemical, fluidic, electromagnetic and thermal features of 3D printing to their advantage [6] [7] [8]. Specifically, 3D printing shows great potential in analytical chemistry and has played an increasingly important role over time. It contributes not only to the acceleration of manufacturing processes for multiple analytical devices and systems, but also to the development of new analytical techniques with improved performance [9]. Thus far, in analytical labs, 3D printing has been applied to fabricate supporting analytical tools [10], integrated analytical systems [11], point-of-care devices [12], and functional materials for biosensing [13], with more freedom for design and improvement of functionality [9]. Fabrication of optical components for analytical assays are an important application of 3D printing techniques [5], example of which include 3D printed lenses and prisms [14], waveguides [15], and terahertz optics [16].

To date, multiple techniques for 3D printing have been applied in fabrication of 3D components, such as powder bed fusion, material jetting, sheet lamination, material extrusion, binder jetting, directed energy deposition, and photopolymerization [6]. Among these techniques, stereolithography (SLA) was established based on an ultraviolet (UV) radiation-triggered, localized photopolymerization approach, which occurred in a bath containing a mixture of monomers, oligomers and photo initiators. SLA generated significant interest via its broad applicability in complex 3D structure manufacturing, high degree of precision, and capacity for use of a wide variety of resin materials [17]. Moreover, SLA was demonstrated as a powerful tool for fabricating 3D printed optics [18] [19]. SLA has, there-

fore, become a foundational type of modern 3D printing [5], and there are broad prospects for applications of SLA-based 3D printed optics.

Surface plasma resonance (SPR) biosensing is a widely used label-free technique for monitoring biomolecular interaction and achieving protein quantification, which relies on optical excitation of surface plasma waves [20]. The generation of surface plasma waves generally requires prism couplers in order to increase the incident light wave vector to match the wave vector of the surface plasmons [21]. The geometry and material of the SPR prism couplers have significant impact on SPR sensing performance [20] [22]. Therefore, there has been investigation of high-resolution SPR systems coupled with various types of prisms, including Dove prisms [23], hollow prisms [24], and photopolymer hemispherical optical prisms [25]. Taking advantage of ease of design and fabrication, rapid prototyping, and low cost, researchers have used 3D printing to fabricate high-performance prisms for SPR devices. Lertvachirapaiboon and coworkers reported development of a dual-mode SPR sensor chip platform using a grating 3D printed prism, which had outstanding refractive index sensitivities and achieved fine-tuning of the excitation wavelength for SPR biosensing [26]. Previously, by taking commercial equilateral SF2 glass prisms for SPR as a reference, our group fabricated 3D printed equilateral prisms and applied them to surface plasmon resonance imaging (SPRi) biosensing [19]. However, the 3D printed equilateral prisms suffered drawbacks, such as high resonance angle (the reflectivity dip is at approximately 82°) and small sensing area, which negatively impacts sensing performance due to the relatively low refractive index of the print-out material (approximately 1.49). To solve this problem, we designed and fabricated a 3D printed Dove prism with microscale line patterns for multiplex

SPRi biosensing without using photolithography, and achieved dramatic reduction of the incident resonance angle without changing the 3D printing materials. At the same time, the SPRi sensing resolution was significantly improved due to a larger sensing area. The sensing performance of the SPRi setup was tested via salt assays and protein biosensing, which showed sensitivity comparable to commercial prism coupled to SPRi platforms. Furthermore, a 3D printed E-beam evaporation mask for gold micro array fabrication with a larger number of gold islands was also investigated as an alternative method of multiplex SPRi biosensing.

3.3 EXPERIMENTAL

3.3.1 Materials

Methoxypolyethylene glycol amine (methyl-PEG-amine), 11-mercaptoundecanoic acid (MUA), N-Hydroxysuccinimide (NHS), 1-(3-dimethylaminopropyl)-3-ethylcarbodiimide hydrochloride (EDC), cholera toxin (CT) from Vibrio cholerae and anti-CT antibody produced in rabbit were purchased from Sigma Aldrich (St. Louis, MO). Sodium chloride and streptavidin were purchased from Thermo Scientific (Rockford, IL). m-PEG-SH (MW 1000) and biotin-PEG-SH (MW 2000) were obtained from Nanocs Inc. (New York, NY). Clear V4 photoactive resin (FLGPCL04) was obtained from Formlabs, Inc. (Somerville, MA). SF2 (n=1.648) glass equilateral prisms were obtained from Surplus Shed (Fleetwood, PA). A solution of 1× PBS containing 10 mM Na2HPO4, 137 mM NaCl, 1.8 mM KH2PO4, 2.7 mM KCl (pH=7.45) was prepared. Chromium and gold pellets for electro-beam evaporation were obtained from Kurt J. Lesker (Jefferson Hills, PA).

3.3.2 Instrumentation

A homebuilt SPRi setup was used for spectroscopy and imaging assays at room temperature. Briefly, for real-time SPRi measurements, the prisms were fixed in a 3D printed prism holder designed to fit the specific prism, the incident light angle was set to the direction of 30 %R on the left-hand side of the dip of SPR reflectivity curve, where the slope is the steepest. For the salt sensing assay using the commercial SF2 glass prism, a gold deposited (2 nm chromium and 50 nm gold) glass slide was coupled with the prism for SPRi measurement. The running buffer for the salt sensing assay is nanopure water, and 1× PBS for the streptavidin and CT assays (flow rate: 5 mL/h). Atomic force microscopy (AFM) characterization was performed on a Veeco Dimension 5000 (Santa Barbara, CA) under tapping mode. Ellipsometry was conducted using a UVISEL M200 (Horiba Jobin Yvon, France). For both AFM and ellipsometry characterization, a 3D printed cuboid (20 mm × 20 mm × 1 mm) was treated with the same sanding and polishing procedure to mimic the surface condition of the 3D printed Dove prism, and then used as the specimen because of the sample height restriction of the instruments.

3.3.3 Design of the Dove Prisms/E-beam Evaporator Masks by Stereolithography/3D printing

The 3D models of the prisms were designed using SketchUp software (Trimble, Inc., Sunnyvale, CA) [19]. Formlabs software was used to upload the 3D models to a commercial 3D stereolithography printer, Formlabs Form 3 (Somerville, MA), for rapid prototyping. More specifically, a compact system of lenses and mirrors were integrated

in the light processing unit (LPU) within the printer and a 250 mW UV laser was used to produce accurate prints (XY resolution: 25 µm). The cured prisms were placed in an isopropanol bath for 20 min then washed with isopropanol three times before drying via compressed air. A CL-1000 UV crosslinker (UVP Inc., Upland, CA) was applied to post-cure the prisms for 1.5 h. The prisms were then treated with several rounds of wet sanding and buffer wheel/polishing (Central Machinery, USA) to pursue optical use. Similarly, 3D printed E-beam evaporation masks were fabricated using Formlabs Form 3 and Clear V4 photoactive resin, followed by the same cleaning procedure as was used to produce the 3D printed Dove prisms.

3.3.4 Gold Nanofilm Deposition

The commercial SF2 Prisms, polished 3D printed equilateral prisms, and polished 3D printed Dove prisms were first washed with isopropanol and dried three times under compressed air. A standard cleanroom protocol for gold deposition via an electron-beam (E-beam) evaporator (Temescal, Berkeley, CA), previously reported by our group [27], was applied to generate a 2 nm-thick chromium film and a 50 nm-thick gold film on the sensing surface of the prism at 5×10^{-6} Torr. The prisms were stored in a desiccator at room temperature before use.

3.3.5 SPR Imaging for Protein Biosensing

Streptavidin biosensing was conducted by injection of 1 mg/mL biotin-PEG-SH aqueous solution for attachment to the gold surface. The surface was further blocked by m-PEG-SH to minimize non-specific binding of streptavidin. A streptavidin PBS solution at

various concentrations was then injected into the system and the % R change was measured.

For CT biosensing, the surface chemistry was first characterized using a dual channel NanoSPR (NanoSPR, Addison,IL) with a red laser light ($\lambda = 670$ nm). For SPRi assays, the 3D printed Dove prism was immersed in 1 mM MUA ethanol solution overnight to form a self-assembled monolayer (SAM) for the attachment of carboxyl groups to the gold surface [28] of the prism. Then, the freshly made EDC (200 mM)/NHS (50 mM) solution was spotted on the prism gold surface which then covered the surface. CT solutions at different concentrations (in 1× PBS) were spotted and incubated at the selected sections of the 3D printed Dove prism surface, which was placed in a wet chamber for 1 h (Figure 3.4c); the other sections were used as control sections for SPRi biosensing. The whole gold surface of the printed prism was treated with a mixed solution of m-PEG-amine and bovine serum albumin (BSA) to passivate the unbonded carboxyl groups on the surface. A PDMS flow cell was then clamped on the prism. Next, 200 µg/mL anti-CT in PBS solution was injected into the SPRi system and the % R value change was measured.

3.4 RESULTS AND DISCUSSION

3.4.1 The 3D Printed Dove Prism for Surface Plasmon Resonance Imaging: Theory and Design

SPR, as a quantum electromagnetic phenomenon, happens when light interacts with free electrons at a metal-dielectric interface and causes localized charge density oscillations that propagate along the boundary of the interface [29]. The surface plasma wave (SPW) is a transverse magnetic (TM)-polarized wave, which means that the magnetic vec-

tor is perpendicular to the propagation direction of the SPW and parallel to the plane of interface at the same time [20]. The excitation of surface plasmon polaritons (SPP) is associated with both energy (angular frequency ω) and momentum (the wavevector k_x). For a given energy $\hbar\omega$, the wavevector of light k_x is always larger than that in free space, which indicates that none of the light with any frequency in free space can excite the SPP on a plane interface [22]. Therefore, the wavevector of the incident optical wave needs to be enhanced for the occurrence of SPW, which is commonly achieved by prism couplers in attenuated total reflection (ATR) mode [30]. The relationship between the propagation constant of a SPW at the metal and dielectric interface k_{SPW} and free space wavenumber k_0 is demonstrated by the following equation [20]:

$$k_{SPW} = k_0 \sqrt{\frac{\varepsilon_m {n_a}^2}{\varepsilon_m + {n_a}^2}} \tag{3.1}$$

where ε_m denotes the dielectric constant of the metal, and n_a denotes the refractive index of the dielectric. In order to activate the SPR by photons, the wavevector of the photon k_{photon} needs to match with the wavevector of the SPW, which can be achieved by changing the incidence angle of the incoming light. The relationship between k_{photon}, k_{SPW}, and angle of incident light under the condition at which plasmon resonance occurs is expressed in the following equation [31]:

$$k_{photon} = k_{SPW} = n_{prism} k_0 sin\theta_{res} \tag{3.2}$$

where n_{prism} denotes the refractive index of the prism and θ_{res} denotes the incident angle of the light. Thus, according to Equation 3.2), for prisms with the same materials, the incident light (at a specific wavelength) resonance angle within the prism remains the same.

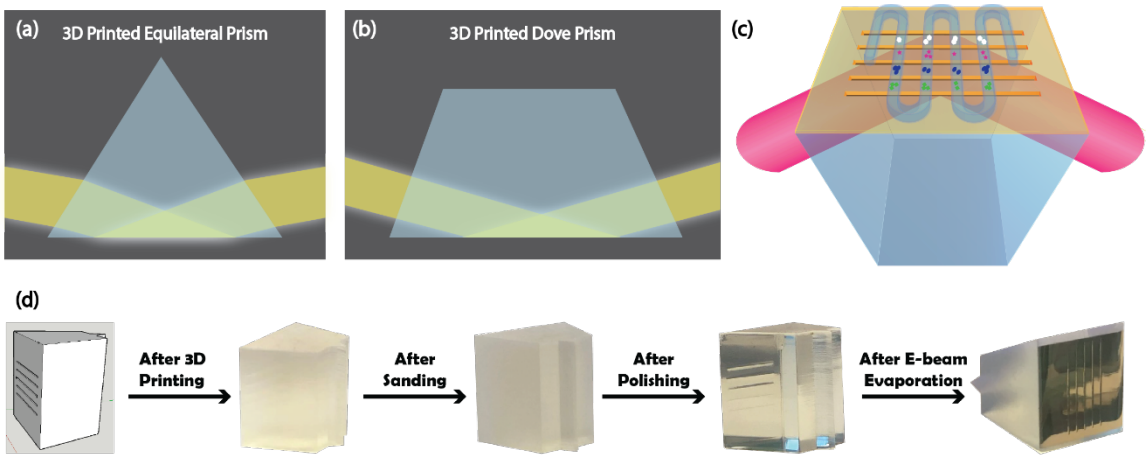

Figure 3.1: Design and fabrication of 3D printed Dove prisms. Schemes of light reflection when go through (a) a 3D printed equilateral prism and (b) a 3D printed Dove prism. (c) Scheme of SPRi sensing platform using a 3D printed Dove prism. (d) Fabrication scheme for 3D printed Dove prisms.

Based on the consideration above, we calculated the incident light resonance angle inside the previously reported 3D printed equilateral prism, which is about 74°, and applied this angle as the base angle for the Dove prism design. Figure 3.1a and 3.1b illustrate the light path of the refracted laser beam passing through the 3D printed equilateral and Dove prisms and reflected on the gold-dielectric interface. In this situation, the incident light will be perpendicular to the Dove prism surface at the resonance angle and achieve a much lower sensing angle and larger sensing area compared with the 3D printed equilateral prism. The face with gold deposition of this 3D printed Dove prism was designed to be the same size as the previous 3D printed equilateral prism, which is 2.4 cm × 2.4 cm. A total of 5 regularly spaced cuboid-shaped grooves (1.84cm in length, 350 µm in height, 310 µm in depth, and 1.9 mm apart from each other) were designed on the sensing face for the purpose of multiplex sensing (Figure 3.1c). After deposition of a thin gold layer on the sensing face, the area between the grooves were modified with different capturing ligands for SPRi biosensing of various targets simultaneously. When packed with an S-shaped flow cell on the top of the prism, the cross sections of the rectangular patterns and the S-shaped flow channel became the sensing area of the SPRi sensor. Since multiplex SPRi biosensing has traditionally relied on combining a chip with micro patterns by photolithography fabrication [32] [33], the fabrication cost and time were substantially reduced by use of 3D printed Dove prisms.

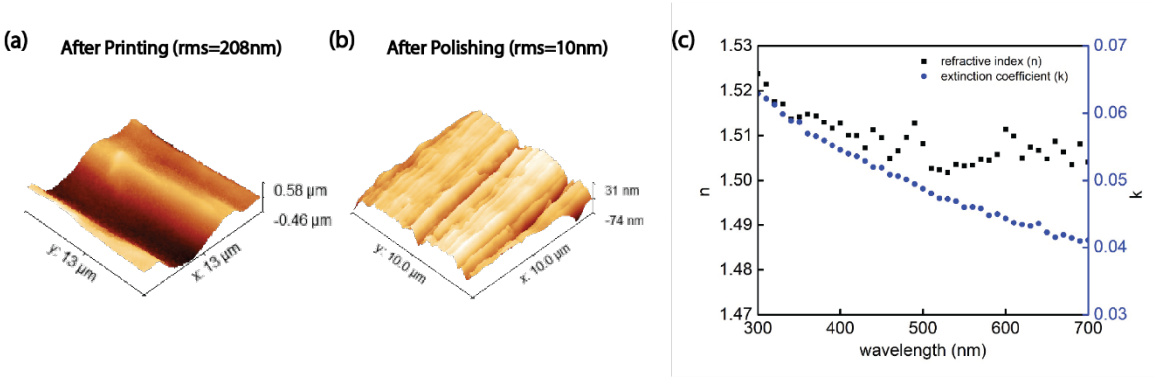

Figure 3.2: Characterization of 3D printed Dove prisms. Atomic force microscopic images showing the surface roughness of 3D printed Dove prisms (a) before (rms=208nm) and (b) after (rms=10nm) the polishing procedure. (c) Ellipsometry results of the 3D printed Dove prisms, depicting refractive index (n) and extinction coefficient (k) change with wavelength for the printed resin.

3.4.2 Fabrication and Characterization of 3D Printed Dove Prisms

The steps of 3D printed Dove prism fabrication are demonstrated in Figure 3.1d. We designed a triangular-shaped hump at the back side of the printed Dove prism to fix it with a 3D printed prism holder on a homebuilt SPRi setup. Since the limited resolution of the 3D printer could not reach the requirements for optical use, a standard benchtop polish-

ing procedure (including wet sanding and buffer wheel/polishing compound treatment) was applied to minimize the surface roughness of the prism [19]. The prisms showed clearness and increased transparency after the polishing. Moreover, during the sanding via sanding paper and the wheel polishing processes, the area of the narrow cuboid-shaped grooves could not be well-sanded or polished, which created a significant difference in SPRi under the CCD camera compared with the well-polished sensing area after gold deposition.

The surface topography of the 3D printed Dove prisms before and after polishing was characterized by atomic force microscopy (AFM; Figure 3.2a, 3.2b). As a result, the prism surface roughness dropped from 208 nm (characterized area: 13 µm × 13 µm) after print-out to 10 nm (characterized area: 10 µm × 10 µm) after sanding and polishing. Although the surface roughness of the 3D printed prisms is not comparable with that of the commercial glass prisms, which are usually less than 2 nm [34], the 3D printed Dove prisms show relatively smooth surfaces that are suitable for optical applications.

The refractive index (n) and extinction coefficient (k) of the print-out material for the Dove prism were characterized by ellipsometry under lights of different wavelength. Specifically, under 650 nm wavelength, which is the common operating laser wavelength for SPR, the refractive index of the 3D printed Dove prism was 1.5048, which is very close to that of PMMA (1.4864), as reported in the literature [35], and is also close to the refractive index (1.475) we reported previously using another batch of clear resin from the same company [19]. These results demonstrate that the materials of the printed prism shared similar optical properties with PMMA.

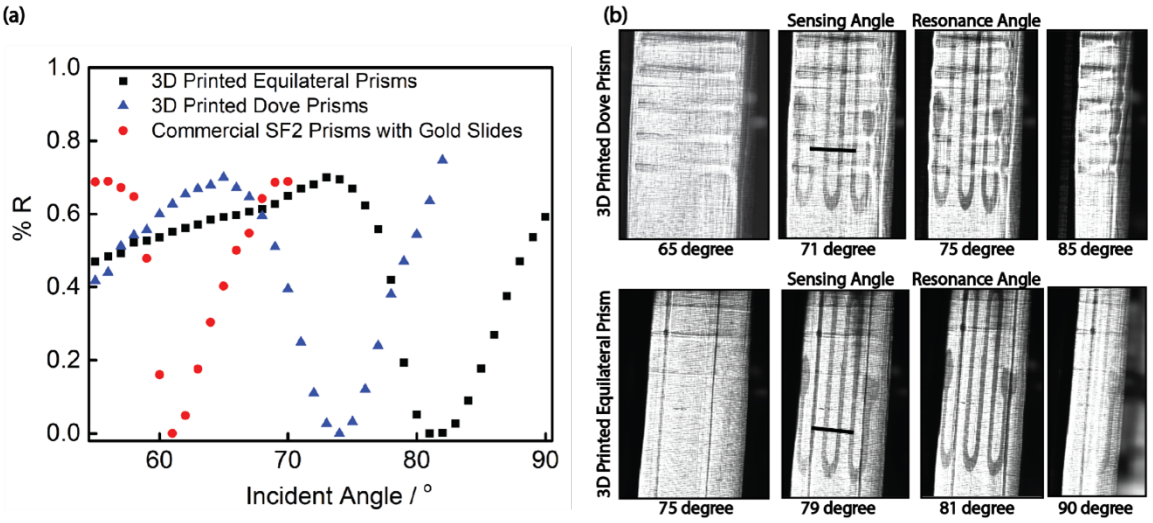

Figure 3.3: 3D printed Dove prisms on SPRi. (a) Surface plasmon resonance reflectivity curves with 3D printed equilateral prisms, 3D printed Dove prisms and commercial SF2 glass prisms with gold islands slides on SPRi. (b) Reflected images showing plasmonic resonance for the gold film coated 3D printed equilateral prism (top) and 3D printed Dove prism (bottom) surface with different incident light angle. Bars in the images of sensing angle were used to evaluate sensing area difference between the 3D printed equilateral prisms and 3D printed Dove prisms.

3.4.3 3D Printed Dove Prism for SPR Imaging Setup

Unlike SPR spectroscopy, which relies on monitoring angle change or wavelength change, SPRi measures reflective light intensity at a fixed angle [36], which is generally located in the linear response region of the left of the dip in the reflectivity curve [37]. The

dip in the reflectivity curve occurs when optical parameters match the resonance condition, causing the generation of SPP on the gold-dielectric interface. In general, we assumed 0 for the reflectivity at the resonance angle and 70% reflectivity for the maximum value in the reflectivity curve. Furthermore, the incident light angle at which reflectivity is 30% on the left of the resonance point was chosen as the sensing angle for SPRi assays.

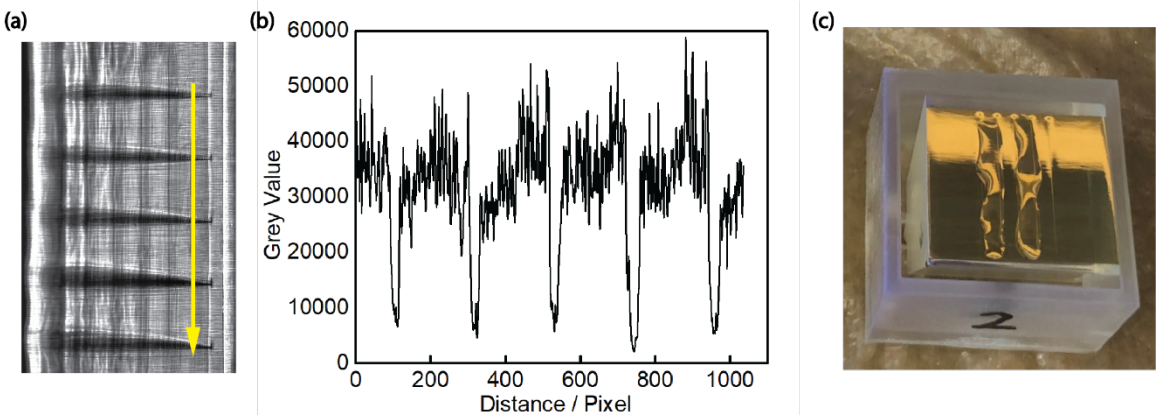

Figure 3.4: (a) Reflected image of a 3D printed Dove prism on the sensing angle. Grey values along the arrow, which is perpendicular to the dip lines pattern on the prism surface, is shown in (b). (c) Images of incubating the prism surface with different solutions for multiplex detection purpose.

In this work, a commercial SF2 prism with a gold-glass slide and 3D printed prisms were applied to construct a homebuilt SPRi setup in the Kretschmann configuration; SPR reflectivity curves were then obtained. Compared with the 3D printed equilateral prisms with the sensing angle at 79° and resonance angle at 81°, the 3D printed Dove prism showed much smaller resonance (75°) and sensing (71°) angles, indicating that Dove prism design could significantly lower the resonance incident light angle without changing the prism materials. As a reference, the resonance angle for an SF2 glass prism with a gold-glass slide is 61° (Figure 3.3a). In addition, reflectivity images (at the angle before the resonance angle where the S channel is invisible, the sensing angle, the resonance angle, and the angle after the resonance angle where S channel is invisible) of 3D printed equilateral prisms and 3D printed Dove prisms were captured using a CCD camera and compared (Figure 3.3b). Black bars in the figures illustrate the same size of sensing area on the real prisms by the SPRi setup coupled with 3D printed Dove prisms and 3D printed equilateral prisms, respectively. As indicated by counting the pixels along the length of the specified sensing area, the SPRi platform combined with 3D printed Dove prisms had a 21% larger sensing area than the SPRi platform with 3D printed equilateral prisms, resulting in more reliable biosensing results. Moreover, Figure 3.4a shows the reflected image at the sensing angle, where both the S-shaped channel and the groove patterns are clearly defined. Image J was used to evaluate the gray value along the yellow arrow in Figure 3.4a, and a periodic change in gray value was observed, illustrating the ease of differentiation of different sensing sections on the 3D printed Dove prisms for multiplex assays (Figure 3.4b).

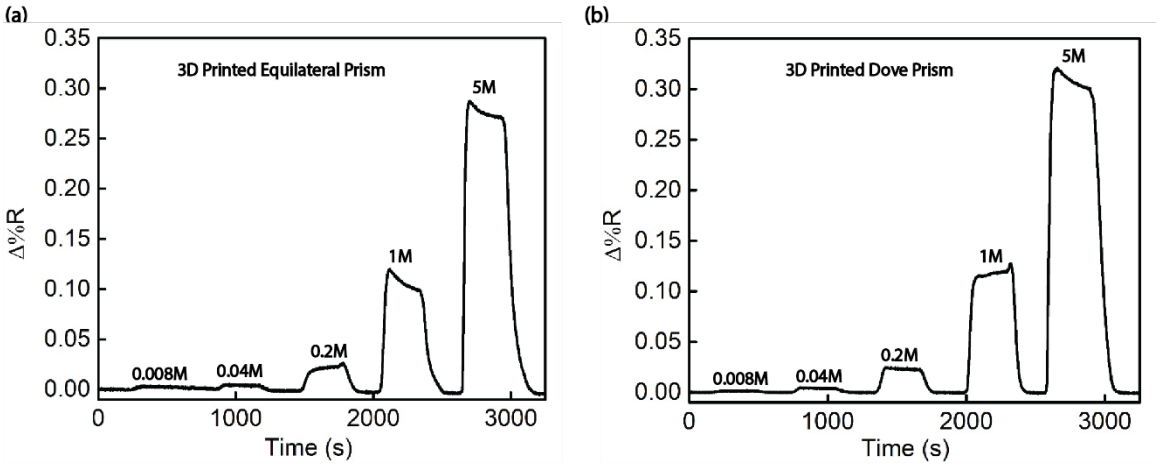

Figure 3.5: Real-time sensorgrams for (a) 3D printed equilateral prisms and (b) 3D printed Dove prisms coupled SPRi for NaCl injections with different concentrations followed by rinsed with nanopure water.

3.4.4 Biosensing by the 3D Printed Dove Prism Coupled SPR Imaging System

The refractive index sensitivity of 3D printed Dove prism coupled SPRi was evaluated by injection of sodium chloride solution and then compared with results using 3D printed equilateral prisms. The concentration of NaCl in the aqueous solution is positively correlated with the refractive index of the solution, and thus used for monitoring the SPRi

response to medium with different refractive indexes within the flow cell. In this experiment, a series of concentrations of NaCl solution, ranging from 0.008 M to 5 M, were injected into the flow channel and the corresponding SPRi signal was monitored in real time (Figure 3.5). SPRi imaging demonstrated a greater response when coupled with the 3D printed Dove prism than when coupled with the 3D printed equilateral prism after injection of NaCl solution of the same concentration, indicating that the physical structure of the prism has a significant impact on the performance of an SPR sensor. This is likely due to the incident light being perpendicular to the Dove prism surface at the resonance angle. Based on Snell's law [38], refractive angle changes faster with incident angle of the light when the incident angle is close to 0 (perpendicular to the prism face), causing a steeper slope around the sensing angle in the reflectivity curve of SPRi and further increasing SPRi sensitivity. Mukhtar et al. also reported that the selectivity and sensitivity of SPR are greatly enhanced when employing hemispherical or half cylindrical type-BK7 prisms compared with conical and triangular type-BK7 prisms [22], which also supports our hypothesis.

The sensitivity of the SPRi setup with the 3D printed Dove prism was also evaluated through protein biosensing. Streptavidin SPRi biosensing is performed by injection of biotin-PEG-thiol on the gold surface for streptavidin binding, followed by injection of block polymers (methyl-PEG-thiol) to minimize non-specific binding and associated signal, and then a final injection of streptavidin in PBS solution to generate the streptavidin signal (Figure 3.6a).

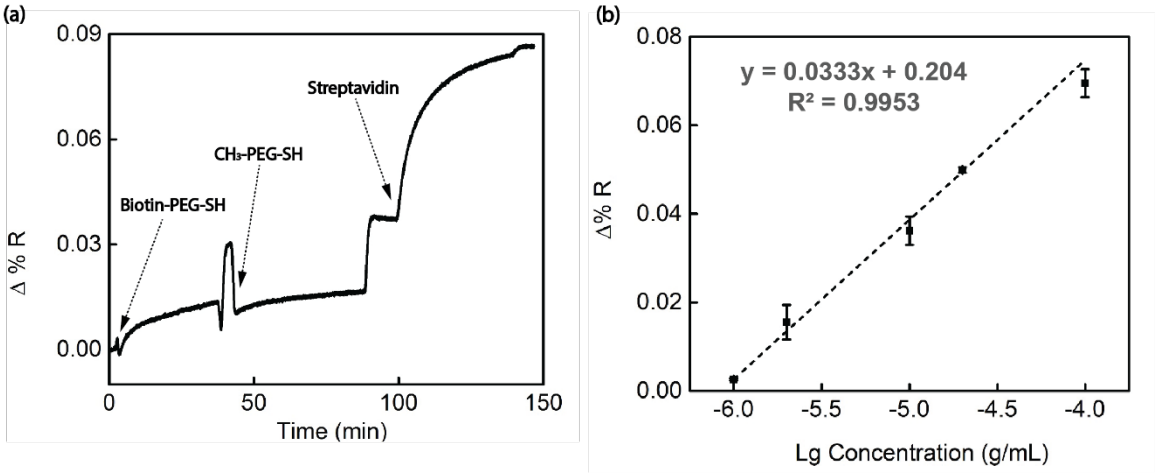

Figure 3.6: Biosensing of streptavidin using 3D printed Dove prisms coupled SPRi. (a) SPR sensorgram of streptavidin binding. (b) Calibration curve of detection of streptavidin on SPRi using the 3D printed Dove prisms.

The drastic drop of the reflection intensity when introducing methyl-PEG-thiol is due to the bulk refractive index change of the solution, which also shows a significant increase in signal as soon as the surface is rinsed with running buffer. A calibration curve for streptavidin biosensing at concentrations ranging from 1 µg/mL to 100 µg/mL via the 3D printed Dove prism SPRi platform was generated, showing a detection limit of 1 µg/mL (Figure 3.6b).

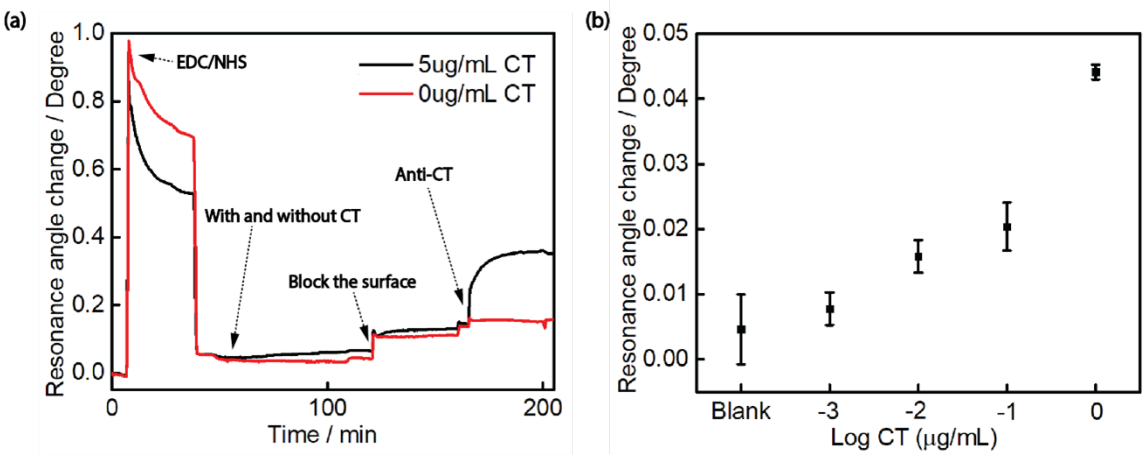

Figure 3.7: Biosensing of cholera toxin using 3D printed Dove prisms on SPRi. (a) SPR sensergram of CT binding to the self-assembled monolayer via EDC/NHS, and Anti-CT recognition. (b) Calibration graph for detection of CT using 3D printed Dove prisms on SPRi.

Furthermore, this 3D printed Dove prism coupled SPRi was applied to a biosensing platform for bacterial CT (Figure 3.7a). Briefly, a MUA self-assembled monolayer (SAM) was formed on the prism gold surface and the carboxyl functional groups were activated by EDC (200 mM)/NHS (50 mM) solution and attached to CT (at different concentrations) via covalent amide linkages. After passivation of free carboxyl groups on the surface by a mixture of methyl-PEG-amine and BSA, an anti-CT solution was injected for CT recognition. Compared with the assay in which no CT was bound to the surface, which shows relatively

low non-specific binding, the introduction of anti-CT generated a marked increase in SPRi signal. According to the calibration graph for CT detection (Figure 3.7b), the platform has the capability to detect CT at a concentration as low as 1 ng/mL, which is comparable to the sensitivity of a commercial SPR platform [39]. These biosensing results demonstrate that the 3D printed Dove prism coupled SPRi achieves remarkable sensing performance for various protein targets and provides reliable signals.

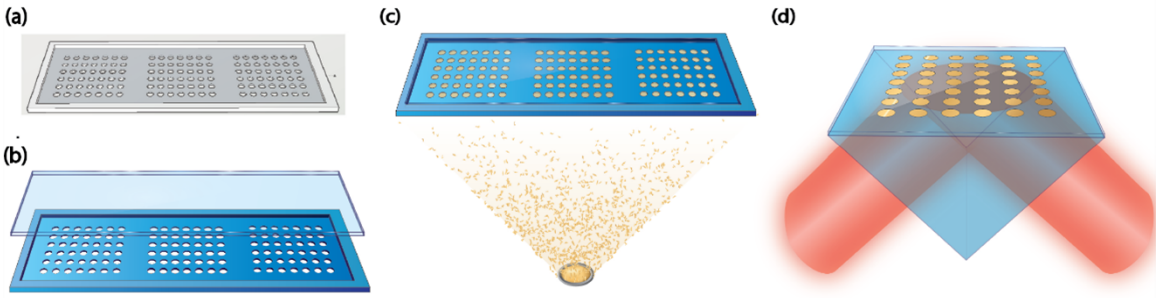

Figure 3.8: Design and fabrication of a 3D printed E-beam evaporation mask for gold islands arrays on SPRi glass slides chips for multiplex sensing. (a) A 3D model of the 3D printed E-beam evaporation mask. (b) A microscope glass slide can be fixed in the E-beam mask for (c) E-beam evaporation. (d) The glass slide with gold arrays were coupled with a commercial glass prism for SPRi sensing.

3.4.5 Application of a 3D Printed E-beam Evaporation Mask for Multiplex SPRi Biosensing

Traditionally, the plasmonic arrays for SPRi biosensing have been fabricated by photolithography [40] [41], which requires the assistance of a photolithography mask and a series of photoresist, metal deposition, and removal procedures. In our previous work, we demonstrated fabrication of SPRi microarrays based on spatial variation of the metal thickness by photolithography, which included 120 gold wells for simultaneous SPRi analysis [42]. Considering that only the cross-sections of S-shaped channels and the rectangular patterns of the 3D printed Dove prisms can be utilized as the sensing sections for SPRi, the highest theoretical number of analytes that can be assessed simultaneously is 16, leaving a wide margin for improvement of multiplex detection. Therefore, we developed a photolithography-free fabrication method using gold island arrays for SPRi biosensing, which was achieved using a 3D printed E-beam evaporation mask during the E-beam evaporation process; we then evaluated the corresponding SPRi performance. Before deposition of the thin gold islands film directly on the prisms, we designed and fabricated an E-beam evaporation mask for commercial glass microscope slides and coupled them with commercial glass prisms for SPRi sensing (Figure 3.8). Similar to SPRi microarrays on commercial glass microscope slides from our previous work [42], which contain 3 sections of gold well arrays for different SPRi experiments, our 3D printed E-beam evaporation mask for glass microscope slides also contained 3 sections, and each section included 7 $\times$ 6 arrays with 2 mm as the diameter of each circle-shaped pattern. The overall shape of the mask was designed to be a groove, so that the glass slides could be fixed in the groove to ensure

correct array positioning and be easily taped to a fixed position before being placed in a E-beam evaporator.

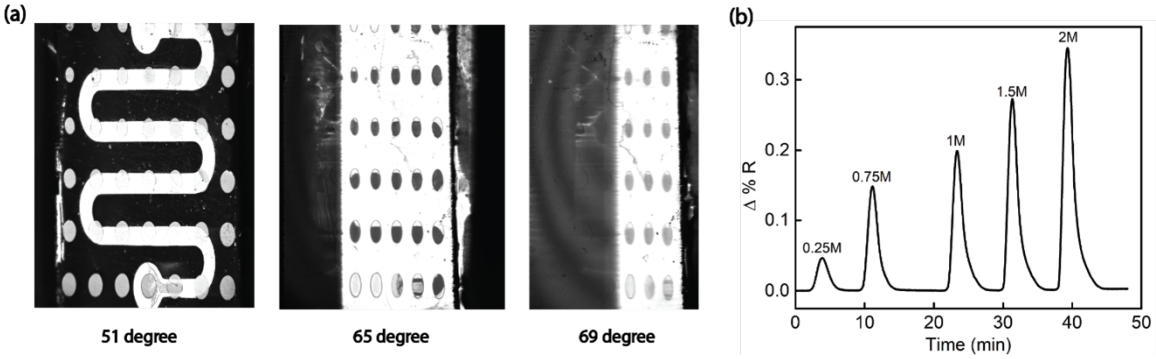

Figure 3.9: (a) Reflected images showing plasmonic resonance for the gold islands glass slide coupling with a commercial glass equilateral prism with 3 different incident light angles. (b) Real-time sensorgram for the gold islands glass slide coupling with a commercial glass equilateral prism by NaCl injections with different concentrations in continuous running nanopure water.

After E-beam evaporation, the slide with gold island arrays was cut and coupled to a commercial SF2 glass prism to test SPRi performance. Reflected images were taken at different incident light angles to illustrate the plasmonic resonance (resonance angle: 65°) of the gold islands slide (Figure 3.9a), with the circle-shaped gold pattern arrays easily defined. Salt solutions of various concentrations were also injected into the system to demonstrate

its high sensitivity to refractive index change; the real-time sensorgram is shown in Figure 3.9b.

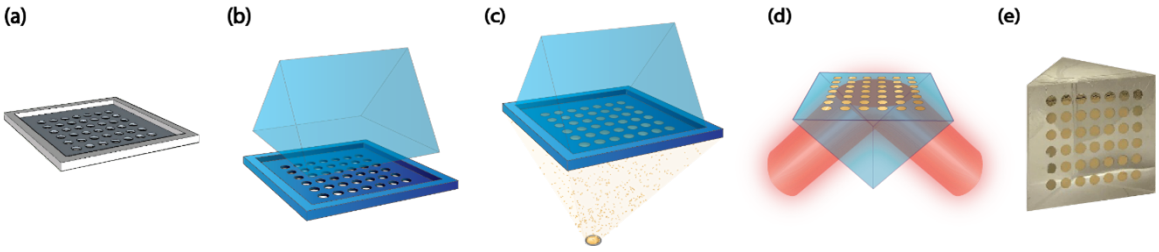

Figure 3.10: Design and fabrication of a 3D printed E-beam evaporation mask for a photopolymer equilateral prism with gold islands arrays for SPRi biosensing. (a) A 3D model for the prism E-beam evaporation mask. (b) The prism can be fixed in the mask for (c) E-beam evaporation. (d) The prism with gold islands arrays for SPRi biosensing. (e) A picture of a photopolymer equilateral prism with gold islands arrays.

After obtaining proof of feasibility of our method of fabrication of plasmonic gold island arrays on glass microscope slides, we applied our approach in direct deposition of gold arrays on a photopolymer equilateral prism surface (Figure 3.10). This E-beam mask shows great potential for combination with 3D printed Dove prisms and as an alternative and more efficient way to achieve multiplex SPRi biosensing with much lower cost compared to the conventional photolithography method.

3.5 CONCLUSION

In this study, we designed and fabricated 3D printed Dove prisms with plasmonic micropattern arrays for high-throughput multiplex SPRi biosensing. Compared with 3D printed equilateral prisms for SPRi, the 3D printed Dove prisms overcame the issues of small sensing area and high resonance incident angle without a change in materials, and simultaneously supported array patterns fabrication for multiplex detection. The 3D printed Dove prism has a sensing angle at 71°, which is 8° smaller than the sensing angle of 3D printed equilateral prisms, thus achieving a 21% larger sensing area and providing more reliable results. Moreover, the prisms were treated with a standard benchtop polishing procedure, and the surface roughness of the printed prisms dropped as low as 10 nm, which is quite close to that of commercial glass prisms (2 nm). Additionally, refractive index sensitivity of the SPRi setup was investigated through salt assays, and protein sensing was tested, indicating that the sensitivity of the 3D printed Dove prism coupled SPRi was comparable to that of commercial glass prism coupled SPRi. To achieve a more efficient multiplex SPRi biosensing platform, a 3D printed mask for E-beam evaporation was also designed and applied to gold islands array fabrication. The 3D printed Dove prism and 3D printed E-beam evaporation mask show great potential as cost-effective and highly sensitive tools to enhance the capacity, speed, and reliability of multiplex SPRi biosensing.

REFERENCES

[1] Jose Muñoz and Martin Pumera. 3d-printed biosensors for electrochemical and optical applications. *TrAC Trends in Analytical Chemistry*, 128:115933, 2020.

[2] Eric MacDonald and Ryan Wicker. Multiprocess 3d printing for increasing component functionality. *Science*, 353(6307), 2016.

[3] Adriano Ambrosi and Martin Pumera. 3d-printing technologies for electrochemical applications. *Chemical Society Reviews*, 45(10):2740–2755, 2016.

[4] Sergio Rossi, Maurizio Benaglia, Davide Brenna, Riccardo Porta, and Manuel Orlandi. Three dimensional (3d) printing: a straightforward, user-friendly protocol to convert virtual chemical models to real-life objects, 2015.

[5] Alexander Lambert, Santino Valiulis, and Quan Cheng. Advances in optical sensing and bioanalysis enabled by 3d printing. *ACS sensors*, 3(12):2475–2491, 2018.

[6] Yuanyuan Xu, Xiaoyue Wu, Xiao Guo, Bin Kong, Min Zhang, Xiang Qian, Shengli Mi, and Wei Sun. The boom in 3d-printed sensor technology. *Sensors*, 17(5):1166, 2017.

[7] Cristian Zaharia, Alin-Gabriel Gabor, Andrei Gavrilovici, Adrian Tudor Stan, Laura Idorasi, Cosmin Sinescu, and Meda-Lavinia Negruțiu. Digital dentistry-3d printing applications. *Journal of Interdisciplinary Medicine*, 2(1):50–53, 2017.

[8] Sunil C Joshi and Abdullah A Sheikh. 3d printing in aerospace and its long-term sustainability. *Virtual and Physical Prototyping*, 10(4):175–185, 2015.

[9] Adriano Ambrosi and Alessandra Bonanni. How 3d printing can boost advances in analytical and bioanalytical chemistry. *Microchimica Acta*, 188(8):1–17, 2021.

[10] Karankumar C Dhankani and Joshua M Pearce. Open source laboratory sample rotator mixer and shaker. *HardwareX*, 1:1–12, 2017.

[11] Qianwen Sun, Jikui Wang, Meihua Tang, Liming Huang, Zhiyi Zhang, Chang Liu, Xiaohua Lu, Kenneth W Hunter, and Guosong Chen. A new electrochemical system based on a flow-field shaped solid electrode and 3d-printed thin-layer flow cell: detection of pb2+ ions by continuous flow accumulation square-wave anodic stripping voltammetry. *Analytical chemistry*, 89(9):5024–5029, 2017.

[12] Daniel Quesada-González and Arben Merkoçi. Mobile phone-based biosensing: An emerging "diagnostic and communication" technology. *Biosensors and Bioelectronics*, 92:549–562, 2017.

[13] Farhang Momeni, Xun Liu, Jun Ni, et al. A review of 4d printing. *Materials & design*, 122:42–79, 2017.

[14] Germán Comina, Anke Suska, and Daniel Filippini. Autonomous chemical sensing interface for universal cell phone readout. *Angewandte Chemie*, 127(30):8832–8836, 2015.

[15] Shashank Pandey, Barun Gupta, and Ajay Nahata. Terahertz plasmonic waveguides created via 3d printing. *Optics express*, 21(21):24422–24430, 2013.

[16] AD Squires, E Constable, and RA Lewis. 3d printed terahertz diffraction gratings and lenses. *Journal of infrared, millimeter, and terahertz waves*, 36(1):72–80, 2015.

[17] Jigang Huang, Qin Qin, and Jie Wang. A review of stereolithography: Processes and systems. *Processes*, 8(9):1138, 2020.

[18] Nirveek Bhattacharjee, Cesar Parra-Cabrera, Yong Tae Kim, Alexandra P Kuo, and Albert Folch. Desktop-stereolithography 3d-printing of a poly (dimethylsiloxane)-based material with sylgard-184 properties. *Advanced materials*, 30(22):1800001, 2018.

[19] Samuel S Hinman, Kristy S McKeating, and Quan Cheng. Plasmonic sensing with 3d printed optics. *Analytical chemistry*, 89(23):12626–12630, 2017.

[20] Jiřı Homola, Sinclair S Yee, and Günter Gauglitz. Surface plasmon resonance sensors. *Sensors and actuators B: Chemical*, 54(1-2):3–15, 1999.

[21] Ibrahim Abdulhalim, Mohammad Zourob, and Akhlesh Lakhtakia. Surface plasmon resonance for biosensing: a mini-review. *Electromagnetics*, 28(3):214–242, 2008.

[22] Wan Maisarah Mukhtar, Razman Mohd Halim, and Hazirah Hassan. Optimization of spr signals: Monitoring the physical structures and refractive indices of prisms. In *EPJ Web of Conferences*, volume 162, page 01001. EDP Sciences, 2017.

[23] Olivier R Bolduc, Ludovic S Live, and Jean-François Masson. High-resolution surface plasmon resonance sensors based on a dove prism. *Talanta*, 77(5):1680–1687, 2009.

[24] Jin Li, Yong Zhao, Haifeng Hu, Qi Wang, and Jing Zhang. Spr based hollow prism used as refractive index sensor. *Optik*, 126(2):199–201, 2015.

[25] Supeera Nootchanat, Wisansaya Jaikeandee, Patrawadee Yaiwong, Chutiparn Lertvachirapaiboon, Kazunari Shinbo, Keizo Kato, Sanong Ekgasit, and Akira Baba. Fabrication of miniature surface plasmon resonance sensor chips by using confined sessile drop technique. *ACS applied materials & interfaces*, 11(12):11954–11960, 2019.

[26] Chutiparn Lertvachirapaiboon, Akira Baba, Kazunari Shinbo, and Keizo Kato. Dual-mode surface plasmon resonance sensor chip using a grating 3d-printed prism. *Analytica Chimica Acta*, 1147:23–29, 2021.

[27] Zhengdong Yang, Alexander S Malinick, Tiantian Yang, Wei Cheng, and Quan Cheng. Gold nanoparticle-coupled liposomes for enhanced plasmonic biosensing. *Sensors and Actuators Reports*, 2(1):100023, 2020.

[28] Ying Liu, Yi Dong, Jessica Jauw, Matthew J Linman, and Quan Cheng. Highly sensitive detection of protein toxins by surface plasmon resonance with biotinylation-based inline atom transfer radical polymerization amplification. *Analytical chemistry*, 82(9):3679–3685, 2010.

[29] JM Pitarke, VM Silkin, EV Chulkov, and PM Echenique. Theory of surface plasmons and surface-plasmon polaritons. *Reports on progress in physics*, 70(1):1, 2006.

[30] Jiři Homola, Sinclair S Yee, and Günter Gauglitz. Surface plasmon resonance sensors. *Sensors and actuators B: Chemical*, 54(1-2):3–15, 1999.

[31] Md Saiful Islam, Abbas Z Kouzani, Xiujuan J Dai, and Wojtek P Michalski. Investigation of the effects of design parameters on sensitivity of surface plasmon resonance biosensors. *Biomedical Signal Processing and Control*, 6(2):147–156, 2011.

[32] Zhuangzhi Wang, Thomas Wilkop, Jong Ho Han, Yi Dong, Matthew J Linman, and Quan Cheng. Development of air-stable, supported membrane arrays with photolithography for study of phosphoinositide- protein interactions using surface plasmon resonance imaging. *Analytical chemistry*, 80(16):6397–6404, 2008.

[33] Bin Wang and Bosoon Park. Immunoassay biosensing of foodborne pathogens with surface plasmon resonance imaging: a review. *Journal of Agricultural and Food Chemistry*, 68(46):12927–12939, 2020.

[34] Nagaraju Chada, Krishna P Sigdel, Raghavendar Reddy Sanganna Gari, Tina Rezaie Matin, Linda L Randall, and Gavin M King. Glass is a viable substrate for precision force microscopy of membrane proteins. *Scientific reports*, 5(1):1–8, 2015.

[35] Guy Beadie, Michael Brindza, Richard A Flynn, A Rosenberg, and James S Shirk. Refractive index measurements of poly (methyl methacrylate)(pmma) from 0.4–1.6 μm. *Applied optics*, 54(31):F139–F143, 2015.

[36] Matthew J Linman, Abdennour Abbas, and Quan Cheng. Interface design and multiplexed analysis with surface plasmon resonance (spr) spectroscopy and spr imaging. *Analyst*, 135(11):2759–2767, 2010.

[37] Christopher Lausted, Zhiyuan Hu, Leroy Hood, and Charles T Campbell. Spr imaging for high throughput, label-free interaction analysis. *Combinatorial chemistry & high throughput screening*, 12(8):741–751, 2009.

[38] S Viridi et al. Automation of data acquisition surface plasmon resonance (spr) based on labview. In *Journal of Physics: Conference Series*, volume 1127, page 012003. IOP Publishing, 2019.

[39] F Wu, PA Thomas, VG Kravets, HO Arola, M Soikkeli, K Iljin, G Kim, M Kim, HS Shin, DV Andreeva, et al. Layered material platform for surface plasmon resonance biosensing. *Scientific reports*, 9(1):1–10, 2019.

[40] Eric Ouellet, Christopher Lausted, Tao Lin, Cheng Wei T Yang, Leroy Hood, and Eric T Lagally. Parallel microfluidic surface plasmon resonance imaging arrays. *Lab on a Chip*, 10(5):581–588, 2010.

[41] Alexander S Malinick, Alexander S Lambert, Daniel D Stuart, Bochao Li, Ellie Puente, and Quan Cheng. Detection of multiple sclerosis biomarkers in serum by ganglioside microarrays and surface plasmon resonance imaging. *ACS sensors*, 5(11):3617–3626, 2020.

[42] Abdennour Abbas, Matthew J Linman, and Quan Cheng. Patterned resonance plasmonic microarrays for high-performance spr imaging. *Analytical chemistry*, 83(8):3147–3152, 2011.

Chapter 4

3D-Printed Microfluidic Devices for On-chip Cell Lysis and Lipid Extraction towards Enhanced Lipidomic Profiling

4.1 ABSTRACT

Microfluidic lipid extraction is a useful tool for cell−based lipidomics research owing to small sample volume, high throughput capability and efficient mass transfer between the two extraction phases. Current work with lipid extraction via microfluidics has been hindered by limitations associated with sophisticated fabrication and assembly processes. We report here the design and fabrication of a highly efficient microfluidic device by using

3D printing technology for onchip cell lysis and lipid enrichment of cells for lipidomic profiling with MALDI−MS. The platform consists of a printed micropillar mixer where cells and organic extraction phase are injected for flow-through lysis. An on−chip reservoir is built to separate the two phases in which the organic layer is collected for subsequent MS analysis. The mass transfer between the two phases was modeled and simulated by a computational fluid dynamics study, and the efficiency in cell lysis in different extraction solvent systems was characterized by fluorescence microscopy. Results showed a marked increase in extraction performance with the micropillar mixer as compared with the standard Bligh−Dyer method. For lipid profiling of C. *reinhardtii* cells by MALDI-MS, over 65 lipid species from the MGDG, DGDG, DGTS, and TAG lipid families have been identified. The effect of organic solvents on extraction and lipid profiles was also investigated, and the results indicated that the extractant formula has a diverse impact on collection of certain types of lipid species. This may provide a useful selection guidance when applied to targeted enrichment of lipids with specific cells. 3D printed microfluidic chips, fabricated with straightforward steps and of high efficiency, offer new technical avenues in lipidomics study and can provide a novel platform for lipid profiling research.

4.2 INTRODUCTION

Lipids in cell membranes play critical roles in many aspects of cellular functions, such as membrane formation, bioactive inter− and intracellular signaling, and energy storage [1]. Understanding the composition and changes of lipid membranes under various conditions/states is essential to the deciphering of many cellular mechanisms and even dis-

ease progression [2] [3]. Lipidomics, a study aiming at identification and quantification of a large scale of lipid species in organisms, has attracted widespread attention [4] and has been viewed as a powerful tool to understand molecular interactions and cytotoxicity through tracking changes in lipid composition associated with environmental changes induced by chemicals/drugs/toxicants [5]. Considerable progress has been achieved in lipidomics that spans the fields of drug screening, biomarkers discovery and environmental toxicology [6] [7]. Traditionally, analytical methods including high−performance liquid chromatography (HPLC), thin−layer chromatography (TLC) and high resolution ^{31}P NMR spectroscopy have been utilized to conduct lipid analysis. These methods, though effective, have a range of limitations including long analysis time, low throughput, long-standing experience requirement, and lack of sensitivity [8].In recent years, mass spectrometry technology has also become a promising, powerful tool to enable lipid profiling and monitoring of lipidomic changes in complex samples [9] [10]. Matrix−assisted laser desorption/ionization mass spectrometry (MALDI−MS) is one of the most commonly used MS technique for lipidomic study and shows great advantage due to simple sample preparation, high throughput, high sensitivity and rapid analysis [11] [12].

Sample treatment is currently a performance−limiting step in lipid analysis using MALDI−MS; typically, an extraction process of cells or tissues is needed in order to remove interfering species before reliable results can be obtained. Traditional extraction methods such as liquid−liquid extraction (LLE) and solid phase extraction (SPE) are utilized but they require large sample volumes and are time−consuming processes [12]. Therefore, a fast, high−throughput and efficient approach is needed, especially when dealing with

limited sample volumes. Several approaches have been proposed to tackle this problem. Guillaume−Gentil et al. reported metabolites analysis of single cells by a combination of fluidic force microscopy and MALDI−TOF MS [13]. Do et al. demonstrated an optically guided single cell combining with MALDI−MS method for lipid, peptide and protein profiling to classify cell types [14]. We have also previously presented a lipid profiling study on a thin gold film with nanoplasmonic microarray by fluorescence positioning and MALDI−MS lipid identification [15]. Although these lipid analysis methods have demonstrated the capability to capture information via a fast analysis process, improvements are still necessary to enable lipid analysis for difficult−to−detect molecules and broader applications with varied cell types.

Microfluidic devices have been widely used in sample treatment, particularly in sample mixing and separation [16] [17]. Because of the micrometer scale of the channel size, these devices show remarkable properties of large surface to volume ratio, low sample requirements, enhanced sensitivity, portability, easy modularity and automation. As such, multiple microfluidic platforms for lipid extraction have found increased use in recent years with reported high extraction efficiency [18] [19] [20] [21]. Comparing with the conventional extraction column, the fluid residence time in microfluidic devices is greatly shortened and a closed extracting environment is achieved as the contactor size is significantly miniaturized [19] [22]. Combining microfluidics lipid extraction with MS lipid analysis offers a rapid, simple and high−throughput approach for lipidomic study. Sim and coworkers reported a PDMS based integrated microfluidic platform for cell culturing, lipid extraction followed by quantitative lipid analysis, using a microchannel with a micropillar array as the algae

filter fabricated by standard photolithography [23]. Johnson and coworkers developed a microfluidic system for cell lysis and lipid extraction by packing microchip with silica beads and used a nanoelectrospray ionization quadrupole time−of−flight tandem mass spectrometer (nanoESI−Q−TOF MS/MS) for lipidomics profiling [24]. However, these approaches required complex fabrication by photolithography or packed silica beads that could be replaced using more cost effective methodologies.

The rapid development of 3D printing technology has greatly impacted the microfluidic field where 3D printed devices have gained significant use due to ease in design and rapid fabrication protocols. 3D printing is capable of prototyping structures on the microscale and has started to offer competitive performance when compared to soft lithography, especially when the resolution requirements are not as high [25]. This provides a unique avenue to solving the complex fabrication issues in previously described microfluidic devices. With 3D printing technology, various microfluidic devices can be quickly designed, tested, prototyped, and fabricated [26]. In this work, we report an effective approach for lipidomic profiling of algae cells by on−chip lipid extraction with a 3D printed microfluidic device and MALDI−MS (Figure 4.1). The microfluidic device contains two parts: a micromixer that attains cell lysis and an on−chip reservoir to separate extraction phases. The printed mixing section yielded strong cell lysis performance and showed high extraction efficiency from the enhanced mass transfer, which was further characterized and confirmed by numerical simulations. The on−chip reservoir was used for layer separation and phase collection, and the effectiveness of the microfluidic platform was demonstrated in lipid profiling of C. *reinhardtii* cells by MALDI−MS. Effect of organic extraction solvents on lipid

profiles in MALDI−MS was also investigated to maximize the examination on cell lysates with varied lipid composition. The combination of printed microfluidics and MALDI−MS could offer faster and efficient lipid analysis, providing robust and comprehensive profiles that can be further expanded with extraction solvent optimization.

4.3 EXPERIMENTAL

4.3.1 Materials

Ethyl Acetate, acetonitrile, chloroform, methanol, 2−propanol and methyl sulfoxide (DMSO) were obtained from ThermoFisher Scientific Co (Fair Lawn, NJ). Blue water-soluble food dye was obtained from Tone Brothers, Inc (Ankeny, IA). Oil Red O and Super dihydrobenzoic acid were purchased from SIGMA−ALDRICH (St. Louis, MO). 1−Octanol was purchased from Frontier Scientific Inc (Logan, UT). SYLGARD 184 Silicone Elastomer was obtained from Dow Corning (Midland, MI). Hemocytometer was purchased from Hausser Scientific (Horsham, PA). C. *reinhardtii* (+) bacteria-free (# 152040), and sterile Algae-Gro® medium were obtained from Carolina Inc (Burlington, NC). High purity water (>18 MΩ $cm^{-}1$) was produced by a Barnstead E-Pure water purification system.

4.3.2 Flow Simulations

Numerical simulation of the droplet breakup and velocity field of the microfluidic setup was carried out by COMSOL Multiphysics. Level set method was used to simulate two-phase droplets formation/breakup through a simplified microfluidic model. The slip

length β of the wetted wall boundary condition was set as 5μm. Single phase velocity field simulation was conducted with the model of the same size as the microfluidic platform.

4.3.3 3D Printed Microfluidic Platform and On-chip Phase Separation

The microfluidic chip templates were designed in SketchUp (Trimble, Inc., Sunnyvale, CA) and printed using a Formlabs Form 2 (Somerville, MA) stereolithography printer. The printed molds were washed in an isopropanol bath and dried under compressed air for 3 times. A CL-1000 UV crosslinker (UVP Inc., Upland, CA) were used to post-cure the printed device for 1h [27]. PDMS prepolymer was poured into the molds, followed by degassing in the desiccator and hardening in the oven. The cured PDMS was then removed from the mode using a razor blade and attached to a plasma cleaned microscope glass slide. The inlets of the PDMS micromixer were connected to two syringes of a dual channel syringe pump, and the outlet was connected to the PDMS reservoir using tubing. For the on-chip separation experiments, the organic phase and aqueous phase were injected at the flow rate of 0.2mL/min.

4.3.4 Algae Culture Conditions, Cell Disruption and Lipid Extraction

C. *reinhardtii* cells were cultured in 20mL glass vials containing medium at room temperature under a "cool white" fluorescent light with an intermittent 12-hour light and 12-hour dark cycle. The cells were seeded and cultured for two weeks until they reached stationary phase. All cells were washed with high purity water 3 times before introduction into extraction processes to eliminate possible interference of culture medium in the lipid extract. Cell disruption and lipid extraction experiments were conducted by both microfluidic

and bulk extraction for comparison. For microfluidic cell lysis and lipid extraction, aqueous phase containing algae cells and different organic phases were introduced to the microfluidic system via two inlets, and the resulting two phases were collected separately from the reservoir after the separation process is completed. For bulk lipid extraction, a modified Bligh-Dyer method was used [23] [28]. Briefly, 600μL pre-mixed chloroform/methanol (1:2 v/v) solution was mixed with 500μL washed C. *reinhardtii* solution. The mixed solution was then vortexed for 1h followed by centrifugation at 2000rpm for 10min. The lower phase containing chloroform and extracted lipid was collected via micropipette. To compare the efficiency between bulk extraction and microfluidic method, additional bulk extraction was tested using ethyl acetate/acetonitrile (4:3 v/v) solution with the same volume ratio to the cell solution (1:1 v/v).

4.3.5 Fluorescence Imaging and Cell Counting

A fluorescence microscope with a TRITC filter cube and a Qimaging Retiga 1300 camera was used for characterizing algae cells and analyzing lipid extracts (Ex/EM/BPF 530/590/570). Cell counting was achieved using a hemocytometer. The original algae cell suspension or the collected solution after microfluidic extraction was firstly diluted 10 times and then loaded into the V-shaped well using a pipette tip. The sample was settled for 10 min and then taken to the microscope stage for cell counting.

4.3.6 Fabrication of gold microchip arrays for MALDI-MS substrate

BK-7 microscope slides were firstly cleaned with piranha solution (H_2SO_4:H_2O_2, 3:1 v/v, Caution!), followed by rinsing with ethanol and ultrapure water. The slides were

then dried by nitrogen [29]. The gold-patterned microwell arrays were fabricated based on a previously published method [15] [30]. Briefly, a 2nm chromium film as the adhesion layer and a 200nm gold film were deposited by E-beam evaporation. The photoresist was then lifted off via an acetone gun to reveal the arrays. Another 2/50nm chromium/gold film was deposited onto the surface to generate gold-patterned microwell arrays. In this work, three sections of 10 x 12 arrays with gold wells of 800 µm diameter size were fabricated on one glass slide. The freshly prepared chips were stored in a vacuum desiccator before use.

4.3.7 Lipid analysis using TLC and MALDI-MS on microchip

The lipid extract (organic phase) from the microfluidic chip was firstly concentrated 20 times by the nitrogen blowdown method. For lipid analysis by TLC, original algae solution, microfluidic blank, lipid extract by microfluidic and Bligh-Dyer methods were spotted on silica gel matrix aluminum TLC plates, separated by a solution of hexane/diethyl ether/acetic acid (80:30:1 v/v/v). and stained in an iodine vapor jar [23]. MALDI-MS experiments were performed by loading the concentrated lipid extracts onto the gold microwells followed by applying super-DHB as the matrix. MALDI-MS analysis was carried out by AB-SCIEX 5800 MALDI TOF/TOF Mass Spectrometer (SCIEX, Framingham, MA) using the positive mode with a laser fluence of 5500 au. The MS spectra was obtained for 200 shots collected by the sample. The MALDI-MS analysis of intact cells was conducted using the procedure previously reported by our group [15].

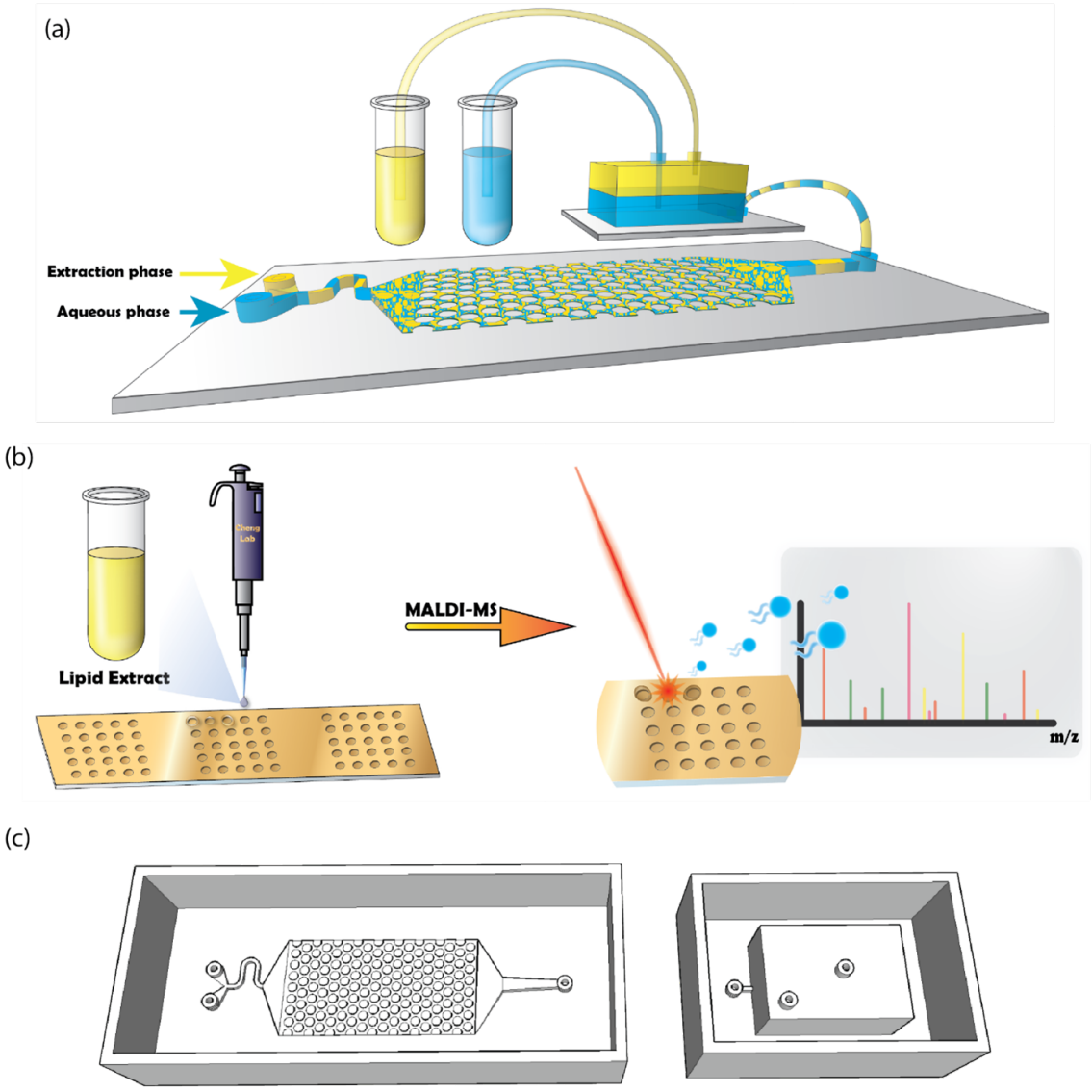

Figure 4.1: 3D printed microfluidic platform for MALDI-MS lipidomic study. (a) A scheme of on-chip thorough mixing and separation of extraction phase and aqueous phase. (b) A scheme of the workflow for lipid extract sampling on the microarray chip for MALDI-MS lipidomic study. (c) A picture of a 3D model of the print-out modes for the microfluidic system.

4.4 RESULTS AND DISCUSSION

4.4.1 Design and Fabrication of Microfluidic System for Onchip Cell Lysis and Extraction

The 3D printed microfluidic system contains two parts: a micromixer for thorough mixing and an on-chip reservoir for phase separation (Figure 4.1). Both were fabricated by 3D printing of the microfluidic templates, followed by PDMS molding. The PDMS pieces were then attached to a glass slide. For the micromixer, the two inlets are connected with an S-shaped microchannel for premixing. This was followed by a wedge-shaped channel for raising the velocity field of the fluid before going to the mixer. The micromixer consists of an array of cylinder-shaped micropillars (700µm in radius, 75µm in height and 400µm for interspace). The design is aimed to generate an anisotropic flow for fluid mixing [31]. The mixing channel at 400µm spacing is sufficient for most cell analysis and will not become blocked even with microalgal cells (C. *reinhardtii*, ∼10µm in diameter). The micropillars are much smaller than the droplets generated near the microchamber inlet. The droplet size has been reported to link to various modes of mass transport in microfluidics. If liquid droplets are large enough, their contact with the inner wall of the microchannel will transform the droplets into a plug shape and thus a circular flow is resulted in both the dispersed phase and the surrounding continuous phase, which can significantly enhance the mass transfer between phases [32]. However, if the droplets size is smaller than the microchannel, the liquid-liquid system will form a "bubbly flow", which provides a larger mass transfer area, especially with a high number of droplets [18] [33]. Our micropillar array design utilizes both factors to provide an enhanced mass transfer and therefore improved

extraction performance. Inner circular flow is expected to occur when droplets flow in the S shaped channel and between the micropillars, and these droplets breakup after flowing through the microarrays to form a large number of "bubbly flow", providing a larger mass transfer area. The on-chip reservoir has a cuboidal shape (2cm in length, 1.4cm in width and 0.84cm in height), which provides a sizable space for fluid accumulation and phase separation. The size of the reservoir was actually optimized to ensure sufficient time for phase settling and separation, and can be modified to accommodate changes for different sample volumes. The reservoir has two outlets on the top section for collection of different phases.

To test lipid extraction by the printed microfluidic chip, an extraction phase and an aqueous phase (containing cells) were injected to the micromixer at the flow rate of 0.2mL/min. To enhance the visual characterization of the mixing, a blue food dye was added in the aqueous phase while Oil Red O dye was dissolved in the oil phase of ethyl acetate. The two phases were well separated inside the reservoir (Figure 4.2a). The lipid extraction and collection of a 200µL sample took about 30s. For the subsequent MALDI-MS analysis, gold microchip arrays were used for easy comparison to a previous work [15]. The plasmonic chip has shown improved MALDI performance because of thermal desorption increase [34] and surface charging suppression [35]. The concentrated lipid extract from the 3D microfluidic extraction was directly spotting on the gold chip for lipid analysis.

4.4.2 Droplet Breakup and Velocity Field Simulation

Although micro-structured mixing devices have attracted broad attention for their effective liquid-liquid extraction [36], mass transfer between phases is still a focal point of

improvement. Microfluidics in general enhances mass transfer as compared to conventional extraction columns due to large contact area [18]. In addition, flow rate [37] and the large surface-to-volume ratio of the droplets [19] are important factors to consider when designing better microflow extractors. An important improvement is the introduction of microscale obstacles in the flow channel, which facilitates droplet breakup [38] and forms smaller droplets with an overall larger contact surface between phases. We have adopted this concept in this micromixer design. To understand the effects of pillar dimension and spacing on mixing efficiency, computational fluid dynamics (CFD) study of droplet breakup was carried out with COMSOL Multiphysics.

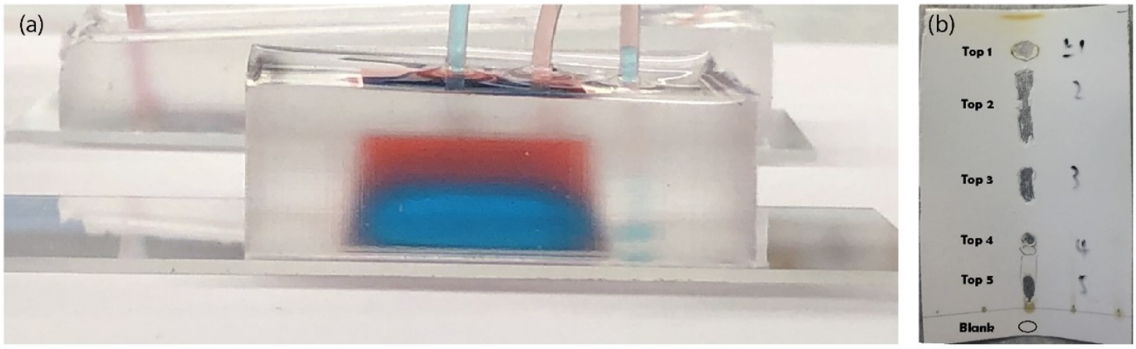

Figure 4.2: Pictures of (a) layer separation in the on-chip reservoir and (b) sampling spots for TLC-MALDI lipid analysis.

We chose to first focus on the breakup of the droplets induced by the micropillar arrays and velocity field distribution in one phase flow in the field simulation study. Given the microscale dimensions of the channels and relatively slow flow velocities, the printed pillar system can be considered to have a low Reynolds number. Thus the flows in this platform are assumed laminar and incompressible [39]. A conservative level set method (LSM) has been applied to the CFD study where the interface between the primary and secondary phase was tracked by the solution of an equation containing a level set function (ϕ) [40]. The level set function is among the range from 0 to 1 and equals to 0.5 (ϕ=0.5) at the fluid interface between the two phases [41]. The governing equations for two-phase simulation include Navier-Stokes equation (4.1), continuity equation (4.2) and the level set equation (4.3), which can be expressed as:

$$\rho\frac{\partial u}{\partial t} + \rho(\, u.\nabla)\, u = \nabla.[\, -pI + \eta(\, \nabla u + (\, \nabla u)^{\,T})\,] + \sigma\kappa\delta n \tag{4.1}$$

$$\nabla \cdot u = 0 \tag{4.2}$$

$$\frac{\partial \phi}{\partial t} + u \cdot \nabla\phi = \gamma\nabla \cdot [\, \varepsilon\nabla\phi - \phi(\, 1-\phi)\, \frac{\nabla\phi}{|\nabla\phi|}] \tag{4.3}$$

where ρ, η, σ and δ denote the density, dynamic viscosity, surface tension coefficient and the function concentrated at the interface of the two fluids, respectively, p is the pressure, I is the identity matrix, n is the normal vector to the interface which points to the inner droplet,

γ and ε are both stabilization parameters in which the former represents re-initialization parameter and the latter the thickness of the interface [42] [43].

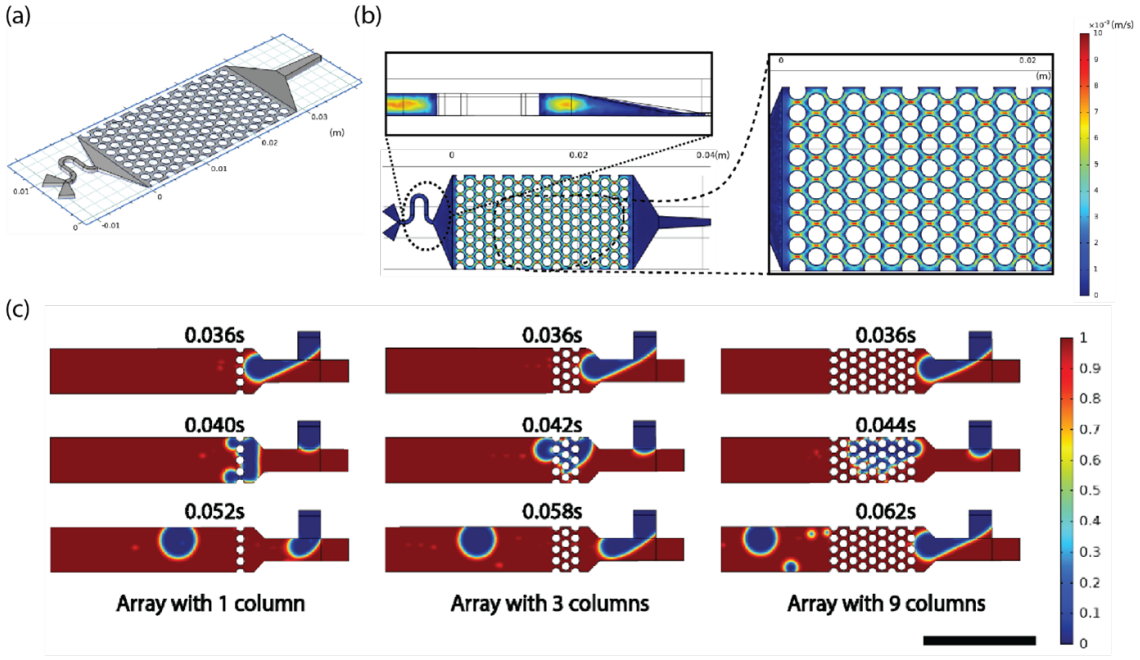

Figure 4.3: Fluid simulation. (a) Three-dimensional (3D) geometry of the micromixer for the velocity field simulation. (b) Single-phase velocity field simulation for water in the micromixer with zoom-in images of the velocity field plot of the selected longitudinal section and cross section. (c) Two-phase simulation of droplets formation in a microfluidic T-junction and droplets breakup in microfluidic channels with different number of columns of micropillars. Bar=500µm.

Figure 4.3a shows a simulated velocity field distribution within the microfluidic device. In this module, the single water phase was injected at the flow rate of 0.2mL/min, which was kept consistent throughout the microfluidic lipid extraction process. Zoomed-in images of the velocity plot is shown in Figure 4.3b for the longitudinal section of the S-shaped channel and cross section of the main part of the micromixer. The linear flow velocity can be seen reaching as high as 9×10^{-3} m/s while flowing through the gap between micropillars, which is more than 5 times higher than in other areas. This drastic velocity change meets our expectation for the design and is the reason behind the dramatic increase in mass transfer efficiency of the extractor.

A more sophisticated modeling was carried out to simulate time dependent droplet breakup in two phases. The main geometry of the design is a T-junction-like microchannel with 2 inlets (100 µm in width) and 1 outlet (200µm in width). Water was chosen as the continuous phase flowing at the rate of $1.3 \times 10^{-2} m^2/h$, while ethyl acetate is the dispersed phase at the rate of $2.6 \times 10^{-3} m^2/h$. The mixed fluid was simulated by flowing through an array of cylinder-shaped micropillars (18.5µm in radius and 13µm rim-to-rim). A varied number of micropillar columns, including 1, 3 and 9, were tested in the simulation module with a time range between 0 and 200ms.

The process of daughter droplet formation, in the form of flow through the micropillar array and subsequent droplet breakup, was monitored at different time intervals for each model. The initial microdroplets were formed at the intersection of the two inlets. Since the diameter of formed droplets is much larger than the gap between the micropillar obstacles, droplets were deformed while flowing through the microarrays, which dramati-

cally increased the contact interface between the aqueous and oil phases. When the number of columns was increased to 9, more daughter droplets were observed based on the simulation results, indicating better droplets breakup efficiency and larger surface area of the droplets with the increasing number of micropillar columns (Figure 4.3c). We have 18 micropillar columns for the lysis chip.

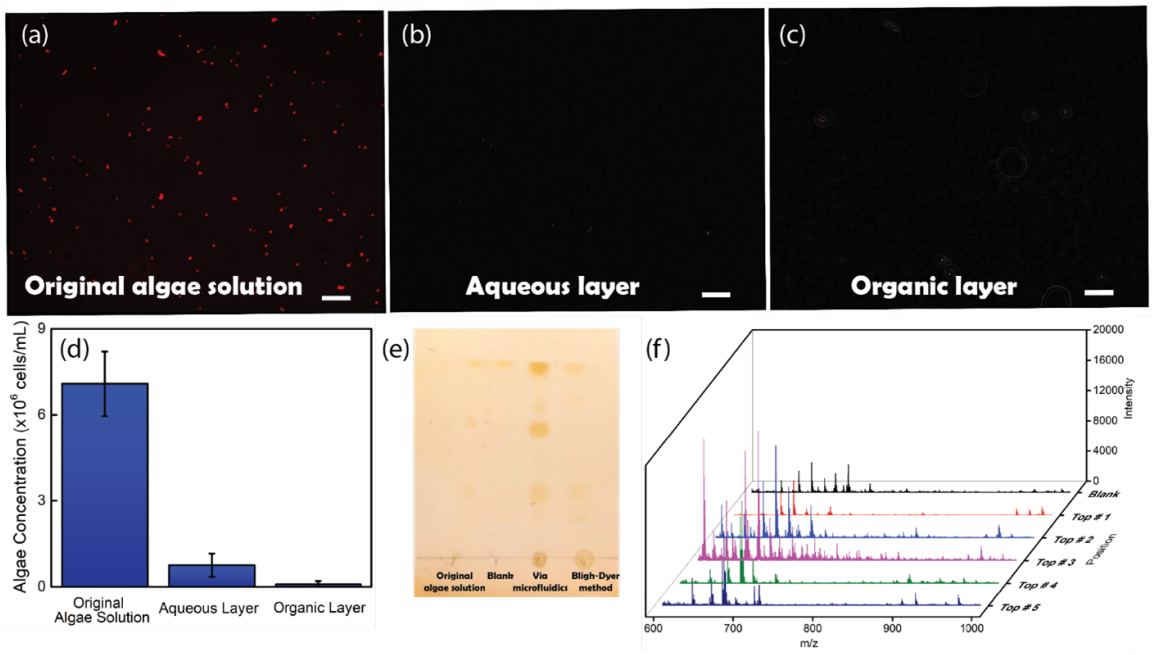

Figure 4.4: Cell lysis and lipid extraction of microalgae solution through the microfluidic device. Fluorescence images of (a) the original algae solution before flowing through the micromixer, (b) the aqueous layer and (c) organic layer collected after cell lysis via the micromixer. Bar=50µm (d) Intact algae cells concentration by cell counting of original algae solution, aqueous layer and organic layer collected from the microflow extractor. (e) TLC image of the original algae solution, microfluidic blank, lipid extract by microfluidic and Bligh-Dyer methods. (f) MALDI-MS spectra of lipids at different lipid spots of the lipid extract via microfluidic device on TLC plate.

4.4.3 Comparison of Cell Lysis by the Printed Microfluidics and the Bligh-Dyer Method

The application of the 3D printed microfluidics for online cell lysis is performed with microalgae cells. Many microalgae species, including C. *reinhardtii*, containing robust and strong multi-layered cell walls, present great challenges for lipid extraction [44]. The cell walls of some algae species even inhibit entry of conventional organic solvents into the cell, which considerably reduce extraction efficiency [45]. The cell lysis performance was evaluated by fluorescence imaging and cell counting. Algae cells show strong fluorescence signal due to abundant amount of pigments, in particular chlorophyll, within the cell membrane [46]. When the cell membranes are disrupted, the fluorescent substances are dispersed into the solution, resulting in loss of signal [47]. Figure 4.4a-c show fluorescence images taken for the original algae solution and after microfluidic extraction. Drastic decrease of the fluorescence spots was observed in both phases. Cell disruption was also verified by cell counting, in which microalgae cells decreased by over 90% in the collected aqueous phase and oil phase, indicating a high efficiency (Figure 4.4d).

The Bligh-Dyer method is a standard lipid extraction method for algae, which is known for the highest extraction efficiency [23]. We compared the algae lipid extraction by the printed microfluidics vs a modified Bligh-Dyer approach (Figure 4.4e). An ethyl acetate/acetonitrile (4:3 v/v) solution was used as the extraction phase for microfluidic extraction. Four samples, including the original algae solution, microfluidic blank, lipid

extracts by microfluidics and Bligh-Dyer method, were spotted on the TLC plate. Lipid extraction by the microfluidic platform displayed higher extraction efficiency, based on the darker lipids spots as compared with those by the Bligh-Dyer method. Lipids for the intact algae cells, however, were not well separated. To identify the lipid species separated on TLC plate, we collected the lipids on different lipid spots followed by lipid analysis via MALDI-MS.

Lipid	Top #1	Top #2	Top #3	Top #4	Top #5
DGTS (32:1)			710.6236		
DGTS (36:5)			758.4899		
Chlorophyll a				871.7355	
TAG (52:10) or TAG (52:2)					881.4703
TAG (52:7)				887.7219	
TAG (54:2)				925.7013	
DGDG (34:7)				929.7182	
DGDG (34:2)		939.7578			
DGDG (34:1)				941.6881	
DGDG (36:2)	983.2314				

Table 4.1: Major lipid components identification and corresponded m/z values for different lipid spots on the TLC plate.

Unlike the TLC coupled MALDI-MS method reported by Fuchs et al. [48] and Luther et al. [49] by utilizing a dedicated TLC-MALDI-TOF MS adapter target, we directly col-

lected lipid samples on different lipid spots (top #1 to top #5) together with silica gel using a clean razor blade and resuspend it in chloroform (Figure 4.2b). Figure 4.4f shows the MALDI spectra of lipid sample of different spots on TLC plate, revealing lipid identity and their distribution in different spots.

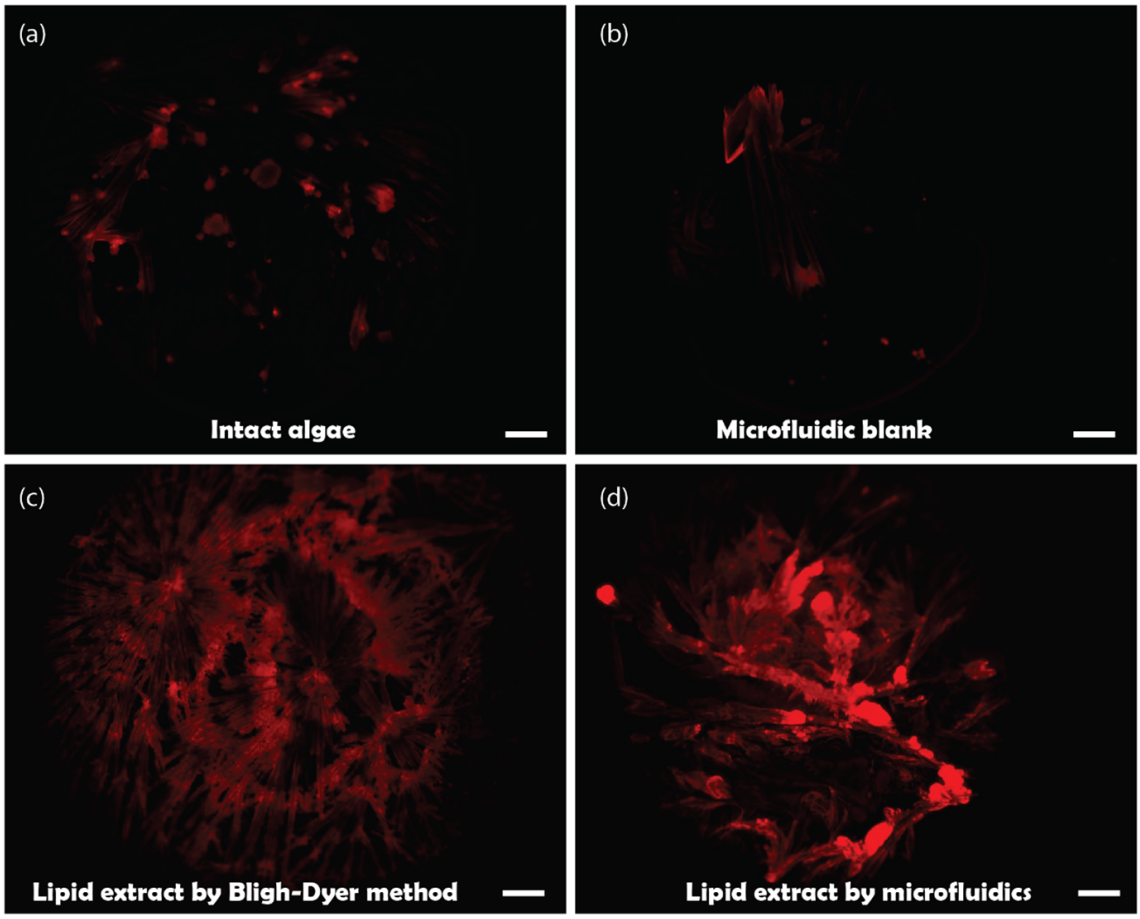

Figure 4.5: Fluorescence images of sampling (a) intact algae, (b) microfluidic blank, (c) lipid extract by Bligh-Dyer method in bulk and (d) lipid extract by microfluidic extraction method on a gold microwells chip.

Based on the major peaks of each MALDI spectra which did not appear on other spots, we were able to identify the major lipid components for different lipid spots (Table 4.1). Further analysis was performed with fluorescence microscopy for intact cells and treated samples on the gold microwell substrate (Figure 4.5). The high fluorescence signal of the microfluidic lipid extract confirms the efficiency by microfluidic extraction, which agrees with the TLC results.

4.4.4 Extraction Efficiency and Lipid Analysis by MALDI-MS

More detailed analysis of lipid extraction was conducted by using the liquid phase from ethyl acetate/acetonitrile mixed solvent (EA/ACN) (4:3 v/v) and MALDI-MS (Figure 4.6a). The analysis of the algae's aqueous layer was also performed for comparison purposes. Compared to the organic layer, aqueous layer has no significant lipid peaks in the mass spectra except for a weak Chlorophyll band around m/z=871.57, indicating the majority of the lipids has been extracted into the organic phase. Lipid extraction yields were compared for the microfluidic platform and bulk extraction with the same solvent (EA/ACN) as well as chloroform/methanol (Bligh-Dyer method) (Figure 4.6a, 4.6c). Using 4 major lipid species for comparison, we achieved a 40% increase with the microfluidics against the bulk extraction with the same solvent (EA/ACN), and a 21% increase vs the chloroform/methanol in bulk (Bligh-Dyer method). The results point to a much-enhanced extraction, indicating that microfluidic extraction has a better performance than approached in bulk due to improved mass transfer.

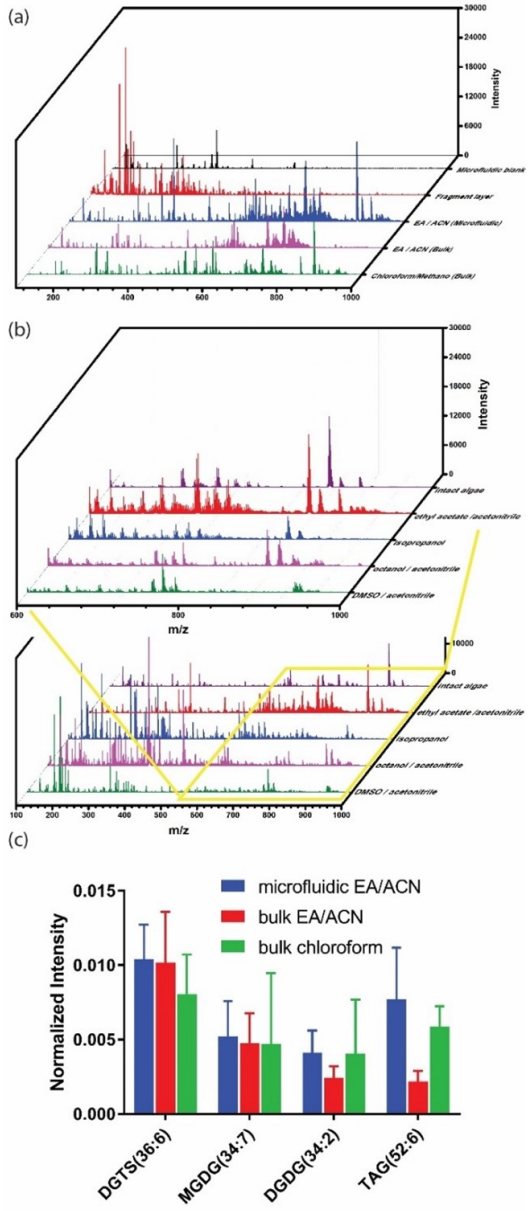

Figure 4.6: MALDI MS analysis. (a) MS spectra of microfluidic blank (dark purple), fragment layer (red) and lipid extract (blue) via the microfluidic platform, lipid extract in bulk using EA/ACN (purple) and chloroform/ methanol (green) as the extraction phase. (b) MS spectra of algae single cell (dark purple) and lipid extract using different extraction phases: red for EA/ACN, blue for isopropanol, purple for octanol/ACN and green for DMSO/ACN. The top spectra is a zoom-in spectra at m/z range from 700-1000. (c) Comparison of lipid extraction efficiency via microfluidic and in bulk (EA/ACN and chloroform/methanol are chosen as the extraction phase) by the differences of selected lipid profile.

4.4.5 Lipid Profiles of C. *reinhardtii* Cells by Different Extraction Reagents

Lipid extraction of cells is known to highly depend on lipid diffusion properties; the selectivity of the extractant also plays an important role [50]. It has been reported the generation of lipid profile highly relies on the extraction efficiency and selection of extractant, where the difference in the partitioning of the lipid species into the organic phase is a significant factor [51]. For example, in Bligh-Dyer method, methanol is typically used to disrupt the hydrogen bonding networks or electrostatic forces between lipids and proteins, and chloroform is used to form the organic layer [28]. In PDMS microfluidic systems, selection of the extraction solvent can be complicated because PDMS can swell in a number of organic solvents [52], which may compromise the sealing of the device and affect the channel shape maintenance. PDMS has a large swelling ratio in the solvent with similar solubility parameter δ as itself ($\delta = 7.3 cal^{1/2} cm^{-3/2}$) [53]. Therefore, methanol and chloroform system are not suitable to the microfluidic extraction. We thus have tested a number of common organic solvents for lipid extraction, including EA, octanol and DMSO, and coupled these solvents with ACN for disrupting cell membranes in lipid extraction. We also tested the extraction performance of isopropanol that was previously reported by Lim et al. [23]. Figure 4.6 shows the MALDI-MS spectra obtained using four extractants (EA/ACN, isopropanol, octanol/ACN and DMSO/ACN). The results were also compared with the direct, single cell method that was previously reported by our group [15] (Figure 4.6b).Microfluidic blank samples by injecting only extraction phase at both inlets are illustrated in Figure 4.7 as the reference. Detailed lipid profiling was conducted using different extraction solvent systems, and Figure 4.8 summarizes the results.

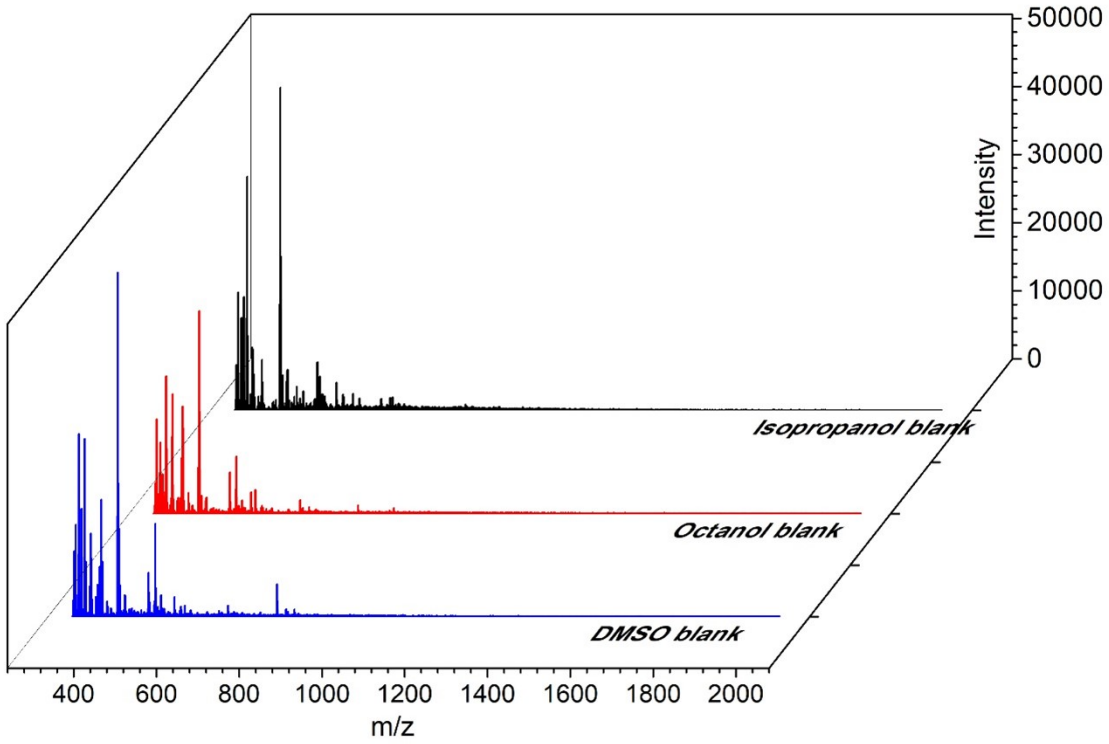

Figure 4.7: Microfluidic blank MS spectra using different organic solvents (Isopropanol, Octanol/ACN and DMSO/ACN).

The focus of the analysis was placed on lipid components of four major lipid classes: MGDG, DGDG, DGTS and TAG. Within a major lipid class, lipid species can be further differentiated by fatty acid chain length and degree of unsaturation. Overall, we were able to unambiguously identify 68 lipid species (including 5 MGDG species, 16 DGDG species, 23 DGTS species and 24 TAG species) with the microfluidic extraction. DMSO/ACN was shown to have higher extraction efficiency towards MGDG and DGDG, while EA/ACN showed better performance in DGTS and TAG extraction. Compared to the intact single cell method previously reported, microfluidic extraction provides an overall much higher signal intensity for most of the lipid species. Specifically, lipid species such as MGDG (34:7), MGDG (34:6), DGDG (34:3), DGDG (36:6) DGDG (34:0), DGTS (35:3), DGTS (35:2), and DGTS (38:4) showed an over 3 times increase in the lipid peak intensity over the intact single cell method. Moreover, for some rare lipids with low abundance within C. *reinhardtii* such as MGDG (34:6), DGDG (36:2), DGDG (36:7), DGTS (35:2), DGTS (36:2), DGTS (39:4), TAG (50:6) and TAG (54:5) [15], which was challenging to detect by the single intact cell method, the peak intensity has been considerably increased by using microfluidic extraction with proper extraction phase, leading to easy differentiation in the MS spectra. This presents a great potential for evaluation of rare lipids in lipidomic studies. It also provides a useful reference for future research involving profiling and in biodiesel studies of various algae.

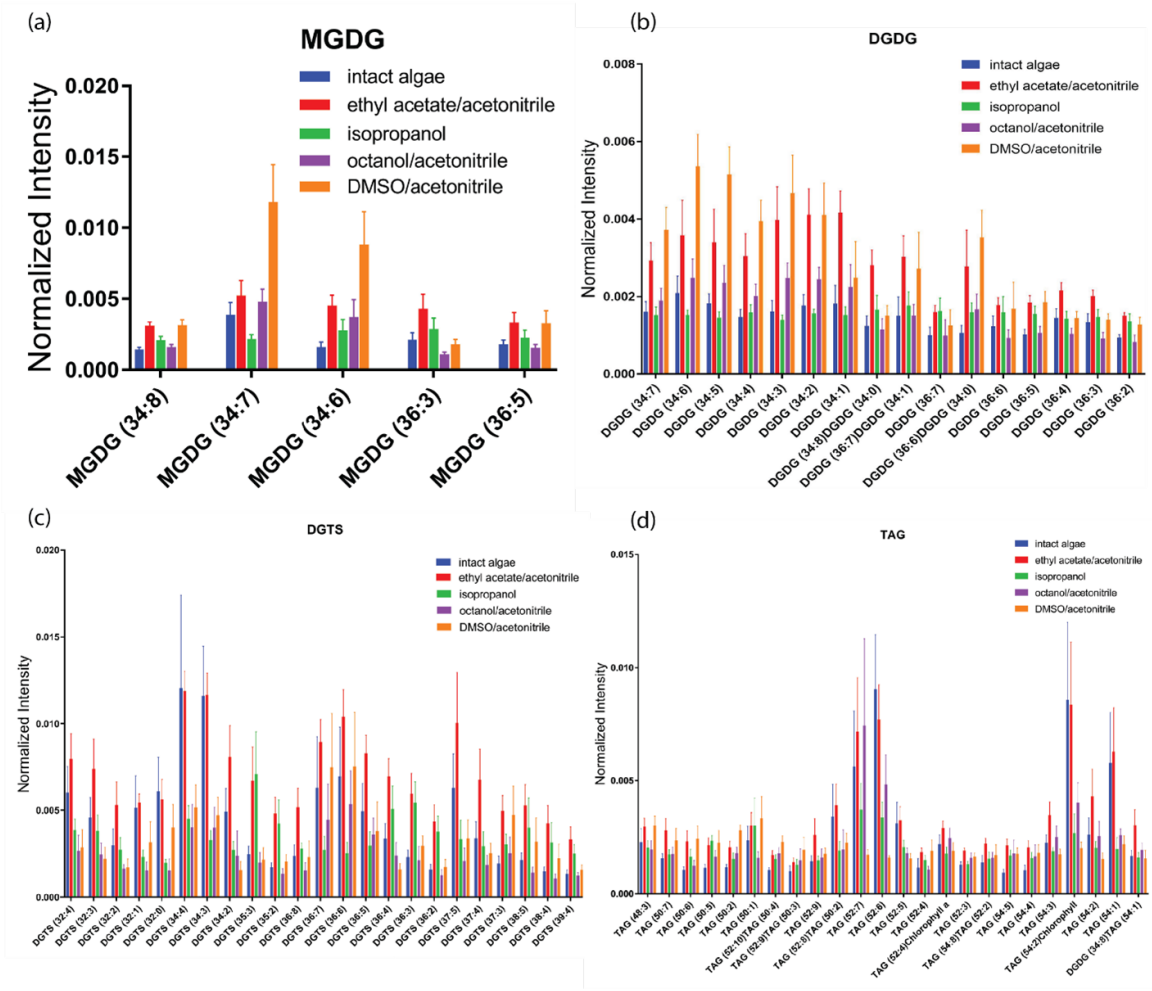

Figure 4.8: Lipid profile of (a) MGDG, (b) DGDG, (c) DGTS and (d) TAG of intact algae single cell and microfluidic lipid extract using different extraction solvent, including EA/ACN, isopropanol, octanol/ACN and DMSO/ACN.

4.5 CONCLUSIONS

In this study, we demonstrated a 3D printed microfluidic system for effective sample preparation that includes cell lysis, lipid extraction, on-chip phase separation and individual phase collection. MALDI-MS was combined with the microfluidic system for demonstrating lipidomic profiling using algae C. *reinhardtii* cells. Two phase numerical simulations

were conducted to show droplet breakup during the extraction process through the pillar array. Single phase velocity field study suggested a dramatic flow rate increase of the fluid when flowing through the gap between the micropillars. These factors contribute to an enhanced mass transfer in the micromixer. Fluorescence and cell counting results showed remarkable cell lysis capability of the microfluidic platform. The TLC and MALDI-MS results showed a marked increase in lipid extraction efficiency compared with the conventional standard Bligh-Dyer method. Furthermore, the effect of different organic solvents on the resulting extracted lipid profile was studied. DMSO/ACN showed higher extraction efficiency towards MGDG and DGDG, while EA/ACN showed better extraction performance for DGTS and TAG. This preferential lipid extraction with different solvent could be used to selectively extract lipids of interest. The printed microfluidic system holds great potential for a fast, efficient, and cost-effective approach for cell lysis and lipid profiling of many cell species. It is particularly useful for those bacteria or plant cells that are protected by robust cell walls which cannot be easily disrupted.

REFERENCES

[1] Yepy H Rustam and Gavin E Reid. Analytical challenges and recent advances in mass spectrometry based lipidomics. *Analytical chemistry*, 90(1):374–397, 2017.

[2] Dan Song, Renpeng Guo, Haibo Huang, Peixiang Zheng, Hong Huang, Qinqin Oyang, Xiaoyue Xiao, Binran Wang, Jingtong Rong, and Rong Liu. 2-amino-3, 8-dimethylimidazo [4, 5-f] quinoxaline alters autophagosome maturation, cellular lipidomic profiles, and expression of core pluripotent factors. *Journal of agricultural and food chemistry*, 67(28):7977–7985, 2019.

[3] Helena Beatriz Ferreira, Tânia Melo, Andreia Monteiro, Artur Paiva, Pedro Domingues, and M Rosário Domingues. Serum phospholipidomics reveals altered lipid profile and promising biomarkers in multiple sclerosis. *Archives of Biochemistry and Biophysics*, 697:108672, 2021.

[4] Changfeng Hu, Wenqing Luo, Jie Xu, and Xianlin Han. Recognition and avoidance of ion source-generated artifacts in lipidomics analysis. *Mass Spectrometry Reviews*, 2020.

[5] Peter V Shanta, Bochao Li, Daniel D Stuart, and Quan Cheng. Lipidomic profiling of algae with microarray maldi-ms toward ecotoxicological monitoring of herbicide exposure. *Environmental Science & Technology*, 55(15):10558–10568, 2021.

[6] Ying-Yong Zhao, Xian-Long Cheng, Rui-Chao Lin, and Feng Wei. Lipidomics applications for disease biomarker discovery in mammal models. *Biomarkers in medicine*, 9(2):153–168, 2015.

[7] Kui Yang and Xianlin Han. Lipidomics: techniques, applications, and outcomes related to biomedical sciences. *Trends in biochemical sciences*, 41(11):954–969, 2016.

[8] Jurgen Schiller, Rosmarie Suss, Beate Fuchs, Matthias Muller, Olaf Zschornig, and Klaus Arnold. Maldi-tof ms in lipidomics. *Front Biosci*, 12:2568–2579, 2007.

[9] Xianlin Han and Richard W Gross. Global analyses of cellular lipidomes directly from crude extracts of biological samples by esi mass spectrometry: a bridge to lipidomics. *Journal of lipid research*, 44(6):1071–1079, 2003.

[10] Son N Nguyen, Jennifer E Kyle, Sydney E Dautel, Ryan Sontag, Teresa Luders, Richard Corley, Charles Ansong, James Carson, and Julia Laskin. Lipid coverage in nanospray desorption electrospray ionization mass spectrometry imaging of mouse lung tissues. *Analytical chemistry*, 91(18):11629–11635, 2019.

[11] Beate Fuchs and Jürgen Schiller. Application of maldi-tof mass spectrometry in lipidomics. *European Journal of Lipid Science and Technology*, 111(1):83–98, 2009.

[12] Min Li, Li Yang, Yu Bai, and Huwei Liu. Analytical methods in lipidomics and their applications. *Analytical chemistry*, 86(1):161–175, 2014.

[13] Orane Guillaume-Gentil, Timo Rey, Patrick Kiefer, Alfredo J Ibanez, Robert Steinhoff, Rolf Bronnimann, Livie Dorwling-Carter, Tomaso Zambelli, Renato Zenobi, and Julia A Vorholt. Single-cell mass spectrometry of metabolites extracted from live cells by fluidic force microscopy. *Analytical chemistry*, 89(9):5017–5023, 2017.

[14] Thanh D Do, Joseph F Ellis, Elizabeth K Neumann, Troy J Comi, Emily G Tillmaand, Ashley E Lenhart, Stanislav S Rubakhin, and Jonathan V Sweedler. Optically guided single cell mass spectrometry of rat dorsal root ganglia to profile lipids, peptides and proteins. *Chemphyschem: a European journal of chemical physics and physical chemistry*, 19(10):1180, 2018.

[15] Peter V Shanta, Bochao Li, Daniel D Stuart, and Quan Cheng. Plasmonic gold templates enhancing single cell lipidomic analysis of microorganisms. *Analytical chemistry*, 92(9):6213–6217, 2020.

[16] Chia-Yen Lee, Chin-Lung Chang, Yao-Nan Wang, and Lung-Ming Fu. Microfluidic mixing: a review. *International journal of molecular sciences*, 12(5):3263–3287, 2011.

[17] Waqas Waheed, Omar Z Sharaf, Anas Alazzam, and Eiyad Abu-Nada. Dielectrophoresis-field flow fractionation for separation of particles: A critical review. *Journal of Chromatography A*, page 461799, 2020.

[18] Kai Wang and Guangsheng Luo. Microflow extraction: A review of recent development. *Chemical Engineering Science*, 169:18–33, 2017.

[19] Davide Ciceri, Jilska M Perera, and Geoffrey W Stevens. The use of microfluidic devices in solvent extraction. *Journal of Chemical Technology & Biotechnology*, 89(6):771–786, 2014.

[20] Qi Li, Fei Tang, Xinming Huo, Xi Huang, Yan Zhang, Xiaohao Wang, and Xinrong Zhang. Native state single-cell printing system and analysis for matrix effects. *Analytical chemistry*, 91(13):8115–8122, 2019.

[21] Shane S Wells and Robert T Kennedy. High-throughput liquid–liquid extractions with nanoliter volumes. *Analytical chemistry*, 92(4):3189–3197, 2020.

[22] A Sanati Nezhad. Microfluidic platforms for plant cells studies. *Lab on a Chip*, 14(17):3262–3274, 2014.

[23] Hyun Seok Lim, Jaoon YH Kim, Ho Seok Kwak, and Sang Jun Sim. Integrated microfluidic platform for multiple processes from microalgal culture to lipid extraction. *Analytical chemistry*, 86(17):8585–8592, 2014.

[24] Tao Sun, Sean Pawlowski, and Mitchell E Johnson. Highly efficient microscale purification of glycerophospholipids by microfluidic cell lysis and lipid extraction for lipidomics profiling. *Analytical chemistry*, 83(17):6628–6634, 2011.

[25] Sidra Waheed, Joan M Cabot, Niall P Macdonald, Trevor Lewis, Rosanne M Guijt, Brett Paull, and Michael C Breadmore. 3d printed microfluidic devices: enablers and barriers. *Lab on a Chip*, 16(11):1993–2013, 2016.

[26] Anna V Nielsen, Michael J Beauchamp, Gregory P Nordin, and Adam T Woolley. 3d printed microfluidics. *Annual Review of Analytical Chemistry*, 13:45–65, 2020.

[27] Samuel S Hinman, Kristy S McKeating, and Quan Cheng. Plasmonic sensing with 3d printed optics. *Analytical chemistry*, 89(23):12626–12630, 2017.

[28] Bligh Eg and Dyer Wj. A rapid method of total lipid extraction and purification. *Canadian Journal of Biochemistry and Physiology*, 37(8):911–917, 1959.

[29] Zhengdong Yang, Alexander S Malinick, Tiantian Yang, Wei Cheng, and Quan Cheng. Gold nanoparticle-coupled liposomes for enhanced plasmonic biosensing. *Sensors and Actuators Reports*, 2(1):100023, 2020.

[30] Abdennour Abbas, Matthew J Linman, and Quan Cheng. Patterned resonance plasmonic microarrays for high-performance spr imaging. *Analytical chemistry*, 83(8):3147–3152, 2011.

[31] Yanlin Wang, Qiaoyu Li, Haimei Shi, Keqi Tang, Liang Qiao, Guopeng Yu, Chuanfan Ding, and Shaoning Yu. Microfluidic raman biochip detection of exosomes: A promising tool for prostate cancer diagnosis. *Lab on a Chip*, 20(24):4632–4637, 2020.

[32] N Harries, JR Burns, David Anthony Barrow, and C Ramshaw. A numerical model for segmented flow in a microreactor. *International journal of heat and mass transfer*, 46(17):3313–3322, 2003.

[33] Young Hoon Choi, Young Soo Song, et al. Droplet-based microextraction in the aqueous two-phase system. *Journal of Chromatography A*, 1217(24):3723–3728, 2010.

[34] Kyuseok Song and Quan Cheng. Desorption and ionization mechanisms and signal enhancement in surface assisted laser desorption ionization mass spectrometry (saldi-ms). *Applied Spectroscopy Reviews*, 55(3):220–242, 2020.

[35] AF Maarten Altelaar, Ivo Klinkert, Kees Jalink, Robert PJ de Lange, Roger AH Adan, Ron MA Heeren, and Sander R Piersma. Gold-enhanced biomolecular surface imaging of cells and tissue by sims and maldi mass spectrometry. *Analytical chemistry*, 78(3):734–742, 2006.

[36] Youchuang Chao and Ho Cheung Shum. Emerging aqueous two-phase systems: from fundamentals of interfaces to biomedical applications. *Chemical Society Reviews*, 49(1):114–142, 2020.

[37] Kaiyun Fu, Wichitpan Rongwong, Zhiwu Liang, Yanqing Na, Raphael Idem, and Paitoon Tontiwachwuthikul. Experimental analyses of mass transfer and heat transfer of post-combustion co2 absorption using hybrid solvent mea–meoh in an absorber. *Chemical Engineering Journal*, 260:11–19, 2015.

[38] S Protiere, MZ Bazant, DA Weitz, and Howard A Stone. Droplet breakup in flow past an obstacle: A capillary instability due to permeability variations. *EPL (Europhysics Letters)*, 92(5):54002, 2010.

[39] A Ebrahimi Khabbazi, AJ Richards, and M Hoorfar. Numerical study of the effect of the channel and electrode geometry on the performance of microfluidic fuel cells. *Journal of Power Sources*, 195(24):8141–8151, 2010.

[40] Piyush Kumar and Manabendra Pathak. Pressure transient during wettability-mediated droplet formation in a microfluidic t-junction. *Industrial & Engineering Chemistry Research*, 59(25):11839–11850, 2020.

[41] Omid Sartipzadeh, Seyed Morteza Naghib, Amir Seyfoori, Mehdi Rahmanian, and Fatemeh Sadat Fateminia. Controllable size and form of droplets in microfluidic-assisted devices: Effects of channel geometry and fluid velocity on droplet size. *Materials Science and Engineering: C*, 109:110606, 2020.

[42] Shazia Bashir, Julia M Rees, and William B Zimmerman. Simulations of microfluidic droplet formation using the two-phase level set method. *Chemical Engineering Science*, 66(20):4733–4741, 2011.

[43] Voon-Loong Wong, Katerina Loizou, Phei-Li Lau, Richard S Graham, and Buddhika N Hewakandamby. Characterizing droplet breakup rates of shear-thinning dispersed phase in microreactors. *Chemical Engineering Research and Design*, 144:370–385, 2019.

[44] Soo Youn Lee, Jun Muk Cho, Yong Keun Chang, and You-Kwan Oh. Cell disruption and lipid extraction for microalgal biorefineries: A review. *Bioresource technology*, 244:1317–1328, 2017.

[45] Dong-Yeon Kim, Durairaj Vijayan, Ramasamy Praveenkumar, Jong-In Han, Kyubock Lee, Ji-Yeon Park, Won-Seok Chang, Jin-Suk Lee, and You-Kwan Oh. Cell-wall disruption and lipid/astaxanthin extraction from microalgae: Chlorella and haematococcus. *Bioresource technology*, 199:300–310, 2016.

[46] Jing-Yan Liu, Li-Hua Zeng, and Zhen-Hui Ren. The application of spectroscopy technology in the monitoring of microalgae cells concentration. *Applied Spectroscopy Reviews*, 56(3):171–192, 2021.

[47] Yunho Choi, Younseong Song, Yong Tae Kim, Seok Jae Lee, Kyoung G Lee, and Sung Gap Im. Multifunctional printable micropattern array for digital nucleic acid assay for microbial pathogen detection. *ACS Applied Materials & Interfaces*, 13(2):3098–3108, 2021.

[48] Beate Fuchs, Jürgen Schiller, Rosmarie Süß, Matthias Zscharnack, Augustinus Bader, Peter Müller, Martin Schürenberg, Michael Becker, and Detlev Suckau. Analysis of stem cell lipids by offline hptlc-maldi-tof ms. *Analytical and bioanalytical chemistry*, 392(5):849–860, 2008.

[49] Anatol Luther, Matthias Urfer, Michael Zahn, Maik Müller, Shuang-Yan Wang, Milon Mondal, Alessandra Vitale, Jean-Baptiste Hartmann, Timothy Sharpe, Fabio Lo Monte, et al. Chimeric peptidomimetic antibiotics against gram-negative bacteria. *Nature*, 576(7787):452–458, 2019.

[50] Amrita Ranjan, Chetna Patil, and Vijayanand S Moholkar. Mechanistic assessment of microalgal lipid extraction. *Industrial & Engineering Chemistry Research*, 49(6):2979–2985, 2010.

[51] Ana Reis, Alisa Rudnitskaya, Gavin J Blackburn, Norsyahida Mohd Fauzi, Andrew R Pitt, and Corinne M Spickett. A comparison of five lipid extraction solvent systems for lipidomic studies of human ldl [s]. *Journal of lipid research*, 54(7):1812–1824, 2013.

[52] Takeshi Honda, Masaya Miyazaki, Hiroyuki Nakamura, and Hideaki Maeda. Controllable polymerization of n-carboxy anhydrides in a microreaction system. *Lab on a Chip*, 5(8):812–818, 2005.

[53] Jessamine Ng Lee, Cheolmin Park, and George M Whitesides. Solvent compatibility of poly (dimethylsiloxane)-based microfluidic devices. *Analytical chemistry*, 75(23):6544–6554, 2003.

Chapter 5

Conclusions

Chip-based biosensing systems play an important role in studies of biochemical interactions and omics investigations [1] [2]. The commercial surface plasmon resonance (SPR) sensor is a typical chip-based biosensor that consists of a light source, a prism coupler, and a detector that can monitor reflected light. SPR is a powerful tool in the study of biological interactions that provides binding kinetics information [3]; Matrix-assisted laser desorption and ionization mass spectrometry (MALDI-MS), is a soft ionization mass spectrometric methods that analyzes a sample and associated matrix mixture on a MALDI chip/plate [4]. Microfluidic devices coupled MALDI-MS provides an integrated platform for sample treatment and lipid analysis, and has been used as a powerful tool for lipidomic research. In this thesis, nanoparticle fabrication methods and 3D printing techniques have been applied for the development of a sensing platform based on SPR and sample treatment for microfluidics coupled MALDI-MS lipidomics research.

In Chapter 2, nanoclusters consisting of POPC vesicles and gold nanoparticles

were used for SPR signal amplification by taking advantage of the large mass of liposomes as well as the plasmon coupling effect of noble metal nanoparticles. These nanoclusters were prepared using the simple yet robust approach of a salt-induced coupling. According to UV-Vis, NTA, and SPR characterization, the POPC-AuNPs were stable for at least 4 weeks, with reproduceable signal enhancement. The amplified signal of POPC-AuNPs was more than six times larger than that of DNA-AuNPs and 1.5 times larger than that of POPC liposomes using a standard biotin-streptavidin binding platform. The POPC-AuNPs were then functionalized by GM1 for recognition of cholera toxin captured on the gold surface, and signal enhancement performance was evaluated. The results demonstrated that the detection limit for cholera toxin can be as low as 0.1 ng/mL. Moreover, larger AuNPs and AgNPs were assembled on the surface of liposomes via similar approaches. The nanoclusters offered significant signal enhancement of SPR sensing, indicating the universality of the method.

Future directions include application of this method to couple various metal nanoparticles of different sizes and shapes with liposomes for use as signal amplification tags for biosensors, especially for metal nanoparticles with brilliant signal enhancement effects but poor stability or that are difficult to modify directly [5] [6] [7]. In addition, similar biomimetic sensing platforms could be developed and applied in the study of nanoparticle-lipid membrane interactions and protein-membrane interactions.

In Chapter 3, we described several robust and cost-effective approaches to fabricate plasmonic microarrays for multiplex biosensing using 3D printing techniques. First, 3D printed Dove Prisms with micropatterns were fabricated and integrated in the SPRi setup,

resulting in brilliant sensing performance. To ensure the necessary optical quality, the printed prisms were sanded and polished, reducing the surface roughness to 10 nm. The prisms showed smooth background in the reflected images and the micropattern arrays were clearly defined. The Dove prisms were further compared with 3D printed equilateral prisms. Because of a larger base angle, the 3D printed Dove prism showed an 8° smaller sensing angle than the equilateral prisms, providing a 21% larger sensing area and, therefore, more reliable results. The sensitivity of the Dove prism coupled SPRi was evaluated via salt sensing and protein recognition. The Dove prism coupled SPRi was capable of detecting 1 ng/mL cholera toxin, which is quite close to the sensitivity of commercial glass prism coupled SPRi.

To carry out more assays simultaneously without the need for photolithography, we developed a 3D printed E-beam mask for the fabrication of gold microarrays during the E-beam evaporation process. The gold microarrays were deposited both on glass slides and directly on the prisms for SPRi sensing, demonstrating high sensitivity to the change of the refractive index of the medium. Future experiments are needed to assess the protein sensitivity of the platform. Moreover, the sensing performance of the gold plasmonic arrays, produced through use of a 3D printed E-beam mask for MALDI-MS assays, could also be investigated.

In Chapter 4, we continued application of 3D printing techniques in the development of biosensing platforms. We designed and fabricated a 3D printed microfluidic system for on-chip cell lysis, lipid extraction, and phase separation for MALDI-MS lipidomics studies. The aqueous phase containing algae cells and the organic extraction phase were injected

through two inlets of the microfluidic device and mixed in the micromixer section. The micropillars in the micromixer have been shown to improve the mass transfer of the two phases by fluidic velocity and droplet breakup simulation. The mixed solution then entered an on-chip reservoir for phase separation and collection. According to the fluorescence and cell count data, only 10% of cells could be observed after undergoing microfluidic extraction, indicating high cell lysis efficiency. Evaluation of lipid extraction efficiency was carried out using TLC and MALDI-MS, and the results demonstrated a 21% increase compared to the conventional Bligh-Dyer bulk extraction method. Furthermore, lipid profiles after microfluidic extraction via different extraction phases were investigated, which can be useful references when selecting the proper organic phases through which to extract lipids of interest.

As a newly emerged discipline, lipidomics is playing an ever more important role in the biological and environmental sciences [8]. Cell lysis and lipid extraction is often a crucial step in sample processing. However, there are some bacteria and plant cells with robust structures that make cell lysis challenging [9]. Considering that the work described in Chapter 4 provides a highly efficient cell lysis and lipid extraction platform, investigations of novel microfluidic designs for lipid extraction of a larger range of cell types could be pursued in future research.

REFERENCES

[1] Ying Liu, Puhong Liao, Quan Cheng, and Richard J Hooley. Protein and small molecule recognition properties of deep cavitands in a supported lipid membrane determined by calcination-enhanced spr spectroscopy. *Journal of the American Chemical Society*, 132(30):10383–10390, 2010.

[2] Peter V Shanta, Bochao Li, Daniel D Stuart, and Quan Cheng. Plasmonic gold templates enhancing single cell lipidomic analysis of microorganisms. *Analytical chemistry*, 92(9):6213–6217, 2020.

[3] Rebecca J Green, Richard A Frazier, Kevin M Shakesheff, Martyn C Davies, Clive J Roberts, and Saul JB Tendler. Surface plasmon resonance analysis of dynamic biological interactions with biomaterials. *Biomaterials*, 21(18):1823–1835, 2000.

[4] Yaju Zhao, Minmin Tang, Qiaobo Liao, Zhoumin Li, Hui Li, Kai Xi, Li Tan, Mei Zhang, Danke Xu, and Hong-Yuan Chen. Disposable mos2-arrayed maldi ms chip for high-throughput and rapid quantification of sulfonamides in multiple real samples. *ACS sensors*, 3(4):806–814, 2018.

[5] Jianlong Wang, Ahsan Munir, Zanzan Zhu, and H Susan Zhou. Magnetic nanoparticle enhanced surface plasmon resonance sensing and its application for the ultrasensitive detection of magnetic nanoparticle-enriched small molecules. *Analytical chemistry*, 82(16):6782–6789, 2010.

[6] Qiao Zhang, Jianping Ge, Tri Pham, James Goebl, Yongxing Hu, Zhenda Lu, and Yadong Yin. Reconstruction of silver nanoplates by uv irradiation: tailored optical properties and enhanced stability. *Angewandte Chemie*, 121(19):3568–3571, 2009.

[7] Wing-Cheung Law, Ken-Tye Yong, Alexander Baev, and Paras N Prasad. Sensitivity improved surface plasmon resonance biosensor for cancer biomarker detection based on plasmonic enhancement. *ACS nano*, 5(6):4858–4864, 2011.

[8] Kui Yang and Xianlin Han. Lipidomics: techniques, applications, and outcomes related to biomedical sciences. *Trends in biochemical sciences*, 41(11):954–969, 2016.

[9] Mathias Middelboe and Niels OG Jørgensen. Viral lysis of bacteria: an important source of dissolved amino acids and cell wall compounds. *Journal of the Marine Biological Association of the United Kingdom*, 86(3):605–612, 2006.